



**SUB-DIFFUSIVE PHOTON TRANSPORT IN
APERIODIC NANOSTRUCTURES**

TRAVIS RICH

Thesis submitted in partial fulfillment
of the requirements for the degree of
Master of Science

**BOSTON
UNIVERSITY**

BOSTON UNIVERSITY
COLLEGE OF ENGINEERING

Thesis

**SUB-DIFFUSIVE PHOTON TRANSPORT IN APERIODIC
NANOSTRUCTURES**

by

TRAVIS RICH

B.S., Boston University, 2010

Submitted in partial fulfillment of the
requirements for the degree of
Master of Science

2011

Approved by

First Reader

Luca Dal Negro, PhD
Assistant Professor of Electrical and Computer Engineering

Second Reader

Alexander Sergienko, PhD
Associate Professor of Electrical and Computer Engineering

Third Reader

Enrico Bellotti, PhD
Associate Professor of Electrical and Computer Engineering

Fourth Reader

Thomas D.C. Little, PhD
Professor of Electrical and Computer Engineering

*All those wrong notes you
played made it sound more original.*

Thomas Kenny

Acknowledgments

Twelve months ago I joined the Nanomaterials and Nanostructured Optics group and since then since then the I've been aided by a cohort of people supporting me and my research. I'd like to thank Professor Luca Dal Negro for giving me the opportunity to get my feet wet in the field of nanophotonics and supporting my passions and interests along the way. This thesis would not have been possible without the vision and assistance you have given me throughout the past year. More importantly, our discussions concerning research and science broadly have shaped my understanding of the world and my abilities as a researcher - thank you! I'm of course also grateful to my committee, Professors Enrico Bellotti, Alexander Sergienko, and Tom Little, for providing guidance throughout the thesis writing process. I'd also like to thank the NaNO group members, Alyssa Pasquale, Dianmin Lin, Gary Walsh, Jacob Trevino, Nate Lawrence, Salvo Minissale, Selcuk Yerci, and Sylvanus Lee: thanks for putting up with all my questions, jokes, rants, and games - I've cherished the time I've been able to spend with all of you in lab.

I'd also like to thank those outside of the NaNO lab that have made my foray into graduate school an amazing learning experience. Everyone associated with the Smart Lighting Center: Professor Tom Little - thanks for introducing me into the world of engineering research and giving me countless opportunities to succeed; Aaron Ganick, Dan Ryan, Jimmy Chau, Mike Rahaim, and everyone else, thanks for being supportive through my explorations. I'm indebted to the advice and guidance provided by Bunmi Adekore in both academic and non-academic matters - you have provided a very helpful hand in navigating me through a hectic year. I'm also very grateful to everyone in the ECE office, Julie, Austin, Carly, Jamie, and the rest of the gang - thanks for letting me duck under some of the red tape and for all of the assistance you've given that has let me concentrate on my research rather than paperwork.

I'd like to thank my Dad, Mom, Josh, and Peter for bringing me up in an environment

that nurtured my curiosity and for being selflessly supportive of my ambitions and goals. Thanks for teaching me how to learn, rather than what to learn. To Sam, trying to list even a few things that I'm thankful for would be an injustice to everything you've done for me - I couldn't imagine where I'd be right now without your support. And finally, thanks to those outside of ECE, Jasmin, Steve, Aneesh, Maisam, Gabe, Chugg, Schuyler, Grace, Angelo, Max, Jess, Joe, Nick, Tags, Kirby, Rob, Mark, Molly, Erin, Dave, and Mike, for giving me something to talk about besides electrons and photons.

SUB-DIFFUSIVE PHOTON TRANSPORT IN APERIODIC NANOSTRUCTURES

TRAVIS RICH

ABSTRACT

There has been recent excitement in the photonic community regarding anomalous transport of light through engineered materials. This enthusiasm has focused largely on superdiffusion while the realm of subdiffusion has been left largely unexplored. Recognizing this void in understanding, this thesis provides some of the first study into the domain of subdiffusive transport in deterministic photonic systems. Such a phenomenon is of great interest to the development of advanced thin-film solar cells and optical sensing technologies which depend heavily on multiple scattering phenomena and the engineering of slow light. Exploration into this matter begins through random walk modeling of diffusive transport processes. While previous theoretical study on slowed transport processes has focused on randomly disordered media, this thesis places an emphasis on identifying subdiffusive effects in deterministic systems. Through these studies, subdiffusion is demonstrated in one-dimensional and two-dimensional deterministic aperiodic systems defined by the Rudin-Shapiro sequence. Furthermore, the unexpected result of Sinai diffusion is demonstrated for the first time in deterministic media.

This challenge is further explored through electromagnetic simulations performed using the Finite-Difference Time-Domain method. Pseudo one-dimensional deterministic aperiodic systems are examined through the study of light propagation in aperiodic dielectric waveguide structures of varying refractive index. An emphasis is placed on the study of the Rudin-Shapiro sequence due to the subdiffusive effects seen in the random walk simulations on this structure. Subdiffusion is successfully demonstrated through

these electromagnetic simulations and a process for tuning the diffusion exponent is offered through the scaling of the waveguide structure. This thesis further provides suggestions on the device fabrication process and, importantly, provides a procedure with which the diffusive properties of any structure of arbitrary material composition and structure can be analyzed.

Contents

1 Light in Complex Media	1
1.1 Diffusive Transport of Light in Random Media	1
1.1.1 Energy Velocity of Light	2
1.2 Light Scattering	8
1.2.1 Single Scattering	10
1.2.2 Multiple Scattering	13
1.3 Light Localization	15
1.3.1 Scaling Theory of Localization	15
1.3.2 Localization in Deterministic Aperiodic Media	18
1.4 Introduction to Deterministic Aperiodic Media	19
1.4.1 Fibonacci Sequence	23
1.4.2 Thue-Morse Sequence	24
1.4.3 Rudin-Shapiro Sequence	25
1.4.4 Generalization to Two-Dimensions	26
1.4.5 Aperiodic Spirals	27
2 Anomalous Transport Theory	30
2.1 Super- and Sub-Diffusion	30
2.2 Sinai Logarithmic Sub-Diffusion	34
3 Random Walk Modeling of Photonic Transport	38
3.1 Random Walk Simulations	38
3.1.1 Random Walk on Inhomogeneous Complex Media	39

3.2	Percolation Clusters	40
3.3	One-Dimensional Systems	42
3.4	Two-Dimensional Systems	47
4	Electromagnetic Modeling of Photonic Transport	58
4.1	Electromagnetic Modeling of Diffusion	58
4.1.1	Finite Difference Time Domain Simulations	59
4.2	One-Dimensional Systems	60
4.2.1	Diffusion Constant Analysis	65
4.2.2	Diffusion Exponent Analysis	70
4.2.3	Influence of scattering strength and localization length	76
4.3	Two-Dimensional Systems	80
5	Device Design and Engineering	82
5.1	Fabrication	82
5.2	Experimental Methods	84
6	Conclusion	87
A	Source Code	89
References		102
Curriculum Vitae		105

List of Tables

3.1	Diffusion exponents as calculated from fitting the data in Figure 3.15 . . .	57
4.1	Structures explored as decided due to desirable transmission spectra features.	63
4.2	Frequencies examined in the pulse decay analysis	65
4.3	Frequencies explored for pulse decay measurements.	68
4.4	Diffusion constants calculated from the exponential curve fit of the pulse decay data.	69
4.5	Frequencies examined in the energy transport analysis	71
4.6	Mean square displacement data power law fitting results. The length is held at $L = 512$ for all structures.	73
4.7	Mean square displacement as a function of structure length power law fitting results.	75

List of Figures

1.1	Left: Plot of transmission versus device thickness for two sample wavelengths. Right: Calculated value of l_t as determined through fitting using Ohm's law for light. Both plots taken from arbitrary sample for the use of demonstration. (Bertolotti, 2007)	4
1.2	Diffusion constant as a function of wavelength as obtained from the time-resolved transmission method. (Bertolotti, 2007)	5
1.3	Time resolved transmission data demonstrating the stretched exponential tail. The data is measured in an experimental setup using a 20ps laser pulse at 590nm. The three data sets represent different combinations of the particle diameter - d , structure length - L , diffusion constant D , and absolute mean free path - l_{abs} . (a) $d = 550\text{nm}$, $L = 2.5\text{mm}$, $D = 22\text{m}^2/\text{s}$, $l_{abs}=2600\text{mm}$; (b) $d = 250\text{nm}-550\text{nm}$, $L = 1.51\text{mm}$, $D = 13\text{m}^2/\text{s}$, $l_{abs}=380\text{mm}$; (c) $d = 250\text{nm}$, $L = 1.48\text{mm}$, $D = 15\text{m}^2/\text{s}$, $l_{abs}=340\text{mm}$ (Gaponenko, 2010).	7
1.4	Light scattering at a single arbitrary particle	11
1.5	Depiction of the iterative self-energy process.	11
1.6	Multiple scattering through an arbitrary collection of particles	13
1.7	Universal scaling function versus conductance for the first three dimensions. Note that for $d = 1, 2$ $\beta < 0$ always.	18
1.8	Fourier spectra	20

1.9	Fourier spectra of Fibonacci, Thue-Morse, and Rudin-Shapiro sequences. (Dal Negro et al., 2008)	21
1.10	Classification of aperiodic systems (Maciá, 2006)	22
1.11	Fibonacci Sequence	23
1.12	Thue-Morse Sequence	24
1.13	Rudin-Shapiro Sequence	25
1.14	(a) Visual representations of 2D generation algorithm, (b) 2D Fibonacci sequence, (c) 2D diffraction spectra, (d) 1D Fourier transfer taken from cutting vertically along arrow in (c). (Dallapiccola et al., 2008)	26
1.15	Two-dimensional diffraction patterns (Gopinath et al., 2008)	27
1.16	SEM micrographs of (a) golden-angle spiral, (b) α_1 -spiral, and (c) α_2 -spiral fabricated from gold nanoparticles of diameter 200nm. The calculated pseudo-Brillouin zones of the (d) golden-angle spiral, (e) α_1 -spiral, and (f) α_2 -spiral. (Trevino et al., 2011)	29
2.1	The three diffusion regimes as described by analysis of the mean squared displacement versus time.	34
3.1	Four different percolation clusters with values of p = (a) 0.15, (b) 0.35, (c) 0.60, and (d) 0.85	41
3.2	Mean Squared Displacement, $\langle r^2(t) \rangle$ versus Steps. Power Law fits yields exponents for $p = 0.3, 0.4, 0.5, 0.59, 0.65, 0.75$ of $\beta = 0.96, 0.98, 0.89, 0.68, 0.12, 0.01$ respectively.	42
3.3	Random walk implementation on an open 1D grid	43
3.4	Probability Density function at five different time intervals	44
3.5	Random walk implementation on an occupied 1D grid	45
3.6	Mean square displacement versus Number of steps taken	46

3.7	Mean square displacement versus Number of steps taken for the Rudin-Shapiro and random arrays plotted versus the natural logarithm of the number of steps taken. Data is the same as from Figure 3.6.	47
3.8	Random walk implementation on a 2D grid	48
3.9	Random walk implementation on an unrestricted 2D geometry	49
3.10	A sample single random walk on a aperiodic spiral (left) and the probability density map of an ensemble average of many ($> 10^4$) random walks (right).	50
3.11	Mean Square Displacement versus Number of iterations considered in the ensemble average.	51
3.12	Averaged probability of taking a step in a given angle. The function that generates the potential angle at which to step is uniform, but due to occupied lattice spaces, not all are acceptable, hence the non-uniform distributions above.	52
3.13	Mean Square Displacement versus Starting location. The color bar represents the mean square displacement value.	54
3.14	Probability density maps. For a given location: Red = higher probability of being found → Blue = lower probability of being found	55
3.15	Mean squared displacement versus Number of steps taken	56
4.1	An electromagnetic dipole pulse evolving through (top row) a random nanostructure array and (bottom row) a homogeneous medium.	59
4.2	FDTD Geometry Representation	60
4.3	A depiction of an aperiodic waveguide structure setup in an FDTD environment. Note, the orange PML layers are kept at roughly 10 times the wavelength of the incident light from any structure to avoid disruptive reflections. Yee cell mesh sizes are exaggerated to show detail.	61

4.4	Sample FDTD transmission setup. Note yellow frequency monitor to the right of the structure and the pink source indicator at the lefthand side. The orange border is the PML layers.	62
4.5	Transmission Spectra for three different systems at three different lengths each.	64
4.6	Intensity versus time as a function of both structure and frequency, measured at the output facet of the structure.	66
4.7	Intensity versus time as a function of both scale and frequency, measured at the output facet of the structure.	67
4.8	Intensity versus time for the three structures of interest. Each data set is fit by an exponential curve, yielding exponents of -0.0499, -0.00141, and -0.00214 for the Periodic, Rudin-Shapiro Si, and Rudin-Shapiro SiN structures, respectively.	69
4.9	Sample FDTD diffusion length measurement setup. Note the 2D field monitor surrounding the structure and the 1D index monitor through the center of the structure.	71
4.10	Regimes of the energy density displacement data.	72
4.11	Mean Squared Displacement versus Time in both linear and log-log scale. The power law curve fits are overlaid with dotted lines.	73
4.12	Mean Square Displacement versus Time power law fits.	74
4.13	Mean Square Displacement vs. Time as a function of the structure length. .	75
4.14	Mean Square Displacement vs. Time as a function of the structure length. Power law fits are overlaid.	76
4.15	Reciprocal transmission versus the system length. The slope of this data yields the localization length, l_c (Daozhong et al., 1994).	77

4.16	Pulse propagation in the Rudin-Shapiro Si and Air structure. The strong scattering leads to a localized mode that does no propagate with time.	78
4.17	Pulse propagation in the Rudin-Shapiro SiN and Doped SiN structure. The index contrast and scattering strength are engineered such that propagation of the light pulse is allowed.	79
4.18	Pulse propagation in the Periodic SiN and Doped SiN structure.	79
4.19	Acoustic pulse propagation through a random one-dimensional medium (Fouque et al., 2007).	80
4.20	Sample CAD layout of a two-dimensional Rudin-Shapiro structure.	81
5.1	SEM Micrographs of aperiodic waveguides. (Courtesy of Nate Lawrence)	83
5.2	Experimental setup schematics (Courtesy of Nate Lawrence)	84
5.3	IR CCD images of out-of-plane light scattering from aperiodic waveguides(Courtesy of Nate Lawrence)	85

List of Abbreviations

1D	One-Dimensional
2D	Two-Dimensional
3D	Three-Dimensional
EBL	Electron Beam Lithography
FDTD	Finite-Difference Time-Domain
MSD	Mean square displacement
PDF	Probability Distribution Function
RS	Rudin-Shapiro
Si	Silicon
SiN	Silicon Nitride
TM	Thue-Morse

List of Symbols

a	scaling factor
$\alpha(\vec{r})$	Polarizability
β	Scaling function
c	Speed of light
d	System dimensionality
D	Diffusion Constant
δ	Dirac delta function
$\delta\omega$	System eigenmode width
$\Delta\omega$	System eigenmode separation distance
E	Electromagnetic Field
ϵ	Electromagnetic permittivity
\mathcal{F}	Fourier transform
g	Green's function
g_0	Fourier-space Green's function
γ	Conductance
γ_c	Critical conductance
η	Random walker location probability
θ	Average waiting time
J	Source current density
k_0	Wave vector in free space
l_c	Localization length
l_i	Inelastic mean free path
l_s	Scattering mean free path
l_t	Transport mean free path
L	Sample thickness
L_d	Diffusion length
\mathcal{L}	Laplace transform
n	Particle density
ξ	Localization length
P_s	Step distribution

\mathcal{P}	Random walk propagator
\vec{r}	Position vector
r_0	Source position
R	Reflectance
σ^2	Step length variance
σ_s	Scattering cross section
σ_t	Radiation pressure
T	Transmission
τ	Wait time
τ_i	Absorption time
τ_H	Heisenberg time
τ_t	Transport time
u	Energy density
v	Wave transport velocity
v_e	Energy velocity
v_p	Phase velocity
V	Scattering potential
$W(\tau)$	Wait time distribution
ω	Angular frequency
Ψ	Random walker non-jump probability

Feynman Diagram Notation

○	Scattering potential
—	Fourier space Green's function
—	Connects scattering events occurring on a single particle
×	Single particle t-matrix
⊗	Averaged t-matrix

Chapter 1

Light in Complex Media

1.1 Diffusive Transport of Light in Random Media

We define as a random medium any dielectric structure whose refractive index randomly fluctuates spatially over length scales comparable to the wavelength of light. Such media can be fabricated, for example, through various doping schemes or through deposition of nanoparticles onto a substrate. Due to the effects of multiple scattering of light (see Section 1.2.2), the light transport is said to be diffusive. The high number of scattering events effectively averages the wave interference effects and allows us to characterize the transport with the following diffusion equation for light intensity:

$$\frac{\partial I(r,t)}{\partial t} = D \nabla^2 I(r,t) - \frac{\nu}{l_i} I(r,t). \quad (1.1)$$

Here, D is called the diffusion constant and l_i is the inelastic mean free path. Furthermore, we can define l_s , the scattering mean free path, as the characteristic length between any two consecutive scattering events. If we then take a random collection of appropriately sized particles, we can define l_s as:

$$l_s = \frac{1}{n\sigma}, \quad (1.2)$$

where σ_s is the scattering cross section and n is the particle density.

Similarly, we can define the transport mean free path, l_t , which describes the average distance traveled by a wave before its direction vector is randomized. In certain

scenarios, such as isotropic scattering, we find that $l_t = l_s$. For all other situations we can more generally define:

$$l_t = \frac{1}{1 - \langle \cos(\theta) \rangle} \frac{1}{n\sigma_s}. \quad (1.3)$$

Here we average over $\cos(\theta)$ to give the mean cosine of the scattering angle after each scattering occurrence. Similarly to our scattering cross section, we have the cross section for radiation pressure σ_t which is defined such that $l_t = 1/n\sigma_t$. Additionally, this transport mean free path can be related to the diffusion constant constant D through:

$$D = \frac{1}{d} v l_t, \quad (1.4)$$

where d is the dimension of the system and v is the wave transport velocity (this will be discussed further in Section 1.1.1).

1.1.1 Energy Velocity of Light

While theoreticians agree that scatterers in disordered media lowers the transport velocity of light, experimental verification of this tends to be rather indirect. It is standard practice to thus measure D , the diffusion constant, and from this result extract the transport velocity data.

For the sake of simplicity we explore this topic by defining a filling fraction which in turn defines the disorder of the system under consideration. We define the filling fraction and the fraction of the total spatial volume (or area in lower dimensions) that is occupied by a scattering agent. A low filling fraction intuitively implies less scattering as there are less obstacles from which to interact, whereas a large filling fraction implies the opposite. The simply analogy can be made between this and cars on the highway: fewer cars on the highway (i.e. low filling fraction) yields faster transport than a heavily jammed highway (i.e. high filling fraction).

The theory is rather clear for situations in which there is a low filling fraction or

when the filling fraction is equal to 1, however, this is not the case for the regime in between these two scenarios. When the filling fractions is equal to unity, we expect $v_e = v_p$, where v_e is the energy velocity and v_p is the phase velocity. Unfortunately, for systems that are moderately filled with scatterers, an obvious relationship between these two velocities cannot be made. Rather, experimental techniques are often used to determine them. As previously stated, it is common to first experimentally measure the diffusion constant, D , and from this extract the energy velocity. Doing so relies on the following relationship:

$$D = \frac{1}{3}v_e l_t. \quad (1.5)$$

Both D, l_t can be experimentally measured, and thus we can solve for v_e .

To measure the transport mean free path, l_t , one must simply measure the total transmission, T and reflectance, R of a sample. Rearranging equation 1.6 then yields the transport mean free path.

$$T \approx \frac{l_t}{L} \left(1 + \frac{2}{3} \left[\frac{1+R}{1-R} \right] \right) \quad (1.6)$$

However, this is not a good technique in practice. The resulting calculation of l_t relies heavily on an accurate measurement of the sample thickness, L . Since a sufficiently accurate measurement of the thickness is typically impossible, it is more prudent to take a series of measurements over a range of sample thickness and then fitting this curve to determine l_t . Transmission measurements are typically taken over a range of wavelengths, thus yielding $T(\lambda)$. This can then be plotted with respect to sample thickness, as depicted in Figure 1.1. The transport mean free path is extracted using

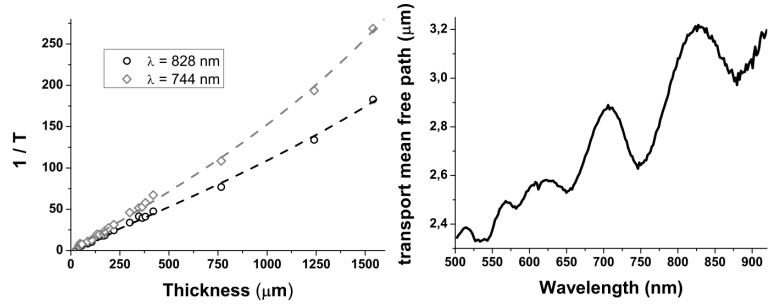


Figure 1.1: **Left:** Plot of transmission versus device thickness for two sample wavelengths. **Right:** Calculated value of l_t as determined through fitting using Ohm's law for light. Both plots taken from arbitrary sample for the use of demonstration. (Bertolotti, 2007)

Ohm's law for light:

$$\begin{aligned}
 T(\lambda) &= S_f(\lambda) \frac{\sinh(2\alpha z_e) \sinh(\alpha z_e)}{\sinh(\alpha(L + 2z_e))} \\
 z_e &= \frac{1}{2\alpha} \ln \left(\frac{1 + \alpha z_0}{1 - \alpha z_0} \right) \\
 z_0 &= \frac{2}{3} l_t(\lambda) \left(\frac{1 + R}{1 - R} \right) \\
 \alpha &= \frac{1}{l_i}
 \end{aligned} \tag{1.7}$$

This form of Ohm's law for light takes into account absorption processes (Garcia et al., 1992). Fitting this data thus yields $l_t(\lambda)$ as depicted in Figure 1.1 (Bertolotti, 2007).

The diffusion constant, D can also be found through transmission measurements. However, in contrast to the previous technique, the diffusion constant is calculated through time-resolved transmission measurements rather than frequency-resolved measurements. A short ($\approx ps$), narrow-bandwidth pulse is sent through a sample of arbitrary thickness and a time profile of the transmission is measured. This profile is then fit using

the solution of the time-dependent diffusion equation for a slab geometry as follows:

$$\begin{aligned}
 T(t) &= \frac{I_0 e^{-\frac{t}{\tau_i}}}{4t\sqrt{(4\pi D)^3}} \sum_{j=-\infty}^{\infty} \left[A e^{-\frac{A^2}{4Dt}} - B e^{-\frac{B^2}{4Dt}} \right] \\
 A &= (1-2j)(L+2z_e) - 2(z_e + l_t) \\
 B &= (2j+1)(L+2z_e) \\
 \tau_i &= \frac{l_t l_i}{3D}
 \end{aligned} \tag{1.8}$$

Here, τ_i is the absorption time of the material and z_e is the same as defined in 1.7. The important notion to draw from this is the relationship between the absorption time and diffusion constant, where $\tau_i \propto \frac{1}{D}$. Figure 1.2 demonstrates sample results collected from a slab populated with scattering spheres of 610nm and illuminated with a 2ps pulse from a Ti:Al₂O₃ laser. As shown, the diffusion constant varies strongly with wavelength.(Bertolotti, 2007).

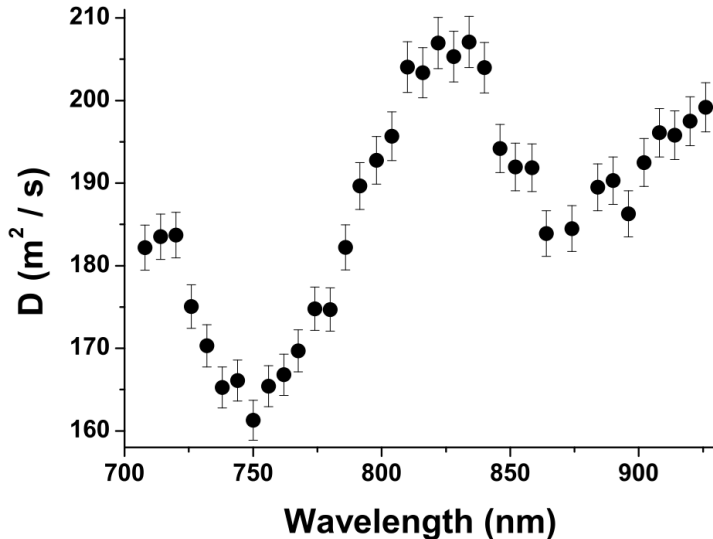


Figure 1.2: Diffusion constant as a function of wavelength as obtained from the time-resolved transmission method. (Bertolotti, 2007)

Equation 1.8 leads to a simplified proportionality relationship between the transmission as a function of time and the diffusion constant. This relationship takes the form of:

$$T(t) \propto e^{\left[-t \left(\frac{\pi^2 D(t)}{(L+2z_e)^2} + \frac{1}{\tau_{abs}} \right) \right]}. \quad (1.9)$$

This proportionality can be used to describe the transmission tail stretching that occurs due to a decreased diffusion constant. Plots of output facet transmission data that demonstrate this exponential stretching can be seen in Figure 1.3 (Gaponenko, 2010).

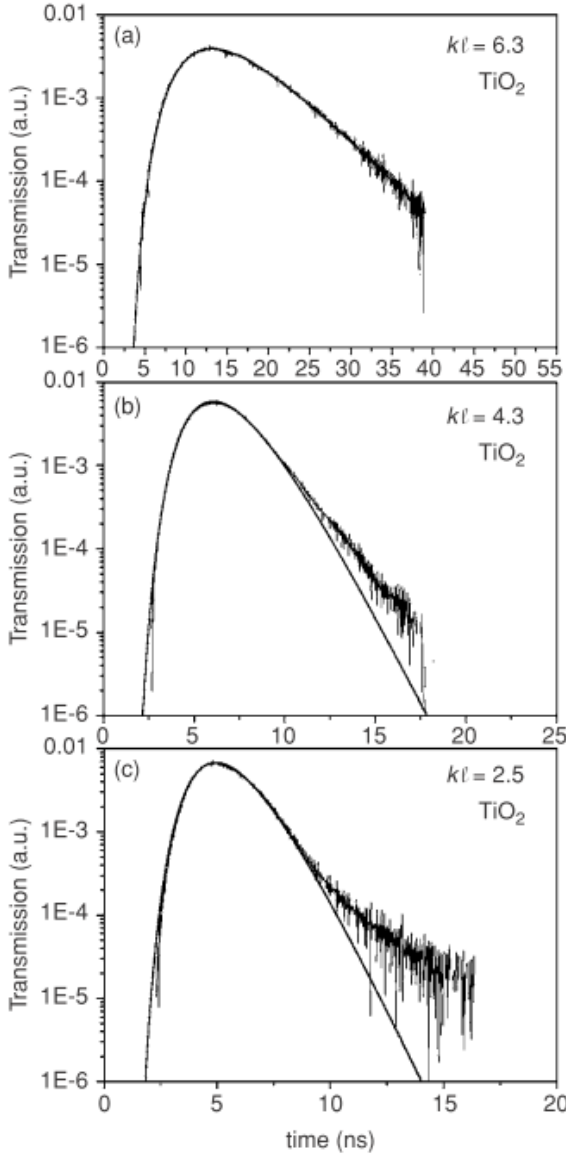


Figure 1.3: Time resolved transmission data demonstrating the stretched exponential tail. The data is measured in an experimental setup using a 20ps laser pulse at 590nm. The three data sets represent different combinations of the particle diameter - d , structure length - L , diffusion constant D , and absolute mean free path - l_{abs} . (a) $d = 550\text{nm}$, $L = 2.5\text{mm}$, $D = 22\text{m}^2/\text{s}$, $l_{abs}=2600\text{mm}$; (b) $d = 250\text{nm}-550\text{nm}$, $L = 1.51\text{mm}$, $D = 13\text{m}^2/\text{s}$, $l_{abs}=380\text{mm}$; (c) $d = 250\text{nm}$, $L = 1.48\text{mm}$, $D = 15\text{m}^2/\text{s}$, $l_{abs}=340\text{mm}$ (Gaponenko, 2010).

1.2 Light Scattering

We now take a more in depth look into the underlying processes that dictate the diffusion behavior. When light interacts with matter, there are four possible processes: scattering, reflection, absorption, and emission. For this thesis though, emission will be neglected. This should be clarified to some degree as scattering and reflection are essentially identical processes. Reflection is simply a special case of scattering where the incident angle and exit angle at which the light travels are equal. In these two processes there is no energy loss, rather, there is simply a redirection of the incident electromagnetic energy. Conversely, energy is lost (from the wave's point of view) during absorption processes. Absorption dissipates electromagnetic energy in the form of heat via phonons.

In order to understand the wave nature of reflection, scattering, and absorption, let us first look at the transport of an electromagnetic wave. Here, we consider a scalar solution which is applicable if the scattering is isotropic (uniform in all directions) on average. This approach neglects polarization effects, but greatly simplifies this first-approach analysis. We start with the wave equation:

$$[\nabla^2 + k_0^2 \epsilon(\vec{r})] E(\vec{r}; k_0) = J(\vec{r}). \quad (1.10)$$

Here k_0 is the wave vector in free space, which is defined as the angular frequency of light, ω , divided by the speed of light, c . $\epsilon(\vec{r})$ is the electromagnetic permittivity, $E(\vec{r}; k_0)$ is the electromagnetic field , and $J(\vec{r})$ is the source current density. For the electromagnetic permittivity, we take the material to be a collection of randomly arranged scattering objects with a polarizability $\alpha(\vec{r})$. Thus we have, the

$$\epsilon(\vec{r}) = 1 + \sum_i \alpha(\vec{r} - \vec{r}_i). \quad (1.11)$$

If the scatter is much smaller than the wavelength of the incident light, we can approximate each one to be a point dipole. This allows (1.11) to become

$$\epsilon(\vec{r}) = 1 + \sum_i \alpha \delta(\vec{r} - \vec{r}_i), \quad (1.12)$$

with $\delta(\vec{r})$ describing the Dirac delta function.

Using the Green's function method to solve the wave equation provides a very general approach that allows us to decompose the transport of light into a series of single scattering events separated by free space propagation. This leads us intuitively to a strategy for describing multiple scattering of light. The Green's function denoted here as $g(\vec{r}, \vec{r}_0; k_0)$, describes the E at \vec{r} due to \vec{r}_0 . This yields,

$$[\nabla^2 + k_0^2 \epsilon(\vec{r})] g(\vec{r}, \vec{r}_0; k_0) = \delta(\vec{r} - \vec{r}_0) \quad (1.13)$$

Using this we find the general solution to the wave equation. Given the linearity of Maxwell's equations, we can use

$$E(\vec{r}) = \int d\vec{r}' j(\vec{r}') g(\vec{r}, \vec{r}'; k_0) \quad (1.14)$$

to describe the electric field due to a collection of sources whose distribution is described by $J(\vec{r})$.

In the simplest case of an electromagnetic wave in free space, we have $\epsilon(\vec{r}) = 1$. Thus:

$$[\nabla^2 + k_0^2] g(\vec{r}, \vec{r}_0; k_0) = \delta(\vec{r} - \vec{r}_0). \quad (1.15)$$

This leads to the Fourier space Green's function, given by:

$$g_0^{R,A}(\vec{k}; k_0) = \frac{1}{|\vec{k}|^2 - k_0^2 \pm i0} e^{-i\vec{k}\vec{r}_0}. \quad (1.16)$$

We introduce $\pm i0$ to guarantee that the inverse Fourier transform converges. g_0^A cor-

responds to the anti-causal Fourier-space Green's function (i.e. the advanced Green's function) and g_0^R corresponds to the causal Fourier-space Green's function (i.e. the retarded Green's function).

The causal and anti-causal versions represent two field distributions. The advanced function represents a spherical wave expanding around a point source while the retarded function represents the same point source with a spherical wave contracting onto it. In real space, these two scenarios are related by:

$$g_0^R(\vec{r}, \vec{r}_0; k_0) = g_0^A(\vec{k}; k_0)^* \quad (1.17)$$

and thus the direct space functions can be written generally as:

$$g_0^{R,A}(\vec{r}, \vec{r}_0; k_0) = -\frac{1}{4\pi|\vec{r} - \vec{r}_0|} e^{\pm ik_0|\vec{r} - \vec{r}_0|}. \quad (1.18)$$

For all real scenarios (i.e. causal), the retarded form must be used, allowing us to write (1.14) as:

$$E(\vec{r}) = \int d\vec{r}' j(\vec{r}') g_0^R(\vec{r}, \vec{r}'; k_0). \quad (1.19)$$

1.2.1 Single Scattering

The processes and mathematics that describe a single scattering event are all that is needed to understand much more complex behavior, such as multiple light scattering and photonic transport. That said, we now describe the theoretical backbone that describes single scattering.

For a single scatter, we must add a single scattering potential, V . Thus, (1.15) becomes:

$$[\nabla^2 + k_0^2]g(\vec{r}, \vec{r}_0; k_0) = \delta(\vec{r} - \vec{r}_0) + V_1(\vec{r})g(\vec{r}, \vec{r}_0; k_0). \quad (1.20)$$

Here, the scattering potential is equal to $-k_0^2\alpha(\vec{r})$. The newly added term can be considered the source-term for the wave equation, and we can thus use (1.19) to rewrite the

wave equation as:

$$g(\vec{r}, \vec{r}_0; k_0) = g(\vec{r}, \vec{r}_0; k_0) + \int d\vec{r}_1 g_0(\vec{r}, \vec{r}_1; k_0) V_1(\vec{r}_1) g(\vec{r}_1, \vec{r}_0; k_0) \quad (1.21)$$

This states that the radiated field is proportional to the total local electromagnetic

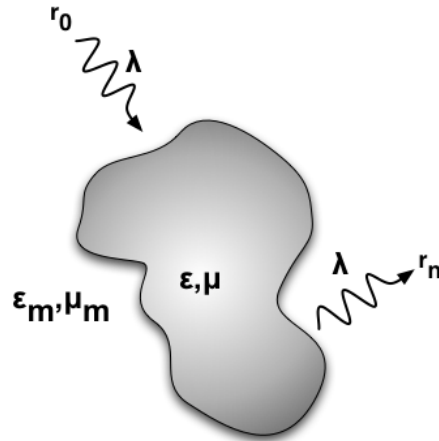


Figure 1·4: Light scattering at a single arbitrary particle

field. This suggests an iterative approach is necessary as the radiated field will thus immediately influence the total local field and in turn the radiated field (as depicted in Figure 1·5). Successive terms can be developed recursively by expanding (1.21) in the



Figure 1·5: Depiction of the iterative self-energy process.

same manner that it was initially derived. Thus, we can express the solution to the wave

equation as the expansion of the Green's function:

$$\begin{aligned}
g(\vec{r}, \vec{r}_0; k_0) = & g(\vec{r}, \vec{r}_0; k_0) \\
& + \int d\vec{r}_1 g_0(\vec{r}, \vec{r}_1; k_0) V_1(\vec{r}_1) g(\vec{r}_1, \vec{r}_0; k_0) \\
& + \int d\vec{r}_1 d\vec{r}_2 g_0(\vec{r}, \vec{r}_2; k_0) V_1(\vec{r}_2) g_0(\vec{r}_2, \vec{r}_1; k_0) V_1(\vec{r}_1) g_0(\vec{r}_1, \vec{r}_0; k_0) \\
& + \dots
\end{aligned} \tag{1.22}$$

We can make this formulation easier to read by introducing a diagrammatic notation.
Let us make the following substitutions:

$$g_0 = — \tag{1.23}$$

$$V = \circ \tag{1.24}$$

This notation is sometimes referred to as Feynman notation and using this we represent (1.22) as:

$$g = — + — \circ — + — \circ \curvearrowleft \circ — + — \circ \curvearrowleft \circ \curvearrowleft \circ — + \dots \tag{1.25}$$

Scattering events grouped together with the \curvearrowleft symbol represent scattering events occurring on the same scatterer.

This equation clearly depicts the utility of the Green's function. It allows us to represent the field going from r_0 to r as the sum of two quantities: non-scattered field radiated by original source and scattered field from single scatterer (fully accounting for iterative radiation effects). This notation eloquently describes the processes of the single scatterer, and due to it's generality, can be expanded upon to provide a tool for understanding multiple scattering systems.

1.2.2 Multiple Scattering

We now begin in an environment with more than one scatterer, randomly distributed over some real space. The solution from this problem requires no additional knowledge beyond that of free-space propagation and single scattering. A redefinition of the

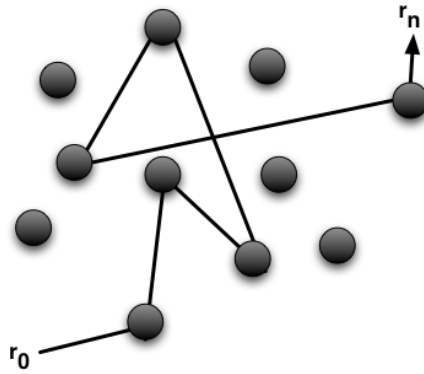


Figure 1·6: Multiple scattering through an arbitrary collection of particles

scattering potential allows us to transform the single scattering problem into a multiple scattering one. Recall:

$$g(\vec{r}, \vec{r}_0; k_0) = g(\vec{r}, \vec{r}_0; k_0) + \int d\vec{r}_1 g_0(\vec{r}, \vec{r}_1; k_0) V_1(\vec{r}_1) g(\vec{r}_1, \vec{r}_0; k_0). \quad (1.26)$$

However, we now set our scattering potential to $V(\vec{r}) = \sum_i V_i(\vec{r} - \vec{r}_i)$. This term accounts for the additional $i - 1$ scatterers that are randomly distributed. This can be represented using the diagrammatic notation introduced in the last section and then expanded,

yielding:

$$\begin{aligned}
g = & \quad \text{---} + \text{---} \circ \text{---} \\
& + \text{---} \circ \text{---} \circ \text{---} + \text{---} \circ \overbrace{\text{---}}^{\curvearrowleft} \circ \text{---} \\
& + \text{---} \circ \text{---} \circ \text{---} \circ \text{---} + \text{---} \circ \overbrace{\text{---}}^{\curvearrowleft} \circ \overbrace{\text{---}}^{\curvearrowleft} \circ \text{---} \\
& + \text{---} \circ \overbrace{\text{---}}^{\curvearrowleft} \circ \text{---} \circ \text{---} + \text{---} \circ \text{---} \circ \overbrace{\text{---}}^{\curvearrowleft} \circ \text{---} \\
& + \text{---} \circ \overbrace{\text{---} \circ \text{---}}^{\curvearrowleft} \circ \text{---} + \dots
\end{aligned} \tag{1.27}$$

If we now introduce a single-particle t-matrix, $t(\vec{r}_1, \vec{r}_2)$, which represents the sum of all self-induced scattering from a single scatter, diagrammatically represented as:

$$t(\vec{r}_1, \vec{r}_2) = \times = \circ + \overbrace{\circ}^{\curvearrowleft} \circ + \overbrace{\circ}^{\curvearrowleft} \circ \overbrace{\circ}^{\curvearrowleft} \circ + \overbrace{\circ}^{\curvearrowleft} \circ \overbrace{\circ}^{\curvearrowleft} \circ \overbrace{\circ}^{\curvearrowleft} \circ + \dots, \tag{1.28}$$

we can completely describe the multiple scattering process by,

$$\begin{aligned}
g = & \quad \text{---} + \text{---} \times \text{---} + \text{---} \times \text{---} \times \text{---} \\
& + \text{---} \times \text{---} \times \text{---} \times \text{---} + \text{---} \times \overbrace{\text{---} \times \text{---}}^{\curvearrowleft} \times \text{---} \\
& + \text{---} \times \text{---} \times \overbrace{\text{---} \times \text{---}}^{\curvearrowleft} \times \text{---} + \dots
\end{aligned} \tag{1.29}$$

However, to find the solution to this equation would require knowledge of the location of every single scatterer. This requirement can not be sufficiently met in realistic scenarios and thus we instead look to solving the Green's function averaged over disorder. Such analysis will provide a result that conveys the field transport properties of the medium but does not require specific knowledge of scatterers. By defining the averaged t-matrix

as $T = \langle t \rangle = \langle \times \rangle = \otimes$, we can represent the averaged Green's function as the following:

$$\begin{aligned} \langle g \rangle = G = & \quad \text{---} + \text{---} \otimes \text{---} + \text{---} \otimes \text{---} \otimes \text{---} \\ & + \text{---} \otimes \text{---} \otimes \text{---} \otimes \text{---} + \text{---} \otimes \overbrace{\text{---} \otimes \text{---}}^{\text{---}} \otimes \text{---} \\ & + \text{---} \otimes \text{---} \otimes \overbrace{\text{---} \otimes \text{---}}^{\text{---}} \otimes \text{---} + \dots \end{aligned} \quad (1.30)$$

Here, G is general and is satisfactory for any multiple scattering problem. In direct space:

$$G(\vec{r} - \vec{r}_0; k_0) = g_0(\vec{r} - \vec{r}_0; k_0) + \int \int d\vec{r}_2 \vec{r}_1 g_0(\vec{r} - \vec{r}_2; k_0) \sum(r_2, r_1; k_0) G(\vec{r}_1 - \vec{r}_0; k_0), \quad (1.31)$$

where \sum denotes the self-energy, or the sum of all scattering diagrams that are irreducible(i.e. cannot be represented as two smaller scattering diagrams without splitting a recurrent scattering sequence). This completely represents the Green's function in terms of all possible permutations of single-scattering events that result in a field traveling from \vec{r}_0 to \vec{r} .

1.3 Light Localization

1.3.1 Scaling Theory of Localization

A localized state is a state which is immobile beyond a certain length scale. That is, there is no transport beyond a given length scale. While Anderson developed theory regarding the disappearance of the diffusion constant in infinite systems, we are of course interested in finite systems. Thus, we must consider the conductance of the system, γ . This term gives a quantitative metric on the sensitivity of transport properties to the boundary conditions. It has been shown by Thouless that γ depends on the ratio of the typical system eigenmode width, $\delta\omega$, and the separation distance between two

neighboring modes, $\Delta\omega$ (Thouless, 1974). That is:

$$\gamma = \frac{\delta\omega}{\Delta\omega}. \quad (1.32)$$

Importantly, the mode width, $\delta\omega$, is the inverse of τ_t , the transport time, which is defined as the time needed to propagate between system boundaries. Furthermore, the mode separation distance is found to be the inverse of τ_H , the Heisenberg time, which is the longest possible time before light retraces a location it has already visited. The Heisenberg time can be further described as being proportional to the density of states, L^d , where d is again the dimensionality of the system and L is system size. These leads to the general calculation of transport time:

$$\tau_t = \frac{L^d}{D}. \quad (1.33)$$

Here, as first mentioned in Section 1.1, D is the diffusion constant.

In the localized regime $\gamma < 1$ and thus the width of the modes is less than the mode separation distance. This implies that if the localized system is attached to another system of similar size, the already localized states will not couple to the second system and therefore, waves will stay localized in their own subsystems. This lack of coupling leads to the following conductance equation:

$$\gamma = e^{-\frac{2L}{\xi}}. \quad (1.34)$$

The localization length is captured in the variable ξ .

However, such analysis does not hold for diffusive systems due to significantly larger $\delta\omega$ values. In this scenario, the two subsystems will have coupled modes, thus leading to modes which occupy the full system space. This leads to an alternative conductance

proportionality relation of

$$\gamma \propto \frac{\delta\omega}{\Delta\omega} = L^{d-2} \quad (1.35)$$

Taking the natural logarithm of equations 1.34 and 1.35 leads to

$$\ln(\gamma(L)) = (d-2)\ln(L) \quad (1.36)$$

$$\ln(\gamma(L)) = -\frac{2}{\xi}e^{\ln(L)}, \quad (1.37)$$

for extended and localized states, respectively.

We can now define a metric to characterize the transport of a system. We define the scaling function as:

$$\beta = \frac{d\ln(\gamma)}{d\ln(L)}. \quad (1.38)$$

From this comes two distinct regimes determined by the sign of β . A positive scaling function implies that the transport is diffusive and that increasing the system size will enhance the conductance. Alternatively, a negative scaling function implies the existence of localized waves and dictates that γ decreases with the system size (Barthelemy, 2009).

Utilizing equations 1.36 and 1.37, we can now characterize β into three different regimes as a function of γ :

$$\beta = \begin{cases} d-2 & \text{for large } \gamma \\ 0 & \text{for } \gamma = \gamma_c \\ \ln(\gamma) & \text{for small } \gamma \end{cases}$$

For this, we define γ_c as the critical conductance. This term denotes the limit between the localized transport and diffusive transport. It is interesting to note that this result holds regardless of the dimensionality of the system. The realm of anomalous diffusion exists near the transition between these two regimes. In such a state, both standard diffusion and localization processes are evident, leading to an interesting mix of the two phenomena which is manifested in the notion of anomalous diffusion. The relationship

between β and $\ln(\gamma)$ is shown in Figure 1·7 (Sheng, 1995).

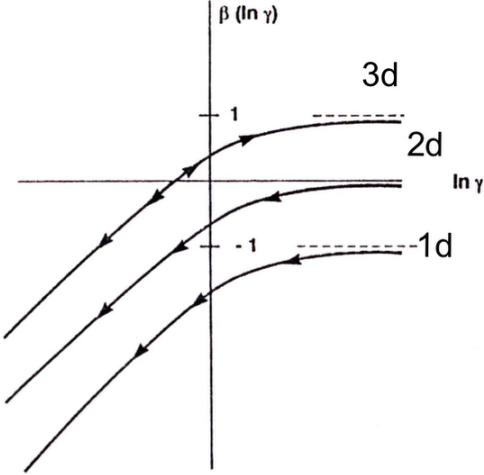


Figure 1·7: Universal scaling function versus conductance for the first three dimensions. Note that for $d = 1, 2 \beta < 0$ always.

1.3.2 Localization in Deterministic Aperiodic Media

The study of aperiodic media and the interest in the properties of deterministic aperiodic systems grew greatly with the experimental discovery of quasicrystals. Their unique properties make them ideal candidates for engineering applications where the disorder normally associated with random systems is desired. While localization has been rigorously studied in random media, in order for us to quantifiably utilize these effects in engineering solutions, we must have a deterministic method of creating localization inducing disorder. To do so, we identify a set of aperiodic arrays, further discussed in Section 1.4 that have demonstrated similar localization behavior (Dulea et al., 1992).

Contrary to photonic crystals (which demonstrate localization based on symmetry breaking defects in the crystal lattice) deterministic aperiodic localized modes are created due to the many nonequivalent localized arrangements of scatterers. These localized arrangements of scatterers introduce a higher level of complexity to the properties of

the critically-localized eigenstates, and thus offer the potential for a higher degree of engineering tunability (Boriskina et al., 2008). Many of these structures mimic the localization phenomena found in fractal structures and, as is true in both of these structure types, the degree of localization is proportional to the complexity of the Fourier spectra of a given array. This matter will be addressed in the coming chapter (Dal Negro et al., 2008).

1.4 Introduction to Deterministic Aperiodic Media

Deterministic aperiodic media give us a tool to introduce disorder in an engineering (tunable) fashion (as opposed to random media). The term 'deterministic' is used to convey the property that these systems can be reproduced and scaled to fit any engineering application without ever becoming translationally periodic. The pioneering work that led to deterministic aperiodic patterns came from symbolic dynamics, number theory, and Lindenmayer systems. As such, these structures have a very rich mathematical theory describing their unique properties.

These media use inflation rules to recursively grow a system to the desired size. Though simple, these rules introduce a very high degree of complexity. This is ideal in that we do not have to wade through difficult generation practices to fabricate these highly disordered systems. The level of disorder for a given system is closely related to its Fourier transform. A periodic system, for example, has a Fourier transform that is characterized by equally spaced delta Bragg peaks, while a random system has a Fourier transform that is flat and is comprised of simple white noise. These Fourier transform of these systems can be seen in Figure 1.8.

Deterministic aperiodic sequences are unique in that they straddle the line between periodic and random. This result is evident in the Fourier transform of such systems. Given this, we can see that this implies it is possible to engineer a deterministic aperiodic

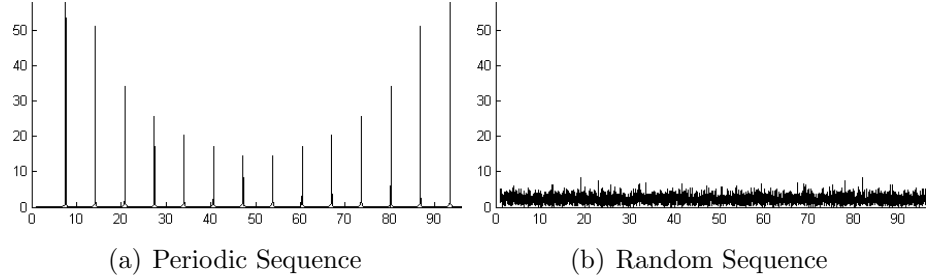


Figure 1·8: Fourier spectra

system to have a Fourier spectra containing any range of disorder that is necessary. In this thesis, three deterministic aperiodic sequences have been focused upon: the Fibonacci sequence, Thue-Morse sequence, and Rudin-Shapiro sequence. As will be shown in the following chapter, the Rudin-Shapiro sequence plays the most interesting role of these three. The generation rules for each of these sequences is as follows:

$$\text{Fibonacci: } A \rightarrow AB ; B \rightarrow A \quad (1.39)$$

$$\text{Thue-Morse: } A \rightarrow AB ; B \rightarrow BA \quad (1.40)$$

$$\begin{aligned} \text{Rudin-Shapiro: } & AA \rightarrow AAAB ; BB \rightarrow BBBA \\ & AB \rightarrow AABA ; BA \rightarrow BBAB \end{aligned} \quad (1.41)$$

where A and B represent the presence and lack of an element, respectively. To create a sequence, one must start with a seed pattern of A and B values, upon which the inflation rules can be applied. The localization and transport properties that arise from these sequences are inherently different and the Fourier transforms of each system (Figure 1.9) are distinctly in between random and ordered; they demonstrate a middle ground between periodicity and random noise. These three structures describe the entire range of disorder between periodic and random.

Generally, Fourier spectra can be organized into three categories: (a) pure point, μ_P (b) singular continuous μ_{SC} and (c) absolutely continuous, μ_{AC} . Furthermore, as

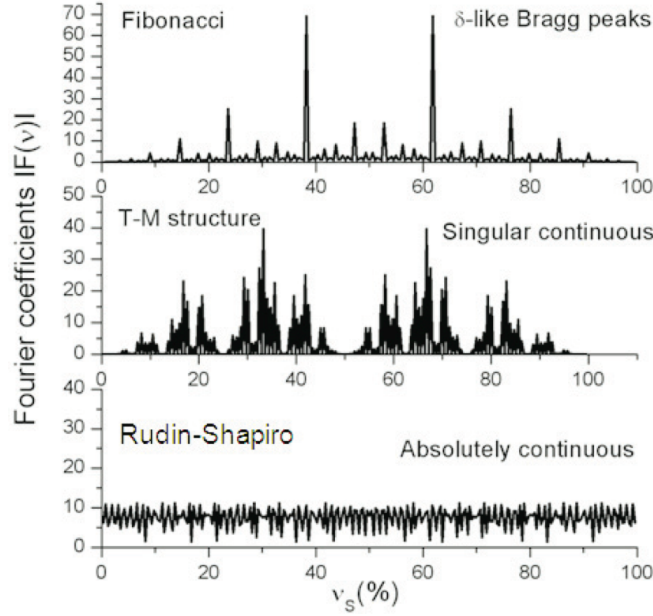


Figure 1.9: Fourier spectra of Fibonacci, Thue-Morse, and Rudin-Shapiro sequences. (Dal Negro et al., 2008)

dictated by Lebesgue's decomposition theorem, the spectrum of any arbitrary physical system can be uniquely decomposed in terms of these three categories, yielding

$$\mu = \mu_P \cup \mu_{SC} \cup \mu_{AC}. \quad (1.42)$$

A pure point system, such as the Fibonacci for example, is characterized by a set of countable peaks, whereas a singular continuous system, such as the Thue-Morse, can be covered by an ensemble of open intervals with arbitrary small total length. Lastly, the absolutely continuous spectrum is characterized by a completely diffuse spectrum, as is the case in the Rudin-Shapiro sequence. It is also important to note that systems can be classified by both their lattice Fourier transform and their Hamiltonian spectrum energy, each of which can assume μ_P , μ_{SC} , or μ_{AC} . This thus yields nine possible categories of lattice types as shown in Figure 1.10. The chart ranges from standard periodic crystals in the upper left corner of the grid, to amorphous systems in the lower right corner. In

	μ_P	Crystalline Matter		Spiral Lattice?
Energy Spectrum	μ_{SC}	Fibonacci Period-Doubling	Thue-Morse	Rudin-Shapiro?
	μ_{AC}	Ideal Quasicrystal		Amorphous Matter
	μ_P	μ_{SC}	μ_{AC}	
Lattice Fourier Transform				

Figure 1.10: Classification of aperiodic systems (Maciá, 2006)

between these two lie the domain of aperiodic systems. It is interesting to note that while Fibonacci, Thue-Morse, and Rudin-Shapiro structures share the same type of energy spectrum, their lattice Fourier transforms differ, thus giving rise to the anticipated differences in transport and localization properties. There is also a caveat regarding the Rudin-Shapiro energy spectrum as denoted by the question mark. The properties of the energy spectra remains an open challenge as numerical studies have suggested that the spatial decay of wave-functions in these lattices is described by an intermediary between power and exponential laws. Thus, the charge distribution of localized electronic states is less spread than that of states in Fibonacci lattices (modeled by a power law), yet the localization degree is weaker than that found in random systems. Thus, for the time being, the Rudin-Shapiro has been placed under the singular continuous energy spectra bracket, but with the inclusion of a question mark to denote that this is not a rigorous characterization of the Rudin-Shapiro Hamiltonian spectrum energy (Maciá, 2006). We now more thoroughly explore the Fibonacci, Thue-Morse, and Rudin-Shapiro structures

in order to establish an understanding of the systems that will be primarily investigated in this thesis. The mechanism for producing both one-dimensional and two-dimensional variations of these sequences is outlined.

1.4.1 Fibonacci Sequence

The Fibonacci sequence is generated using the following inflation rule: $A \rightarrow AB$; $B \rightarrow A$ (Janot, 1997). If we start with a seed value of 'A', this rule generates A, AB, ABA, ABAAB, and so on. This pattern can be additionally generated using

$$n_i = \left[1 + \left\lfloor \left(\frac{i}{w} \right) - \left\lfloor \left(\frac{i+1}{w} \right) \right\rfloor \right], \quad (1.43)$$

where $\lfloor \cdot \rfloor$ denotes the floor function, n_i denotes the n^{th} unit in the sequence and $w = \frac{1}{2}(\sqrt{5} + 1) \approx 1.61803$. The Fibonacci sequence is unique in comparison to both periodic and disordered systems, as suggested through its Fourier transform (Figure 1.9). The Fourier spectra of this sequence contains isolated Bragg peaks with incommensurate periods which broadly fill a wide frequency range. Furthermore, the spectra contains pseudo

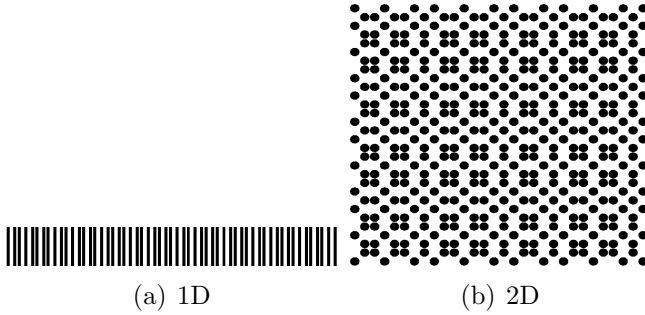


Figure 1.11: Fibonacci Sequence

band gaps, that is, forbidden frequency regions. These pseudo band gaps are induced by strong local structural correlations arising from the disorder of the system and are analogous to the electron behavior in amorphous semiconductor materials. The sequence has been widely studied since its introduction and interesting properties have been

noted. Such properties include its support of transmission scaling (Gellermann et al., 1994) and band edge group velocity suppression (Dal Negro et al., 2003). Furthermore, Fibonacci sequences have been used to demonstrate energy spectra that consist of self-similar Cantor sets with zero Lebesque measure as demonstrated by Janot. Many of these experimental results have been made possible by the experimental realization of the first dielectric Fibonacci quasicrystal structure by Gellerman in 1993 (Gellermann et al., 1994).

1.4.2 Thue-Morse Sequence

The Thue-Morse sequence adds a level of complexity beyond the Fibonacci sequence in that it possesses a singular continuous Fourier spectra. The system is generated using the inflation rule described by Schroeder as $A \rightarrow AB$; $B \rightarrow BA$ (Schroeder, 1991). If we thus start with a seed value, A, we produce A, AB, ABBA, ABBABAAB, and so on. Thue-

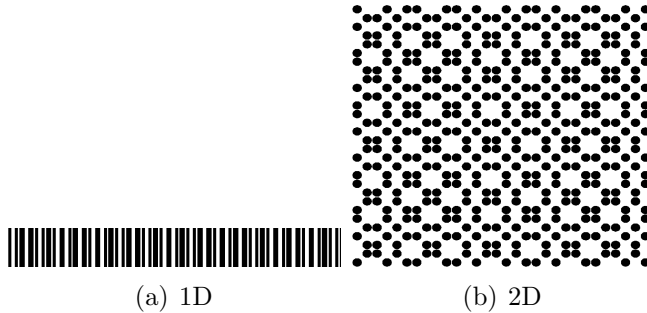


Figure 1.12: Thue-Morse Sequence

Morse structures have been shown to demonstrate a self-similar hierarchy of pseudo band gap regions which are separated by narrow transmission resonance states when assembled in a photonic multilayer structure. Excitement regarding the Thue-Morse sequence is derived, in part, by its fascinating Fourier spectra that demonstrates properties best modeled by multi-fractal systems (Cheng and Jin, 2002). Early experimental work with Thue-Morse structures has focused on omni-direction band-gaps, field localization and

symmetry induced transparency studied through the fabrication of photonic multilayer structures (Dal Negro et al., 2004).

1.4.3 Rudin-Shapiro Sequence

The Rudin-Shapiro aperiodic sequence varies from the Thue-Morse and Fibonacci sequences in that its Fourier spectra is absolutely continuous. The spectra resembles the spectra of a random system (Figure 1.8(b)) in that it has no defining peaks. As might be expected from this close relation, of the three sequences explored, the Rudin-Shapiro sequence shares the most attributes with a randomly generated sequence. In such structures, exponentially localized fields, strong field enhancement, and subdiffusive light transport have been observed. The results regarding subdiffusive transport are of particular interest to this thesis and will be further discussed in the later chapters. The sequence is generated with the following inflation rule: $AA \rightarrow AAAB$; $BB \rightarrow BBBA$; $AB \rightarrow AABA$; $BA \rightarrow BBAB$ (Schroeder, 1985). Of the structures discussed,

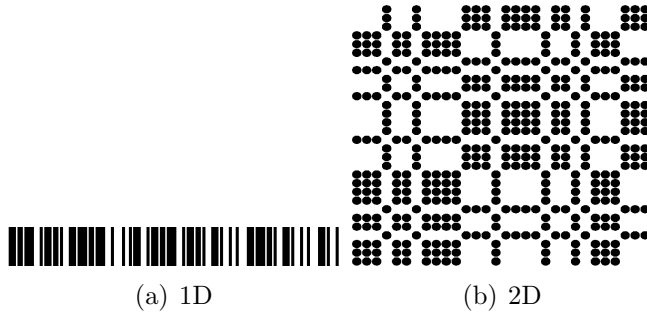


Figure 1.13: Rudin-Shapiro Sequence

the Rudin-Shapiro sequence remains the most unexplored. Little theory, and even fewer experimental results, have been put in the public domain regarding the behavior of photonic Rudin-Shapiro sequences.

1.4.4 Generalization to Two-Dimensions

For the sake of exploring beyond the theoretically studied one-dimensional systems, we need a technique to extrapolate the disordered sequences to two-dimensions while preserving their unique Fourier properties. However, while in the preceding sections we show both 1D and 2D structures, the generation rules only imply how to develop a 1D sequence. The 2D variants require a simple generalization of the 1D sequence into two spatial dimensions. To do so, the inflation rules are alternately executed in orthogonal directions. This guarantees the preservation of the Fourier properties of the 1D systems when extrapolated into higher dimensions. This allows the generations and design of planar (and theoretically 3D) optical devices.

For Fibonacci sequences, two complementary generation rules are used: f_A is used if the unit of inspection in the sequence is an A, and f_B is chosen if the unit is B. These two generation rules are defined as: $f_A : A \rightarrow AB ; B \rightarrow A$ and $f_B : A \rightarrow B ; B \rightarrow BA$.

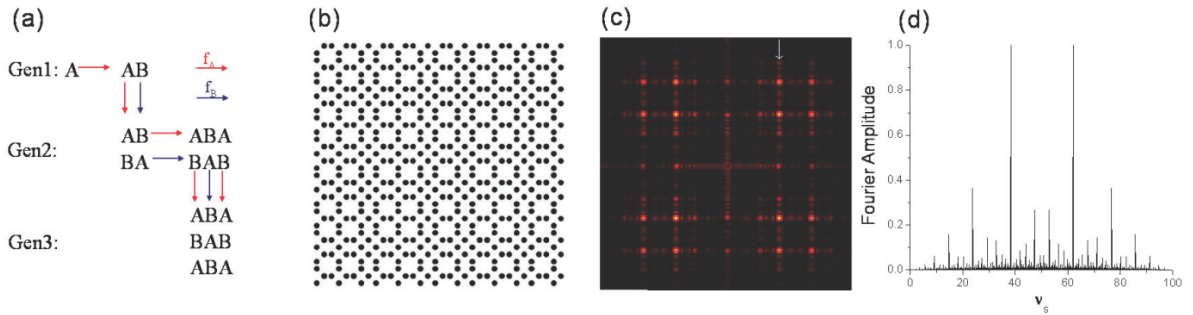


Figure 1.14: (a) Visual representations of 2D generation algorithm, (b) 2D Fibonacci sequence, (c) 2D diffraction spectra, (d) 1D Fourier transfer taken from cutting vertically along arrow in (c). (Dallapiccola et al., 2008)

The generation rules for 2D Rudin-Shapiro and Thue-Morse follow the same general procedure, but follow a slightly different implementation. For Thue-Morse we start with a seed of 'A'. The Thue-Morse inflation rule is then applied along the horizontal direction

to obtain the sequence 'AB'. The same inflation rule is then applied along the vertical direction on each of the elements from the previous step. This produces a 2-by-2 matrix of $\begin{bmatrix} A & B \\ B & A \end{bmatrix}$. The process is then recursively iterated along each row in the horizontal, and sequentially, vertical directions to generate higher orders of the 2D sequence.

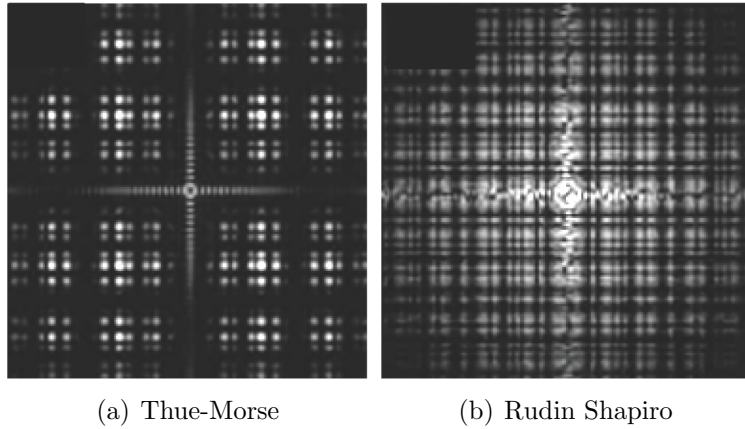


Figure 1.15: Two-dimensional diffraction patterns (Gopinath et al., 2008)

When considering the Rudin-Shapiro 2D generation rules, a similar procedure as that described for Thue-Morse is used, however, a two-letter generation rule is used. Due to this, a 2-by-2 matrix must be used as the seed value. Starting with $\begin{bmatrix} B & A \\ A & B \end{bmatrix}$, the inflation rules are then applied in the horizontal and then vertical directions as detailed in the Thue-Morse procedure.

1.4.5 Aperiodic Spirals

Aperiodic spirals have also been briefly explored during the creation of the material used in this thesis. These structures are known to support circularly symmetric multiple scattering of light, and due to their strong in-plane diffraction, they are a good candidate for slowed diffusion of light. These structures have isotropic, rotationally symmetric Fourier transforms are unique in that they are both translationally and

orientationally asymmetric. The spirals are generated using a simple polar coordinates generation rule. The location of each particle within the spiral is determined by:

$$r = a\sqrt{n} \quad (1.44)$$

$$\theta = n\alpha, \quad (1.45)$$

with $n = 0, 1, 2, \dots$ and $\alpha \approx 137.508^\circ$, which is known as the golden angle. The variable a is a simple constant scaling factor. Additional spiral configurations, aptly named the α_1 and α_2 spirals, are additionally generated by changing the α parameter to $\alpha = 137.3^\circ$ and $\alpha = 137.6^\circ$, respectively. Furthermore, because these aperture angles are irrational fractions of 2π , each of these structures completely lack rotational symmetry. This property explains the diffuse rings found in the Fourier transform. These three spirals are explored briefly in Chapter 3 in hopes of finding unique photonic transport properties due to the strongly asymmetric attributes (Trevino et al., 2011).

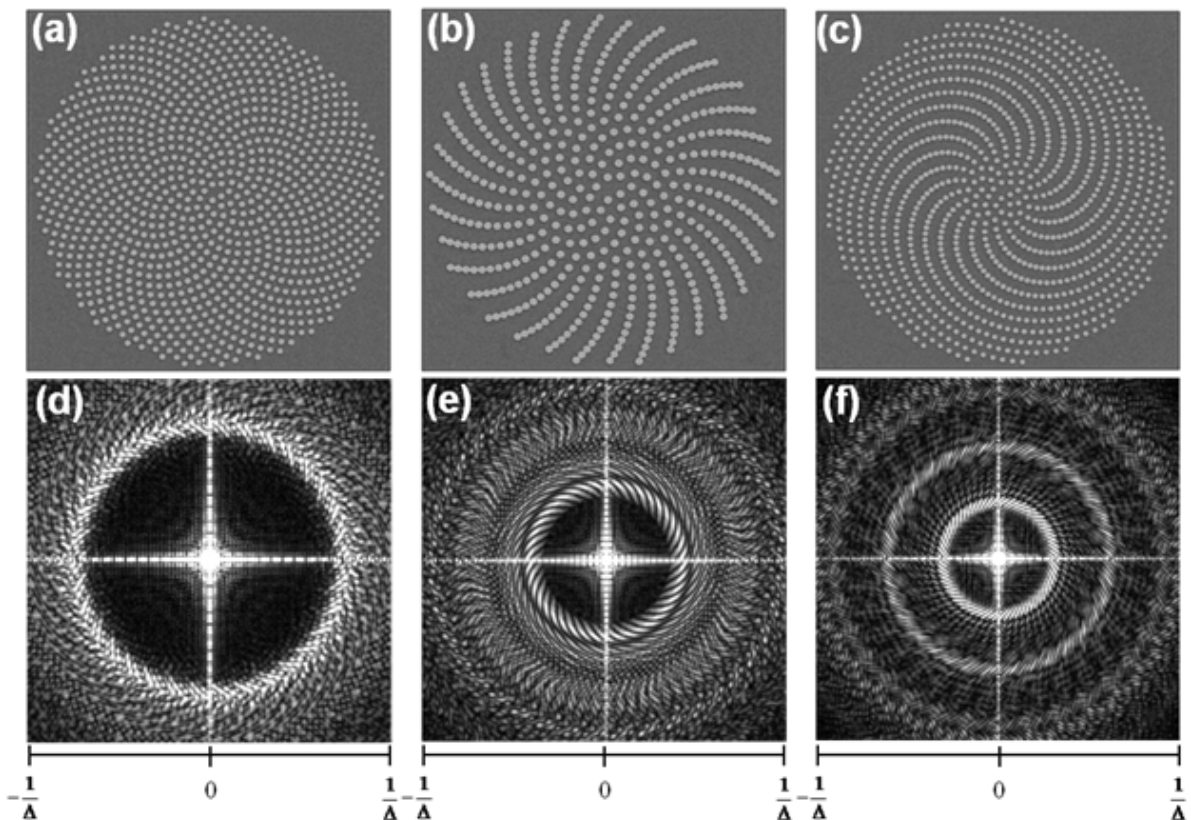


Figure 1.16: SEM micrographs of (a) golden-angle spiral, (b) α_1 -spiral, and (c) α_2 -spiral fabricated from gold nanoparticles of diameter 200nm. The calculated pseudo-Brillouin zones of the (d) golden-angle spiral, (e) α_1 -spiral, and (f) α_2 -spiral. (Trevino et al., 2011)

Chapter 2

Anomalous Transport Theory

2.1 Super- and Sub-Diffusion

Inhomogeneous materials demonstrate an interesting phenomenon of supporting heavy-tailed step distribution of light transport. When this is in the form of a heavy tailed length-step distribution, we are led to superdiffusion. And when this heavy tailed distribution regards the step time distribution, we have slowed transport, dubbed 'subdiffusion'. Together, superdiffusion and subdiffusion are termed 'anomalous diffusion'. A somewhat inappropriate name as the phenomenon is not all at all an anomaly of nature. Many distributions, such as foraging patterns of certain animals, stock market fluctuations, and fluids near turbulent flow demonstration anomalous diffusion behavior (Gouyet, 1996). Standard diffusion is often modeled as a continuous time random walk and using such a construct will be additionally useful here for describing subdiffusion.

Continuous time random walk model that is often used to describe standard diffusion will be useful here for describing subdiffusion (Metzler and Klafter, 2000) . In Chapter 3 we will use a slightly different discrete-time random walk model for the use of numerical simulation, but the general concept is the same. A random walk describes a set of random jumps of arbitrary direction and magnitude in a spatial domain. These steps often follow a step length distribution, $P_s(l)$. The walk is also characterized by the distribution of waiting times a walker experiences at each position. These wait times, τ are given through the waiting time distribution $W(\tau)$. Combining these step-length

distribution and wait-time distribution, we thus have the step distribution, $P_s(l, \tau)$. Given this we can then describe the probability of an arbitrary walker to land at a position r at a given time t as follows:

$$\eta(r, t) = \int_{-\infty}^{\infty} dl \int d\tau P_s(l, \tau) \eta(r - l, t - \tau) + \delta(r)\delta(t) \quad (2.1)$$

We can thus similarly define the probability of the walker to be found at site r at the time t . Knowing that the walker will stay at site r for a time τ this probability is found through multiplying $\eta(r, t)$ and $\Psi(t)$, where $\Psi(t)$ is the probability for the walker to stay put at a given site up to the time t , given by:

$$\Psi(t) = 1 - \int_0^t dt' W(t'). \quad (2.2)$$

The product of these two probabilities is often called the propagator and is denoted by $\mathcal{P}(r, t)$ and is thus given as follows:

$$\mathcal{P}(r, t) = \int_0^t d\tau \eta(x, t - \tau) \Psi(\tau). \quad (2.3)$$

For further consideration of this parameter and its influence on the diffusion of a given system, it is convenient to take the Fourier-Laplace transform of 2.3:

$$\mathcal{P}(q, s) = \frac{1 - \mathcal{L}(W(\tau))}{s} \frac{1}{1 - \mathcal{L}(\mathcal{F}(P_s(l, \tau)))} = \frac{1 - W(s)}{s} \frac{1}{1 - P_s(q, s)}, \quad (2.4)$$

where \mathcal{F} and \mathcal{L} represent the Fourier and Laplace transforms, respectively. We can now separate the step length and waiting time by assuming they are uncorrelated, yielding $P_s(q, s) = P_s(q)W(s)$. Doing so allows us to define σ^2 , the step length variance, and θ ,

the average waiting time.

$$\sigma^2 = \int_0^\infty d\tau \tau W(\tau) \quad (2.5)$$

$$\theta = \int_{-\infty}^\infty dl l^2 P_s(l) \quad (2.6)$$

The three cases, normal diffusion, sub-diffusion and super-diffusion, can then be explained as phenomena sensitive to the choice of σ^2 and θ .

Normal diffusion is seen when σ^2 and θ are both finite. We can then express the propagator as,

$$\mathcal{P}(q, s) = \frac{1}{s + \frac{q^2 \sigma^2}{2\theta}} \quad (2.7)$$

because we are now allowed to make the following expansion:

$$P_s(q, s) \approx 1 - \frac{\sigma^2 q^2}{2} - \theta s. \quad (2.8)$$

In this situation, where the transport obeys the standard diffusion equation, a diffusion constant of $D = \frac{\sigma^2}{2\theta}$ is found. The mean square displacement thus also follows standard diffusion properties and varies linearly with time, as given by:

$$\langle r^2(t) \rangle = Dt. \quad (2.9)$$

If we now instead have a diverging average waiting time, θ , while the step length variance remains finite, the standard diffusion equation will no longer hold and we will instead see subdiffusive behavior. In this situation the waiting time must instead be approximated as $W_t(s) \approx 1 - (s\theta_\beta)^\beta$. Here, β is the highest finite fractional moment of the distribution and must be on the range $0 < \beta < 1$. In real time space this correlates

to a waiting time distribution given by $W(\tau) \approx \frac{\theta_\beta}{\tau^{\beta+1}}$, yielding:

$$\mathcal{P}(q, s) = \frac{1}{s} + \left(1 + \frac{q^2 \sigma^2}{2\theta_\beta^\beta s^\beta} \right)^{-1}. \quad (2.10)$$

As is characterizing of a subdiffusive system, this propagator equation leads to a mean square displacement that grows less than linearly with time:

$$\langle r^2(t) \rangle = D_\beta t^\beta. \quad (2.11)$$

The superdiffusion regime is characterized by a waiting time average that has a finite average and a step length distribution that decays with as a power-law curve. This leads to a step distribution of

$$P_s(q) \approx 1 - \sigma_\beta^\beta |q|^\beta, \quad (2.12)$$

with asymptotic behavior described by $P_s \approx |l|^{-(1+\beta)}$ where $0 < \beta < 2$. The propagator is thus once again altered and is given by,

$$\mathcal{P}(q, s) = \frac{1}{s + \frac{\sigma_\beta^\beta}{\theta} |q|^\beta} \quad (2.13)$$

This propagator describes a Lévy distribution (Barthelemy et al., 2008) that has a diverging mean square displacement. The mean square displacement for any arbitrary Lévy Flight can however be described with:

$$\langle r^2(t) \rangle = \int_{L_1 t^{1/a}}^{L_2 t^{1/a}} dx x^2 \mathcal{P}(x, t), \quad (2.14)$$

where L_1 and L_2 define the limits of the initial position of the walker (Jespersen et al., 1999).

These three different cases are effectively depicted in Figure 2·1, which categorizes

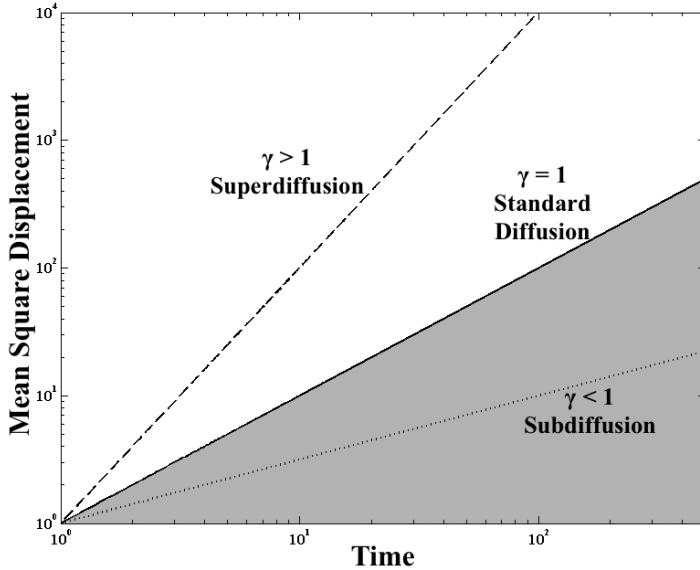


Figure 2·1: The three diffusion regimes as described by analysis of the mean squared displacement versus time.

each regime of transport by the time dependence of the mean squared displacement.

This yields the general equation:

$$\langle r^2(t) \rangle = D_\gamma t^\gamma. \quad (2.15)$$

Regular diffusion, subdiffusion, and superdiffusion are thus categorized by a time exponent of $\gamma < 1$, $\gamma \approx 1$, $\gamma > 1$, respectively (Barthelemy, 2009).

2.2 Sinai Logarithmic Sub-Diffusion

In 1982 Sinai first discovered the conditions that cause standard diffusion laws to break down and the mean square deviation becomes $\langle r^2(t) \rangle \propto \log^4(t)$. Such a phenomenon has since been coined 'Sinai Diffusion'. Sinai found this logarithmically slow diffusion using a 1D random walk model. A random walker is located at an arbitrary location along this 1D environment and at each site it experiences a random bias field $E = p_+ - p_-$.

We define p_+ and p_- as the transition probability of taking a step to the right and left, respectively. Furthermore, it is important to note that $p_+ + p_- = 1$. The underlying mechanism that causes this significantly slowed diffusion is the uncorrelated disorder within the bias field. Were the bias field to be uniform, the random walker would experience standard diffusion and thus propagate with $\langle r^2(t) \rangle \propto t^2$ (Stanley and Havlin, 1987).

Furthermore, Stanley and Havlin have since demonstrated the generalization of Sinai's Diffusion law. That is, by applying a simple generalization to Sinai's random walk model, it is possible to create systems with actively tunable transport exponents, given by:

$$\langle r^2(t) \rangle \propto \log^{2y}(t) \quad (2.16)$$

The y exponent becomes controllable and the system thus has finely tunable transport behavior. The generalization is similar to the Sinai model in that with each site there is an associated random bias field of quantized value $+E_0$ or $-E_0$. However, in contrast to Sinai's original model, Stanley and Havlin now introduce long-range correlation between the bias fields on each site. To do this, each site is no longer assigned a random bias field, but groups of sites of length k are assigned a single random bias field. The value of k is determined from the power law distribution:

$$P(k) = k^{-\beta}, \quad (2.17)$$

where $\beta > 1$.

If we now consider a segment of the site lattice made up of S strings and l sites, where E_i and k_i are the field acting on all k_i sites of string i , we will find that this produces a normal random walk, given that each site is occupied by a bias of only $+E_0$ or $-E_0$. The random walk is identical to standard models in that the walker takes a step of unit length for any given time interval. However, the correlation is the values of

the random bias fields indirectly introduces long-range correlation in the random walk steps. Thus, the net bias, $E(S)$, of the S-string system is given by

$$E(S) = \sum_{i=1}^S E_i k_i \sim \begin{cases} S^{1/\beta} & \text{if } (1 < \beta < 2) \\ S^{1/2} & \text{if } (\beta > 2). \end{cases} \quad (2.18)$$

The value $E(S)$ is analogous to the total displacement of a Lévy flight after S time steps.

The transport properties of this system are dictated by the fact that the total time required for the random walker to exit the system of l sites scales exponentially with the net bias field and is given by:

$$t_{exit} \sim e^{E(S)}. \quad (2.19)$$

To study the diffusion of such systems further, we replace S for l given that $S \sim l^{\beta-1}$ for $1 < \beta < 2$ and $S \sim l$ for $\beta > 2$. This results in the following summation equation:

$$l = \sum_{i=1}^S k_i \sim S \int_1^{k_{max}} k P(k) dk. \quad (2.20)$$

This process allows us to find how k_{max} scales with S , enabling the combination of equations noting that t_{exit} is the time required to cover a region of l sites. This leads to the Sinai anomalous diffusion law of

$$R \sim \log^y(t) \quad (2.21)$$

where

$$y = \begin{cases} \frac{\beta}{\beta-1} & \text{if } (1 < \beta < 2) \\ 2 & \text{if } (\beta > 2). \end{cases} \quad (2.22)$$

It is important to note that as β asymptotically approaches 1, the frequency of strings

with many sites l whose random bias fields are identically oriented increases without limit, thus causing the y exponent to diverge. When the length of a string, l , is larger than the region in which the walker could possibly exist, the process becomes a standard biased random walk (i.e. $d_w = 1$).

Sinai transport represents an exciting opportunity if it can be applied to photonic systems as it is of great interest for both device engineering and fundamental physics knowledge. The actively tunable exponent enables the creation of application specific light-matter coupling interactions and transport properties, which is immediately relevant towards applications such as optical sensing, nonlinear integrated photonics, and solar-cells. Through the use of multi-layered dielectric structures, specifically the use of aperiodic structures with consecutive identical biases, we can achieve the string biasing that is described by Havlin's generalization of Sinai diffusion. This will allow us to bridge the gap between the Sinai mathematical model and physical photonic structures.

Chapter 3

Random Walk Modeling of Photonic Transport

3.1 Random Walk Simulations

When considering the propagation of classical waves through elastically scattering media, a scenario where the energy of the wave is conserved, the transport of the energy density is slowed due to scatterers (i.e the energy velocity is slowed) and can be described using the diffusion theory. Diffusion equations typically disregard interference effects between multiply-scattered waves, and when we neglect these interference effects, a random walk argument becomes applicable for describing the transport properties of the system.

In classical diffusion problems, the motion of a walker is characterized by the mean free path, l . This length depends on the scattering cross section σ_s and the scatterer density n . This yields $l = 1/n\sigma$ as previously mentioned in 1.1. Most importantly, at various levels of disorder, the mean free path of a random walker gets reduced to a level such that localization effects exist. Such systems provide a good first-order analog to the behavior we are set to explore in our photonic systems (Lagendijk and Dainty, 1999). Simulations of this random walk problem allow us to look at an ensemble average of walkers, allowing us to converge towards a steady state distribution of transport properties.

3.1.1 Random Walk on Inhomogeneous Complex Media

Random walks have been used to model a wide range of physical phenomena, from thermal motion of electrons in metals and migratory patterns, to disease propagation and, importantly, photon transport. A random walk is a stochastic process defined on a discrete lattice, usually over a discrete time interval. At each time step, the walker steps from its current location to another site in the lattice following a prescribed behavior. The behavior of the walker (i.e. its present and future steps) are independent of the past steps and thus, the process is Markovian. The mean square displacement can be obtained from a walker's probability density function, $P(r,t)$ defined as probability of finding a walker at a position r at a time t . This density function is obtained through $\langle r^2 \rangle \propto \int r^2 P(r,t) dr$.

The probability density function for a hypercubic lattice is a simple Gaussian (Bunde and Havlin, 1991) and from this knowledge we can define the important parameter $P(0,t)$: the return probability. It has been shown that for the same hypercubic lattice, $P(0,t) \propto \langle r^2(t) \rangle^{-d/2}$, where d is the dimension of the space. For these Markovian situations, the probability density function completely defines the diffusion process, and from it, all transport properties of walker can be calculated. (Ben-Avraham and Havlin, 2000)

Alternatively, random walkers in disordered media behave quite differently. Due to loops, bottlenecks, and other spatial inhomogeneities, the motion of the random walker is slowed down on all length scales (Barthelemy et al., 2008). Fick's diffusion law (Equation 2.9) breaks down in such scenarios. For fractals and percolation clusters, random walkers fall into the anomalous sub-diffusive regime characterized by the mean square displacement scaling as a power law, $\langle r^2 \rangle \propto t^\beta$ where $\beta < 1$ (rather than linearly as dictated by Fick's law). Such behavior arises because the process is no longer Markovian - there is now a correlation between successive steps due to the fact that

different sites are non-equivalent. This phenomenon is general and can be observed over a wide range of disordered materials. Our random walk work is ultimately set to uncover these same properties in deterministic aperiodic sequences.

3.2 Percolation Clusters

The notion of percolation clusters began with the simple question: 'if a space comprised of discrete locations is randomly occupied with a filling fraction of p , what is the probability that a continuous path of occupied sites stretching from one end of the space to the other exists?' In this sense, the question is asking about the probability of a particle to percolate through a system that only allows transport on p percent of it's surface (or volume). To begin exploring this question, it is common to consider an infinite system. The question then becomes whether or not there is an infinite cluster, a path comprised of occupied sites that is of infinite length and allows transport from one side of the system to the other. As dictated by Kolmogorov's zero-one law, the probability of an infinite cluster existing for any given p is either 0 or 1. This then implies the existence of a critical threshold, p_c below which an infinite cluster has zero probability of existing and above which an infinite cluster exists with probability 1. This of course only holds for infinite clusters. Clusters of finite size do not have a perfect delta-function switch, but rather a gradual transition from probability 0 to probability 1 as the critical threshold is crossed. The aforementioned percolation scheme is referred to as a site percolation. Another type, bond percolation, exists where rather than having sites that either allow or deny travel, there are connections between adjacent sites that represent the ability to travel from one site to the next.

Percolation clusters are relevant to the work of this thesis because they allow us to vary the degree of disorder within a system. In contrast to deterministic aperiodic sequences, which can also be used in order to control the level of disorder within a

system, percolation clusters are randomly generated and thus non-deterministic (Sheng, 1995).

To generate a randomly distributed percolation cluster, we begin by defining a 2D array of uniformly distributed random numbers on the open interval $(0,1)$. The percolation variable, p , is set on the closed interval $[0,1]$. Every number is then compared in the 2D random array to p . Numbers less than p are set equal to 1 and numbers greater than p are set equal to 0. This yields a 2D array where $p\%$ of the numbers equal 1 and $(1-p)\%$ of the numbers equal 0. A 1 represents an occupied site in the 2D lattice (the equivalent of an 'A' value from the discussion on aperiodic media in Section 1.3.2) . A random walk can then be executed on a percolation cluster in order to identify the transport properties associated with the designed level of disorder.

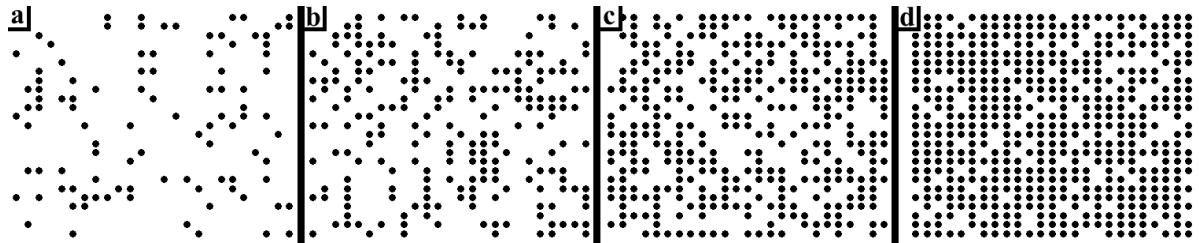


Figure 3.1: Four different percolation clusters with values of p = (a) 0.15, (b) 0.35, (c) 0.60, and (d) 0.85

As shown in 3.2, we are able to transition between ballistic transport (identified by a slope equal to 1) at low fill-fractions to localized regimes (identified with a slope equal to 0) at higher fill-fractions. Such results allow us to draw connections between the level of disorder and the transport behavior. The intermediary positions yield transport properties that are clearly in between ballistic and localized transport - i.e. subdiffusive. Transport on percolation clusters with $p = 0.59$ and 0.65 yield clearly subdiffusive behavior, which is consistent with theory regarding random systems displaying anomalous diffusion at high disorder levels (Ben-Avraham and Havlin, 2000). The data is fit with a

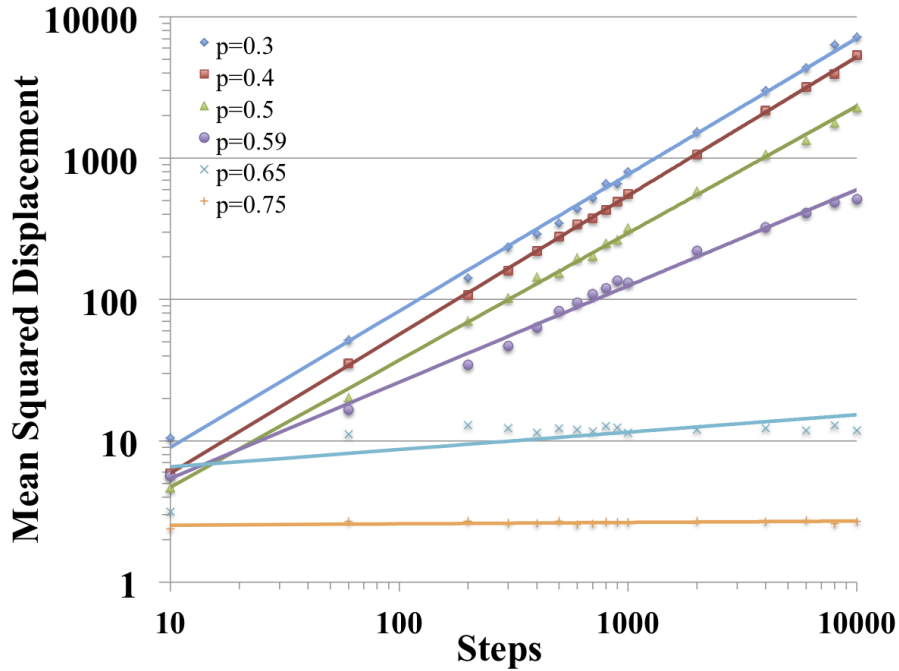


Figure 3.2: Mean Squared Displacement, $\langle r^2(t) \rangle$ versus Steps. Power Law fits yields exponents for $p = 0.3, 0.4, 0.5, 0.59, 0.65, 0.75$ of $\beta = 0.96, 0.98, 0.89, 0.68, 0.12, 0.01$ respectively.

power law, $y = a * x^b + c$, where b is the parameter we take for β (our diffusion exponent).

The data is calculated by taking an ensemble average of many ($> 10^5$) single random-walk simulations. We now move beyond random systems to study random walks in 1D and 2D aperiodic sequences.

3.3 One-Dimensional Systems

We begin our exploration by running one-dimensional random walks on an open lattice. Such random walk simulations provide a baseline to compare our later results to. These simulations will also serve to verify that the simulation and algorithm correlates to what has been theoretically provided in literature. The 1D random walk begins by generating an array of random numbers uniformly distributed between 0 and 1 (exclusive). A

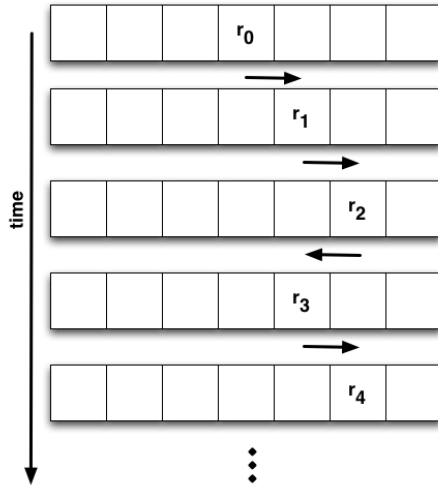


Figure 3.3: Random walk implementation on an open 1D grid

threshold value is defined and the values in the array of random numbers are compared to this threshold. Numbers above the threshold are replaced with a 1 (representing a step to the right) and numbers below the threshold are replaced with a -1 (representing a step to the left). The threshold is typically set at 0.5 to produce an even probability of stepping left or right, but the threshold can be changed if a bias is desired. On an open grid, summing the first N numbers in the array of left and right steps (1s and -1s) yields the random-walker's position after N -steps. The variable $iter$ is defined which represents the number of iterations over which the mean square deviation is averaged. For each count in $iter$, the above process is repeated.

The result of these simulations matches the theoretical literature as the probability density function is shown to be a Gaussian distribution that stretches over time (Figure 3.4). Further matching the literature on the subject, we show that the probability of being at the original location ($r = 0$) decreases exponentially as time progresses. This results in a significant level of stretching in the Gaussian distribution over short time intervals at early times and then a much slower stretching of the distribution over the

same time interval at larger times (notice the larger time steps that are required in Figure 3·4 to achieve a similar degree of stretching). These results match the theory and gives us confidence in the random walk algorithm that is used.

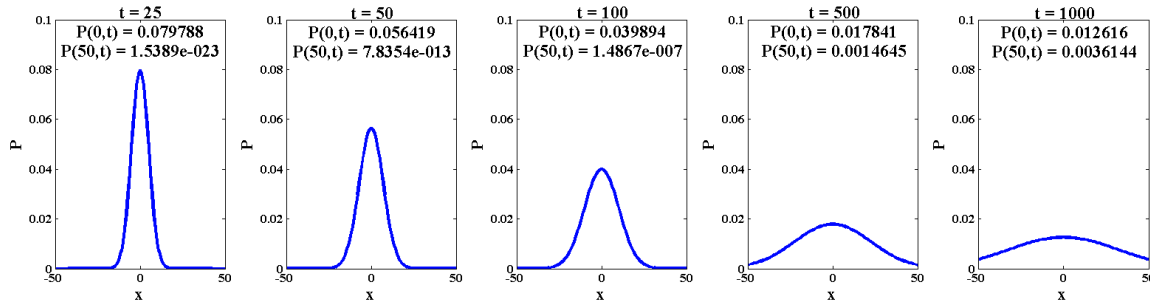


Figure 3·4: Probability Density function at five different time intervals

Of course, this thesis is really interested in walks on occupied lattices, that is, arrays with disorder. Unfortunately, we can not simply keep the same simple procedure of generating a sequence of left and right steps of magnitude 1. When the random-walker is situated on a 1D grid occupied with particles (in either a Fibonacci, Thue-Morse, Rudin-Shapiro, or other disordered pattern), simple steps of one-unit left or right will not suffice. Doing so will trap our random walker in between its two nearest neighbors, thus placing a limit on its deviation distance regardless of time. To combat this, rather than steps of -1 or 1, the step length is defined by a Gaussian distribution of mean 0 and variance 1. A random array of Gaussian distributed numbers is generated. Numbers below zero are floored (yielding -1,-2,-3, ...) and numbers greater than 0 are rounded up (yielding 1,2,3, ...). This produces an array of integer values normally distributed about 0 with a variance of 1, with the probability of taking a step of zero-length equal to zero. For each step in the sequence, the proposed new location of the random walker is compared to the respective lattice. If a spot is occupied on the lattice (represented by a 1), the random-walker does not jump to the new spot, otherwise, if the new location is empty, the walker moves to the new location. The deviation distance is calculated by

looking at the final position of the random walker after N-steps and comparing it to the original location of the walker.

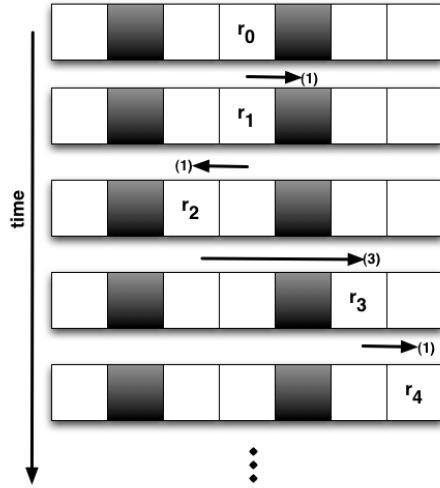


Figure 3·5: Random walk implementation on an occupied 1D grid

The random walks are conducted on six different arrays. In addition to the previously described Fibonacci, Thue-Morse, and Rudin-Shapiro sequences, the random walk operates on a homogeneous (all locations unoccupied), periodic (every other location is occupied - i.e. ABABAB...), and random sequence (populated using the same technique as described for percolation clusters in Section 3.2). The simulation again performs many ($> 10^5$) iterations of the random walk in order to find an ensemble average. The resulting data representing the mean square displacement versus number of steps is shown in Figure 3·6. We fit power law curves to each set of data in order to find the β exponent of interest. Again use $y = a * x^b + c$ as our fitting equation. The Fibonacci, Thue-Morse, homogeneous, and periodic sequences all demonstrate ballistic transport as indicated by $\beta \approx 1$. Of interest instead are the Random and Rudin-Shapiro curves which show markedly decreased β exponents. The data from these two sequences is plotted with respect to natural logarithm of the steps, which yields straight lines, thus

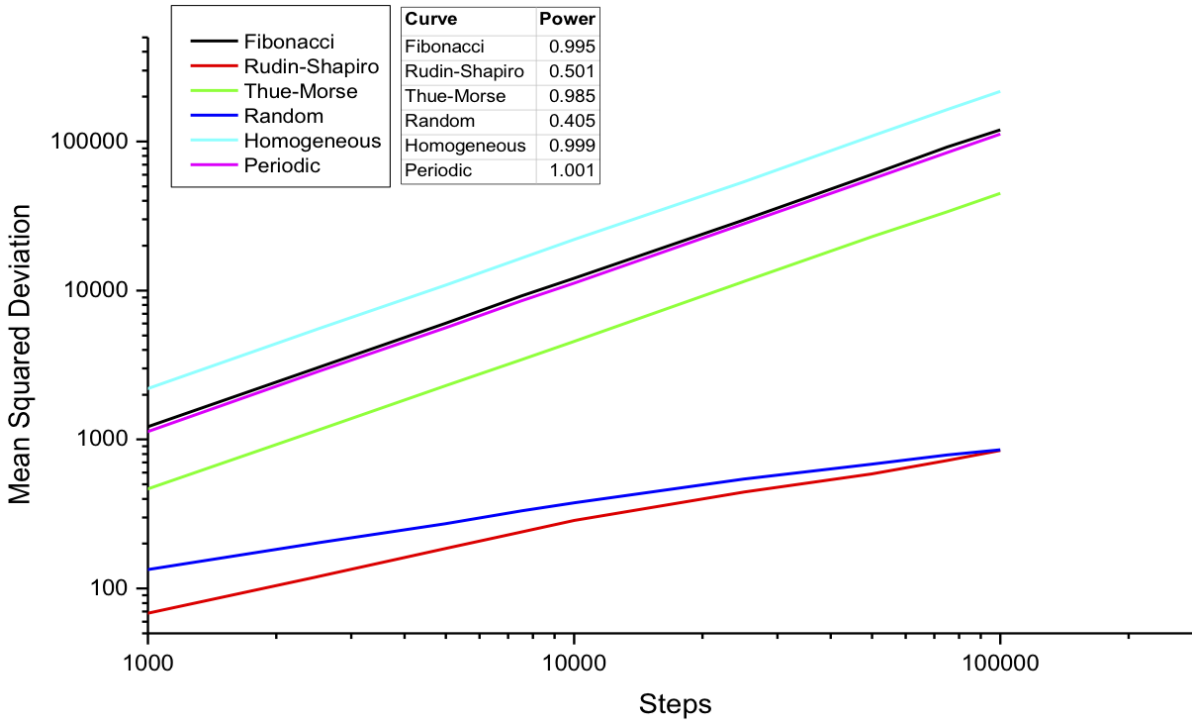


Figure 3·6: Mean square displacement versus Number of steps taken.

implying the logarithmic relation we seek for Sinai diffusion (Figure 3·7). This serves as a strong indicator that the Rudin-Shapiro structure may support Sinai diffusion in both 2D random walk simulations and electromagnetic simulations.

Random walk simulations in one-dimensional sequences provide a good first order approximation for the transport properties of light in photonic waveguides of aperiodic sections. This work confirms the literature's expectation that subdiffusive behavior can be found in any sufficiently disordered system - i.e. in deterministic aperiodic systems rather than just in random systems. Electromagnetic simulations of these same 1D environments will provide a deeper lever of analysis and will provide a more complete insight into the influence of interference effects and the wavelength dependent nature of the slowed diffusion mechanism. Next, we explore, in a similar fashion, the two-dimensional domain. Theory suggests that localization is still possible in higher dimensions but due

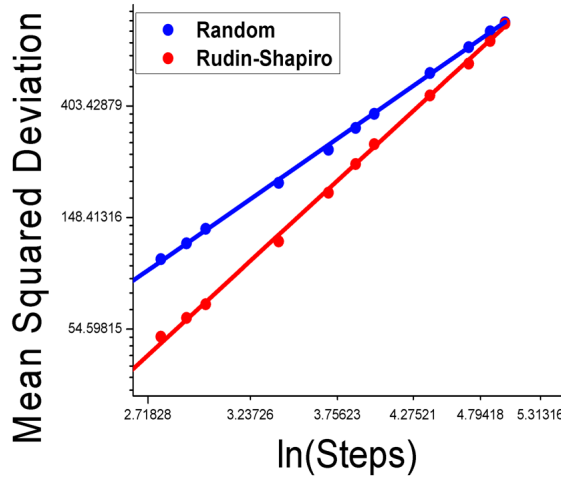


Figure 3.7: Mean square displacement versus Number of steps taken for the Rudin-Shapiro and random arrays plotted versus the natural logarithm of the number of steps taken. Data is the same as from Figure 3.6.

to the extra degree of freedom in movement the parameters and structures that will elicit slowed diffusion are likely to vary.

3.4 Two-Dimensional Systems

The two-dimensional random walk is implemented on the same arrays, with the added addition of three aperiodic spiral patterns (Detailed in Section 1.4.5. The procedure for a random walk in a two-dimensional environment is similar to that of a one-dimensional environment. Two variations of the two-dimensional random walk were explored, a random walk on a grid and a position-based random walk. The latter will be the technique used more heavily and the source of the presented results.

The random walk on a grid begins by generating a 1D array of uniformly distributed random numbers is. The length of the array is equal to the number of steps the random-walker will take. Eight intervals are then defined which represent the direction of the jump to be taken by the random walker (left, right, up, down, downleft, downright,

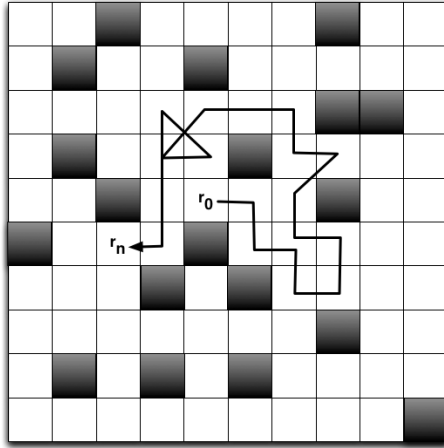


Figure 3.8: Random walk implementation on a 2D grid

upleft, upright). The intervals are weighted such that the probability of taking a step of length 1 is constant, regardless of the direction chosen. The random-walker then iterates through this sequence of jumps. On 2D occupied lattices (i.e. not an open lattice), the proposed new position is compared with the same position in the respective 2D occupied lattice of identical size. If the position in the lattice is occupied, the random walker does not jump, otherwise, if the new location is empty, the random walker moves to that location. By observing the random walker's location after N-steps, we can determine the deviation distance. The variable *iter* is defined which represents the number of iterations over which the mean square deviation is averaged. For each count in *iter*, the above process is repeated. This process is represented in Figure 3.8.

However, this technique is not ideal because it makes several assumptions as to the transport properties of the system, most notably that only orthogonal directions are valid. A more accurate model would be to randomize the length, and the angle at which that length of step is taken (rather than simply choosing one of the 8 cardinal directions). Of course, rather than summing over all direction steps and length, the position of the walker must be tracked at all instances, since it's environment is no longer discretized.

The position-based random walk begins by generating a series of rectangular coordinates that describe the lattice on which the random walker will be moving in (e.g. Fibonacci, Thue-Morse, random, etc.). The random-walker's initial position is defined as $(0,0)$. The variable *steps* is defined as the number of steps that the walker will take. For each count in steps, the random walker will move with a step length of distance a at an angle θ . Here, θ is a uniformly distributed random variable on the open interval $(0, 2\pi)$. The values a and θ are then used to calculate the dx and dy of the random walker for every given step. Summing the random walker's current location and $[dx, dy]$ yields the proposed new location of the random walker.

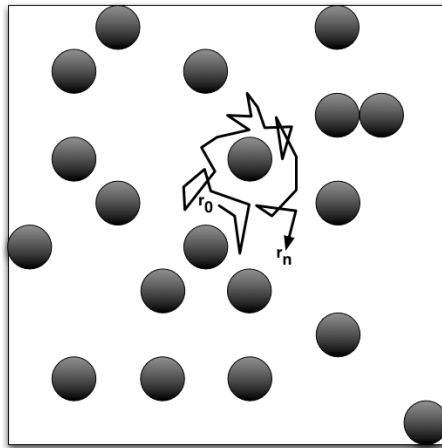


Figure 3.9: Random walk implementation on an unrestricted 2D geometry

Given the random-walker's start-location, end-location, the position of the lattice points, and the radius of each particle at a given lattice point, we can calculate whether the line segment described by the random-walker's start and end location will intersect with any of the particles in the lattice. If the two intersect (i.e. the walker crosses through or lands on a particle), the walker does not take the step. If there is no intersection, the particle takes its move. The deviation distance can be calculated by observing

the walker's position after N-steps. The radius and step-length are user defined, and can be changed to simulate different scenarios.

Figure 3.10 depicts an example of this process being carried out on a spiral array. We show a single random walk event of N steps and the probability density function which is calculated by averaging many single random walk events. This produces a heat map of where the particle is most likely to be found. The simulations are run to a numerical steady state and thus the results can be taken as an average result for any single random walk.

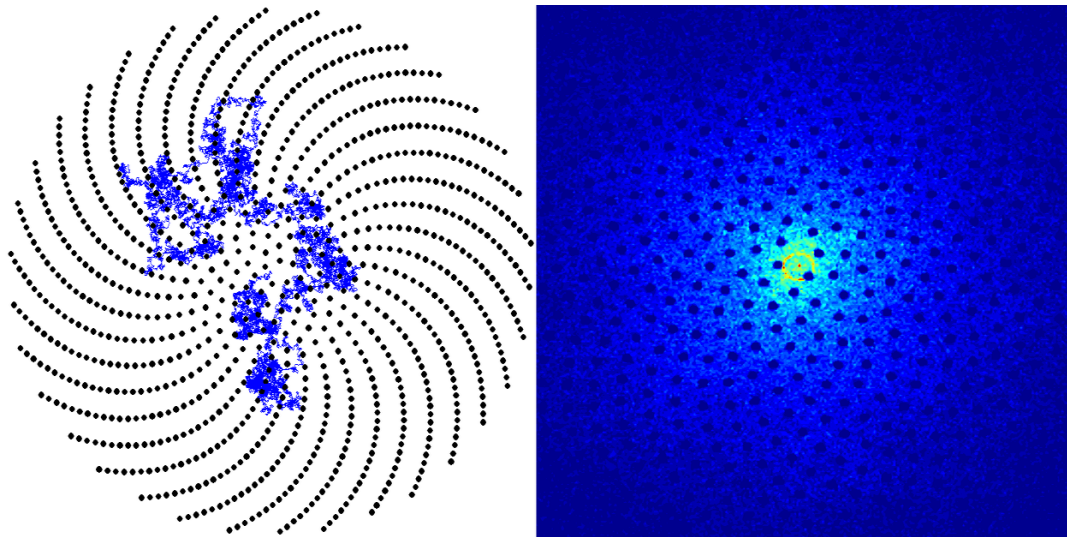


Figure 3.10: A sample single random walk on a aperiodic spiral (left) and the probability density map of an ensemble average of many ($> 10^4$) random walks (right).

In order to have confidence in the simulations and to eventually explore the sub-diffusive nature of the random walker in these systems, there are many parameters we must explore. These include: (a) mean squared deviation versus number of iterations in the ensemble average, (b) mean squared displacement versus starting location, (c) dependence of the step angle on the probability that the step is taken, (d) probability density functions, and (e) mean squared displacement versus number of steps taken.

These metrics will provide useful insight into both the simulation procedure and the nature of the random walker.

It is first useful to gain an understanding of how long it takes these simulations to reach a steady state. To do this the mean squared displacement over a fixed number of steps, N , is calculated. The mean square displacement is then calculated and averaged over $1, 2, 3 \dots, 10^4$ iterations.

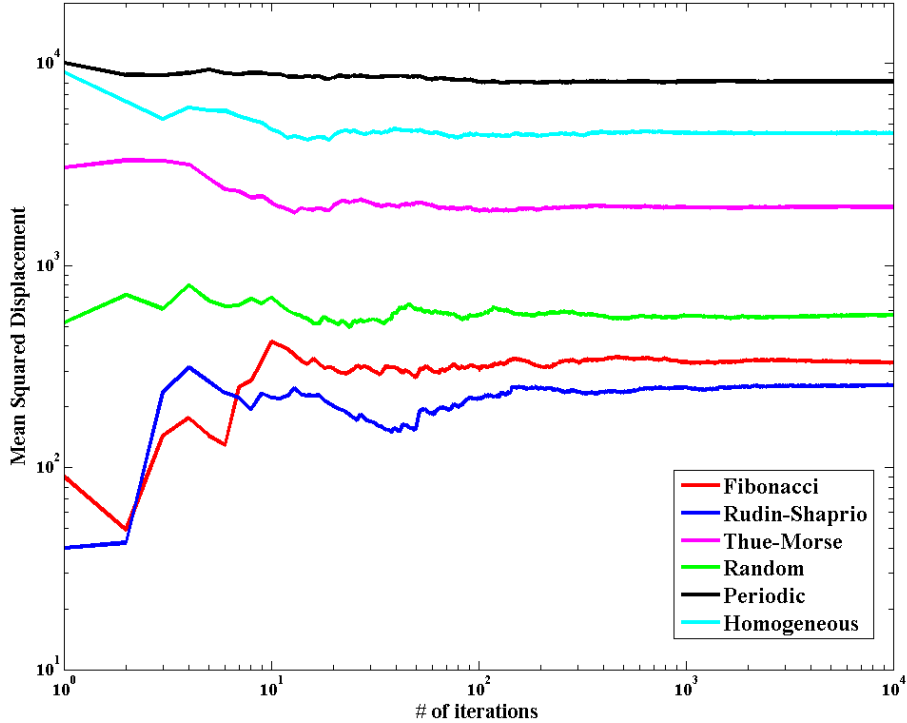


Figure 3.11: Mean Square Displacement versus Number of iterations considered in the ensemble average.

The simulation shows the mean square displacement coming to a steady state near 10^3 iterations and by 10^4 it is very reliably settled (3.11). This analysis was ran this over all array types and though some structures (most notably Rudin-Shapiro and Fibonacci) fluctuate greatly when averaged over only a small sample of random walks, all arrays

settle to a steady average value after 10^4 iterations.

To verify that the simulation correctly distributes the angle at which each step is taken, a history of the angles at which a step was made was recorded over many steps and averaged over many simulations. Note that only the angle of steps that are successfully taken are recorded. The algorithm does not record the angles that result in a step to an occupied space (i.e. a turn in which the random walker does not move). This was run on all the standard structures in addition to the spiral arrays. Plotting the histogram, Figure 3-12, details interesting phenomena.

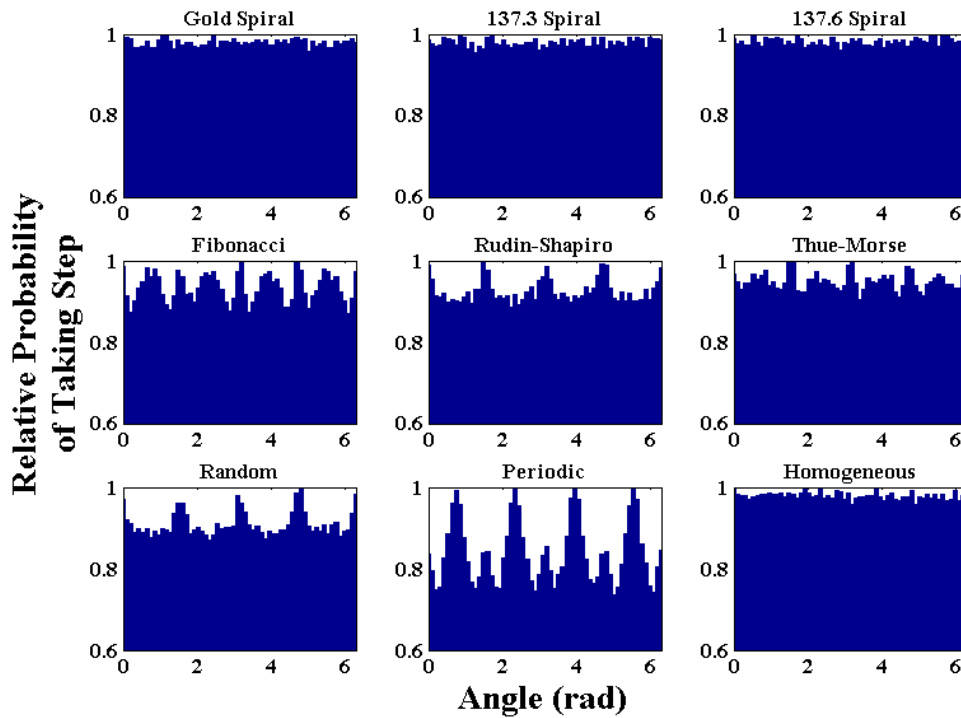


Figure 3-12: Averaged probability of taking a step in a given angle. The function that generates the potential angle at which to step is uniform, but due to occupied lattice spaces, not all are acceptable, hence the non-uniform distributions above.

While the distribution is uniform on the homogeneous structure (i.e. blank structure), several of the disordered structures showed a surprising preference for certain

angles. The uniformity of the homogeneous case suggests that the algorithm is correct and that it is a property of the lattice causing these fluctuations in the disordered lattices. The Periodic lattice shows, not surprisingly, a periodic angle distribution, implying that there are cardinal directions that are preferred. In the case of the disordered lattices, the histograms are distinctly non-uniform and non-periodic. This tells us that for a certain sequence the random walker will have a greater likelihood of moving in certain directions over others. This implies anisotropic scattering, that is, such distributions are what would be expected from scattering in anisotropic media where there exist preferential directions for transport. This is taken more as a point of interest for the time being than a critical term in determining slowed transport phenomena through aperiodic sequences.

It is also important to investigate how a random walker's initial position influences the mean square displacement and transport properties of a lattice. In a homogeneous (i.e. blank) system, we do not expect a walker's initial position to have any effect on its transport behavior. However, in disordered systems since different sites are non-equivalent, it is not guaranteed (or expected) that there will be a uniform behavior across all starting positions. To test this, a random walk simulations are run over a (50x50) grid of starting positions for each of the two-dimensional arrays. Many random walks are launched from each starting position such that an ensemble average can be found and the results can be taken for steady state data. The average mean square displacement over all random walks is tracked for each launch point such that we have a two-dimensional grid of starting locations, each with an associated mean square displacement. The results are shown in Figure 3.13.

As expected, the ordered (homogeneous and periodic) arrays show no variation in mean square displacement over the range of starting points. In contrast, the disordered systems do show a variation in mean square displacement. The phenomenon is most

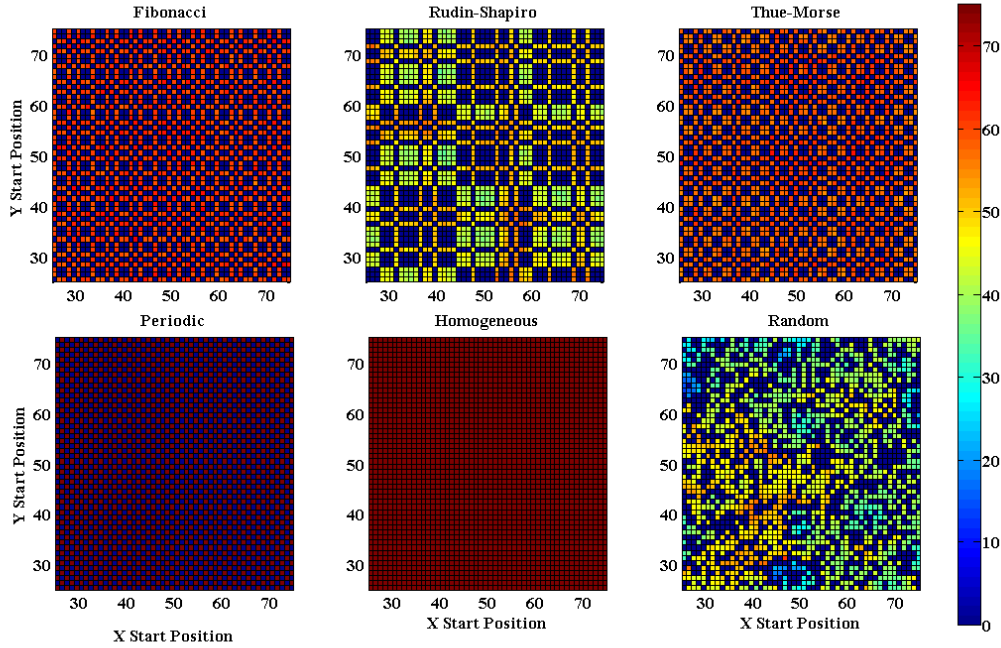


Figure 3.13: Mean Square Displacement versus Starting location. The color bar represents the mean square displacement value.

pronounced in the random and RS systems as shown by the wider range of mean-square displacement values. This correlates to our 1D random-walk results that suggested these two structures would demonstrate the strongest subdiffusive behavior, and we can now have more confidence in explaining this slowed transport as due to the non-equivalent locations; the bottlenecks, loops, and dead ends of these structures have profound influence on the transport of a random walker.

While the previous results suggest anomalous transport and localization effects exist in these structures, it does not explicitly demonstrate these phenomena. In pursuit of this, we now arbitrarily choose a single starting point for each system and calculate the probability density function through numerical simulations. In each case, a random walker is assigned a set starting location and the random walk is run over 10^4 iterations and to find the ensemble average. The probability of the walker existing at any given

location is then calculated knowing the exact path of every random walk. The results are shown in Figure 3.14.

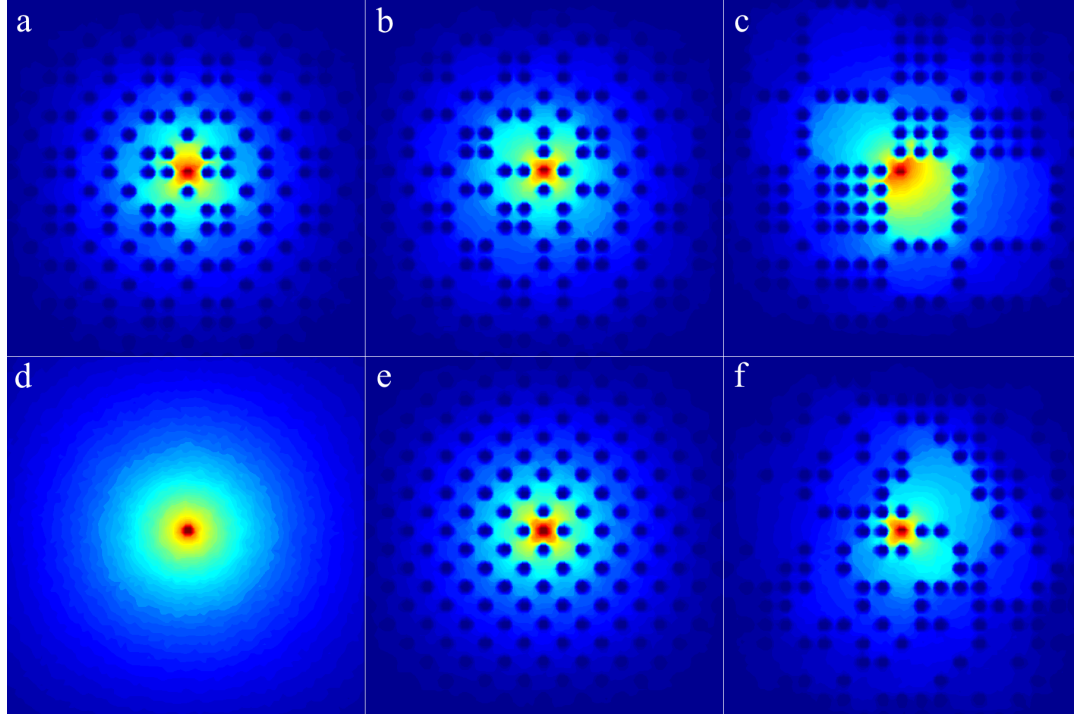


Figure 3.14: Probability density maps. For a given location: Red = higher probability of being found → Blue = lower probability of being found

The homogeneous array displays an expected Gaussian distribution, while the periodic sequence demonstrates a similar density map with the exception of areas of zero probability where particles exist. The disordered structures, alternatively, demonstrate density maps that are decidedly non-Gaussian in distribution. Most notably, again, are the Rudin-Shapiro and random sequences. The random system has a probability density function that is strongly skewed up and to the right, while the Rudin-Shapiro is skewed in several different directions non-uniformly. The Fibonacci and Thue-Morse structures demonstrate similar directional localization or preference, however to a much less significant extent. It should again be noted that these results are for only a single starting location, and are thus not necessarily characteristic of all scenarios involving these ape-

riodic structures, but can be used to demonstrate that they contain features capable of producing non-Gaussian probability density functions and strongly influencing the random walker's transport.

Incorporating this understanding of how these various parameters can influence the behavior of the random walker, we set out to calculated the mean squared displacement as a function of the number of steps taken. We take an ensemble average of many random walks over all structures, averaging over a range of randomly chosen starting locations. This provides an accurate representation of the average transport of the random walker through these structures. As seen in Figure 3·15, the Rudin-shapiro

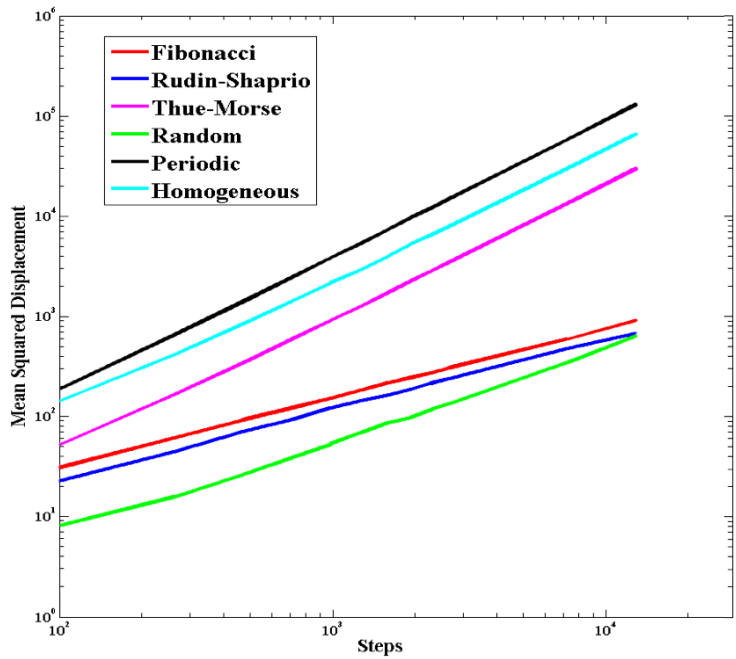


Figure 3·15: Mean squared displacement versus Number of steps taken

and random systems again demonstrate a slower diffusion constant as demonstrated through their lesser slopes. Additionally, the Fibonacci structure shows similar transport behavior to that of the RS structure, which varies from what was found in the 1D case. The slopes of each of these curves, which provide the diffusion exponent, γ , are provided in Table 3.1. Furthermore, several of the curves demonstrate a soft bowing at the

Array	Diffusion exponent, γ
Fibonacci	0.538
Rudin-Shapiro	0.536
Thue-Morse	1.001
Random	0.689
Periodic	1.021
Homogeneous	1.003

Table 3.1: Diffusion exponents as calculated from fitting the data in Figure 3-15

beginning. However, as we are most interested in the long-range behavior (10^3 on) this is not necessarily pertinent to the study of the transport characteristics. The result is, however, interesting to note nonetheless.

These results serve to both confirm our understanding from the one-dimensional simulations and to further our insight into the behavior of these systems. The Rudin-Shapiro and random systems again demonstrate the most potential for slowed diffusion of photons, as demonstrated through their non-ballistic random-walk mean square displacement curves. To further substantiate these candidates, rigorous electromagnetic simulations are necessary, as will be discussed in the coming sections. These random walks, though only a first order approximation that neglects interference phenomena, provide confirmation of the theoretical suggestion that these systems promote sub-diffusive transport behavior, as demonstrated through the results depicted in Figures 3-13, 3-14, 3-15. The following electromagnetic simulations will add to our understanding of these aperiodic environments and allow us to consider the photonic phenomena that will be found in experimental situations.

Chapter 4

Electromagnetic Modeling of Photonic Transport

4.1 Electromagnetic Modeling of Diffusion

Random walk simulations provide an accurate first-order representation of photonic diffusion. The problem is treated in the ray-optics domain, where an electromagnetic field is simplified to a simple unit vector and intensity scalar. Scattering occurrences randomize the direction and calculations are based on this single event. However, as with ray-optics in general, such an approach does not account for numerous electromagnetic (and more generally, wave) phenomena such as interference and polarization effects. To consider such dynamics, a more rigorous electromagnetic simulation model is needed. For such a situation, finite-difference time-domain techniques provide an appropriate tool.

Using this approach we seek to verify slowed electromagnetic diffusion effects that were initially demonstrated by random walk models. Electromagnetic simulations will provide a means to understand the parameters that influence this effect, namely, the impact of refractive index and wavelength. To do this, three types of simulations are used to determine the transport parameters. The metrics by which we will determine the slowed diffusion parameters (D , l_s , etc) are calculated by running simulations to plot (a) transmission spectra, (b) energy density distribution as a function of time, and (c) pulse intensity decay as a function of time. Early results show certain localization

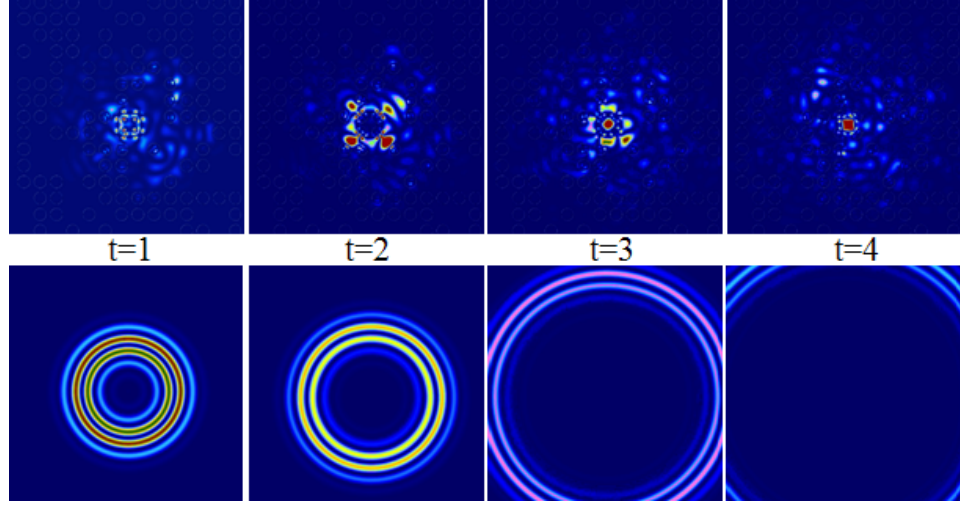


Figure 4.1: An electromagnetic dipole pulse evolving through (top row) a random nanostructure array and (bottom row) a homogeneous medium.

effects, as depicted in Figure 4.1. As we can see, by the time the pulse in homo medium has completely escaped, we still have high intensity fields close to the source origin, demonstrating the localization and slowed diffusion effects we hope to rigorously detail. With these simulations we seek to develop a confidence and understanding such that we can make educated decisions regarding the devices to be fabricated for experimentation.

4.1.1 Finite Difference Time Domain Simulations

The Finite Difference Time Domain method is a numerical method for solving Maxwell's equations in an arbitrarily complex geometry. It is a rigorous full-vector method that can provide both time domain and frequency domain information. The method is both discrete in time and space, and thus, the fields and media are described on what has been termed a 'Yee Cell'. These Yee cells form a discrete mesh over which the numerical method can take quantized steps in both time and space. The discrete time step and mesh cell size are related through the speed of light, c . Importantly, at the $\lim_{meshcellsize \rightarrow 0}$ the numerical method provides an exact solution to Maxwell's equa-

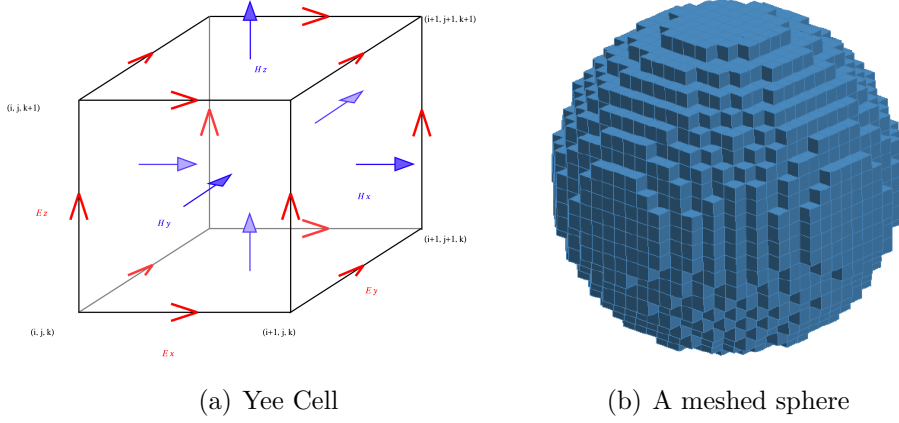


Figure 4.2: FDTD Geometry Representation

tions. Simulations are often populated with customizable sources and the propagation of that source through the defined media is calculated over the time interval specified. Time domain information can be captured at any spatial point and frequency domain information can be found using the Fourier transform of the time domain field data at that same point. This is useful because it allows many frequencies to be examined from a single simulation. This method is the backbone for the following electromagnetic simulations (Taflove, 1980).

4.2 One-Dimensional Systems

Our study now focuses primarily on the Rudin-shapiro and periodic structures. The Rudin-Shapiro system has been chosen because of the strong subdiffusive effects observed in the random walk experiments and the periodic system is used as a baseline given its ballistic transport properties. The wave transport behavior is studied through these systems with the goal of identifying slowed diffusive behavior.

One-dimensional systems are realized through waveguide structures. Due to the fact that they have a width dimension, we loosely refer to them as 'pseudo-1D'. Aperiodic structures are realized through having breaks in the waveguide material. These breaks

can be filled with either a material of varying index or with air - both cases are explored. This process creates a waveguide consisting of dielectric slabs ordered according to the aperiodic sequence. The thickness of each waveguide section is determined by the following relationship:

$$n_1 d_1 = n_2 d_2 = \frac{\lambda}{4}, \quad (4.1)$$

where the subscripts 1 and 2 denote the alternating materials of the waveguide. During this work, simulations were explored in which the right-hand side of equation equal to $\frac{2\lambda}{4}$, $\frac{3\lambda}{4}$, λ . However, such waveguides produced less desirable Fourier spectra (less supportive of localized modes and anomalous transport) and for this reason were not further investigated.

For all simulations, PML boundary conditions are used and typically use 24 layers (too much fewer and reflections from the boundary become intolerable). A depiction of the PML boundaries, as well as the aperiodic waveguide structure, is shown in Figure 4.3.

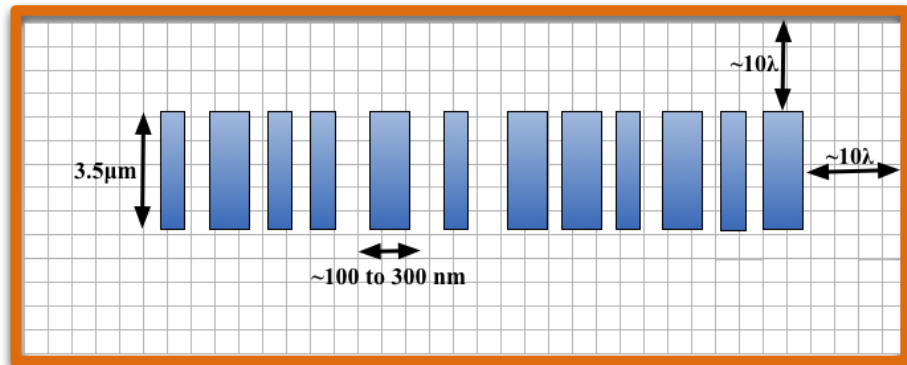


Figure 4.3: A depiction of an aperiodic waveguide structure setup in an FDTD environment. Note, the orange PML layers are kept at roughly 10 times the wavelength of the incident light from any structure to avoid disruptive reflections. Yee cell mesh sizes are exaggerated to show detail.

We begin this exploration by first quantifying the transmission spectra of each wave-

uide. Through calculating the transmission spectra of the systems in question, we are able to quantify the wavelengths which are supported by these waveguides. Other critical information, such as the band gap of the waveguides and the bandwidth of the transmitted modes will be found. The transmission spectra measurement is setup using a 2D simulation, though to comply with our 'pseudo-1D' intentions, the simulation is uniform along the y-axis. A light source for the simulation is created using the mode-source tool of the FDTD software. For the 1D waveguide case, this allows us to match the mode of the source to the mode of the waveguide. The built in Lumerical mode solver is used and the lowest order mode is sent. A spectrally broad pulse used, in this case, defined by a bandwidth from $1.3\mu m$ to $1.8\mu m$. The resulting pulse has a temporal length of $8.6fs$. A single frequency monitor at the output plane of the 1D waveguide measures the transmitted field. This data is then used in conjunction with the transmission function to normalize the collected output data to the incident mode. This function is defined as:

$$T(f) = \frac{\frac{1}{2} \int real(P(f)^{Monitor}) \cdot dS}{sourcepower} \quad (4.2)$$

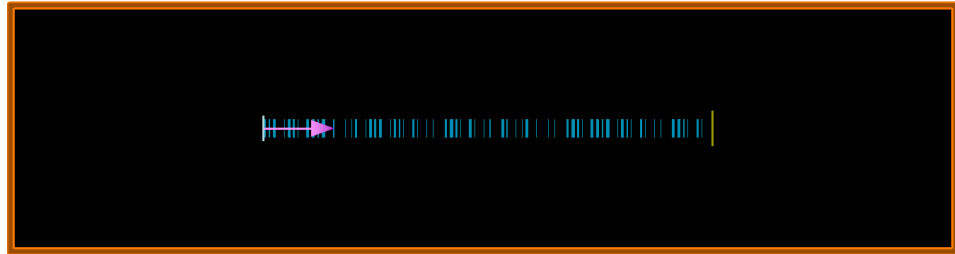


Figure 4.4: Sample FDTD transmission setup. Note yellow frequency monitor to the right of the structure and the pink source indicator at the lefthand side. The orange border is the PML layers.

These simulations have been run over a wide range of both waveguide materials and the waveguide length. The material will give insight into how different refractive indexes

influence the transport properties while the varying lengths will allow for the calculation of the scaling dynamics of these systems.

Using these transmission spectra we can determine which structures are the best candidates to proceed with the transport measurements. The quality factor that we use to determine which structures are suitable is related to the Q-factor of the peaks within the transmission spectra (narrower peaks lead to greater localization/trapping effects) and peak separation (we want to be able to select a single transmission mode without overlap from other modes). The spectra that provide the best results are provided in Table 4.1. The transmission spectra of these systems are given in Figure 4.5.

Structure	Material 1	Material 2
Periodic	SiN (2.1)	Doped SiN (2.3)
Rudin-Shapiro	Si (3.5)	Doped Quartz (1.5)
Rudin-Shapiro	SiN (2.1)	Air (1)
Rudin-Shapiro	SiN (2.1)	Doped SiN (2.3)

Table 4.1: Structures explored as decided due to desirable transmission spectra features.

It should be noted that the transmission spectra of the periodic SiN and doped SiN structure demonstrates a clear bandgap and resonances due to Fabry-Perot reflections. This is nearly identical to what is described by the theory of a one-dimensional Bragg grating despite the fact that this analysis is performed on a two-dimensional simulation. This result provides evidence that our approximation of a one-dimensional system is appropriate.

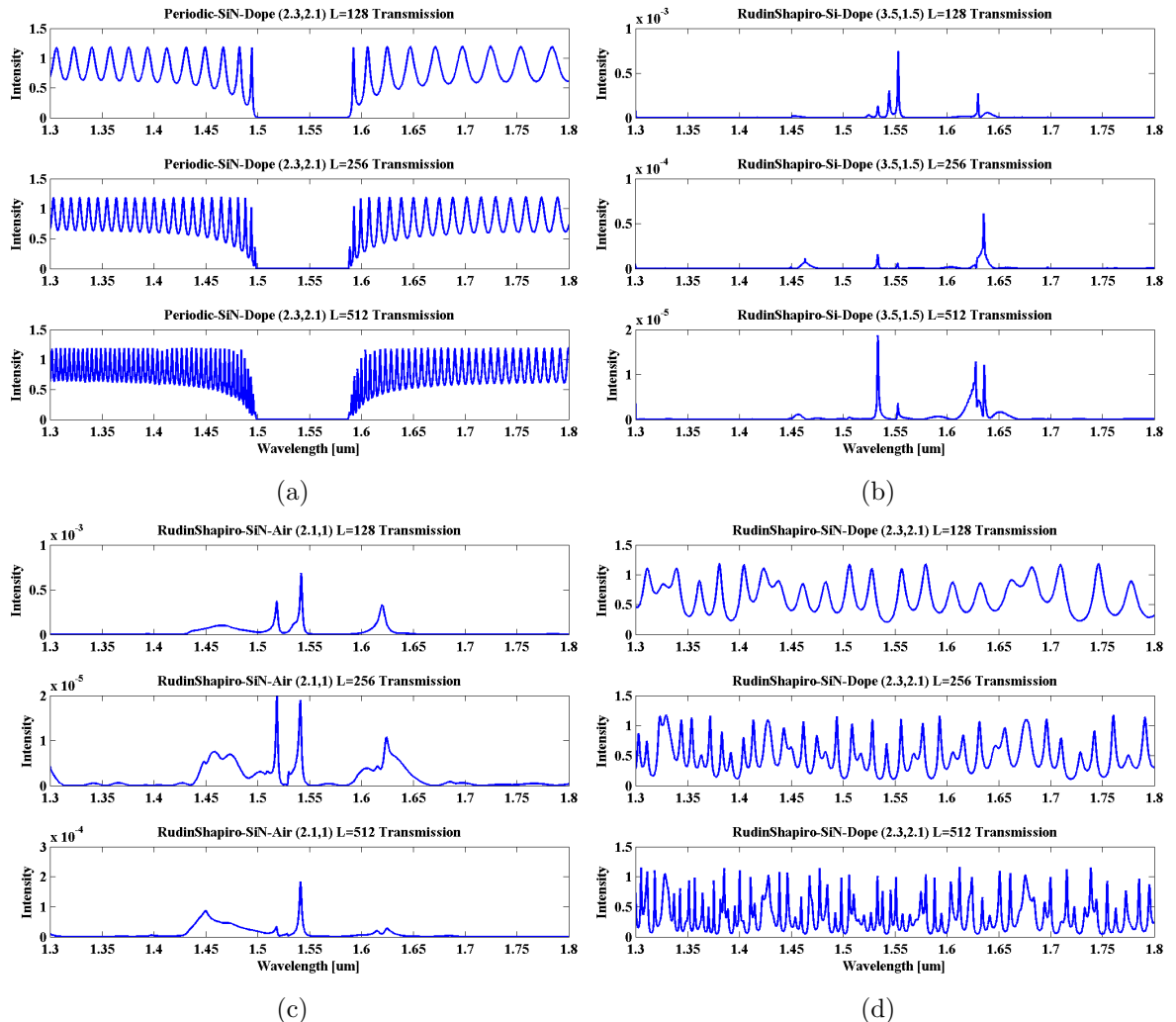


Figure 4.5: Transmission Spectra for three different systems at three different lengths each.

4.2.1 Diffusion Constant Analysis

The transport of a light pulse through a system, when the transport is assumed to be diffusive, is well described by understanding the mean squared displacement of the pulse energy. This displacement is typically given by, $\langle r^2(t) \rangle \sim Dt^\beta$. While the β exponent determines the regime of transport (normal, superdiffusive, or subdiffusive), the diffusion constant, D , is also of interest when characterizing the propagation through a system.

To collect such information, the same data layout as the previous transmission measurement is used, however, we are now concerned with the time dynamics of the system, so a field intensity monitor is used rather than a frequency monitor. We use a realistic source pulse with a total temporal length of 150fs and center the frequency of this pulse around those wavelengths that give rise to the highest transmission efficiency as shown in the spectra of Figure 4.5. The frequencies and structures that are chosen for this analysis are summarized in Table 4.2. The intensity of the electric field is measured at the output facet of the system and the simulation is run for 6000fs to ensure the pulse has had sufficient time to travel through the structure.

		Wavelength			
	Length	λ_1	λ_2	λ_3	λ_4
Periodic (SiN and Doped SiN)	128	1431nm	1592nm	1754nm	-
	256	1473nm	1599nm	1744nm	-
	512	1459nm	1604nm	1739nm	-
Rudin-Shapiro (Si and Doped Quartz)	128	1533nm	1545nm	1553nm	1630nm
	256	1463nm	1534nm	1552nm	1635nm
	512	1533nm	1627nm	1636nm	-
Rudin-Shapiro (SiN and Air)	128	1450nm	1518nm	1542nm	1620nm
	256	1450nm	1518nm	1542nm	1620nm
	512	1450nm	1518nm	1542nm	1620nm

Table 4.2: Frequencies examined in the pulse decay analysis

We first take a qualitative look at the influence of frequency, scale, and structure on the resulting output intensity. Figure 4.6 shows the electric field intensity at the output

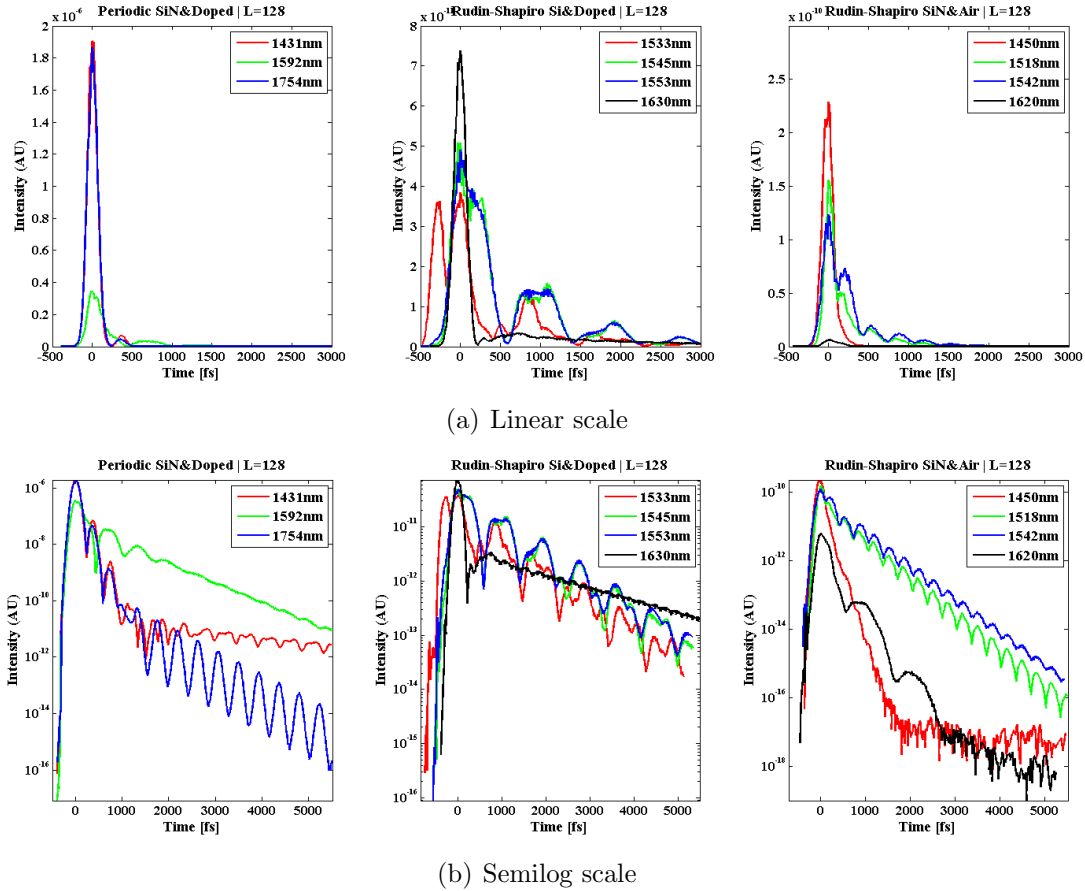


Figure 4.6: Intensity versus time as a function of both structure and frequency, measured at the output facet of the structure.

of the structure as a function of frequency (overlaid on a single plot) and structure (subsequent plots) on both a linear scale and semilog-y scale. The linear scale shows large intensity variations amongst frequencies for each structure, while the semilog-y scale shows stretched decay properties of the intensity for varying wavelengths. The pulse shape is also changed as you vary both structure and frequency, as can be best seen on the linear scales. Two different types of pulse reshaping appear: pulse breaking - as seen in the Rudin-Shapiro Si structure at 1553nm, and pulse stretching, as shown by the 1542nm data of the Rudin-Shapiro SiN structure. While both are interesting phenomenon, pulse stretching is the mechanism that more closely relates to anomalous

diffusion, whereas pulse-breaking is more indicative of Anderson localization of light energy.

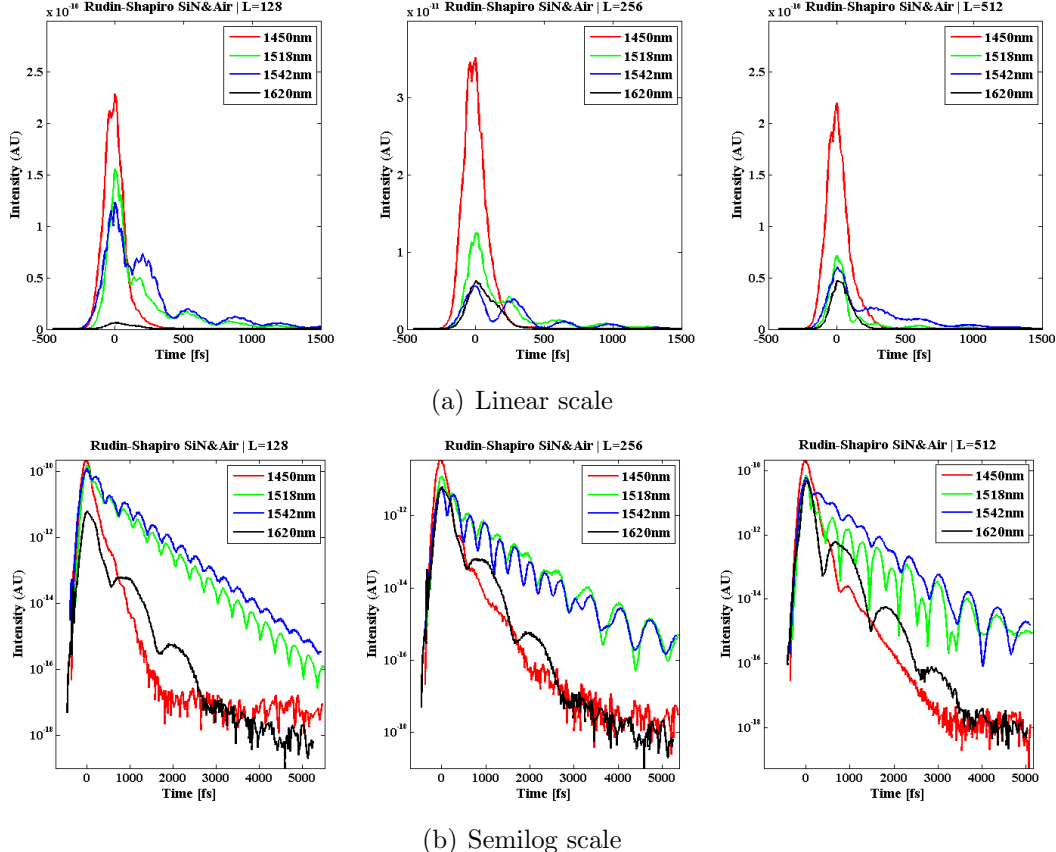


Figure 4.7: Intensity versus time as a function of both scale and frequency, measured at the output facet of the structure.

The dependence on scale and frequency is also explored. The Rudin-Shapiro SiN structure is chosen and kept constant while the length of this structure varies over $L = 128$, $L = 256$, and $L = 512$. This data is plotted in Figure 4.7 and both linear and semilog-y scales are again provided. In the linear scale, we can see that the intensity relationship stays qualitatively similar (i.e. 1454nm is always strongest, followed by 1518nm, etc), yet there are some changes as the length is scaled. More importantly, we can see that the pulse shape changes (especially at 1542nm) as the length of the system

grows. Focusing now on the semilog-y scale, we can see again a somewhat consistent relation between frequencies (1450 and 1518nm always decay more slowly than 1542 and 1620nm) along different lengths, but this relationship does change. Notably, the lower frequencies develop stronger oscillations as the scale increases.

While these plots give a qualitative feel, we again select three specific frequencies to analyze more rigorously. The qualitative approach is useful for gaining a rough understanding of the system properties, but a more thorough quantitative approach is also required. One frequency is chosen for each structure and the length is set to $L = 512$ to ensure that the mode source has fully emitted the pulse before any electric field reaches the end facet. The frequencies are again chosen to be the ones with the highest transmission efficiency and are detailed in Table 4.3.

Structure	Structure Length	Wavelength
Periodic SiN and Doped SiN	512	1739nm
Rudin-Shapiro Si and Doped Quartz	512	1533nm
Rudin-Shapiro SiN and Air	512	1542nm

Table 4.3: Frequencies explored for pulse decay measurements.

The data for each of these frequencies is both time and intensity normalized. The time normalization adjusts the time scale for each set of data such that the point at which the pulse maximum reaches the end of the structure is regarded as $t = 0$. This allows us to overlay each set of data for comparison regardless of the fact that the light does not reach the end of each structure synchronously. Intensity normalization scales the maximum intensity value for each data set to unity. Since we are concerned with the decay characteristics (rather than the specific intensity value), this has no effect on the resulting analysis and allows the three data sets to be overlaid on a single set of axes. The data is given on a loglog scale so that the slope of each curve represents the diffusion constant. Exponential curve fits of the form $y = y_0 + Ae^{Bx}$ are calculated and

overlaid on the same plot, as shown in Figure 4·8. The exponents calculated from curve

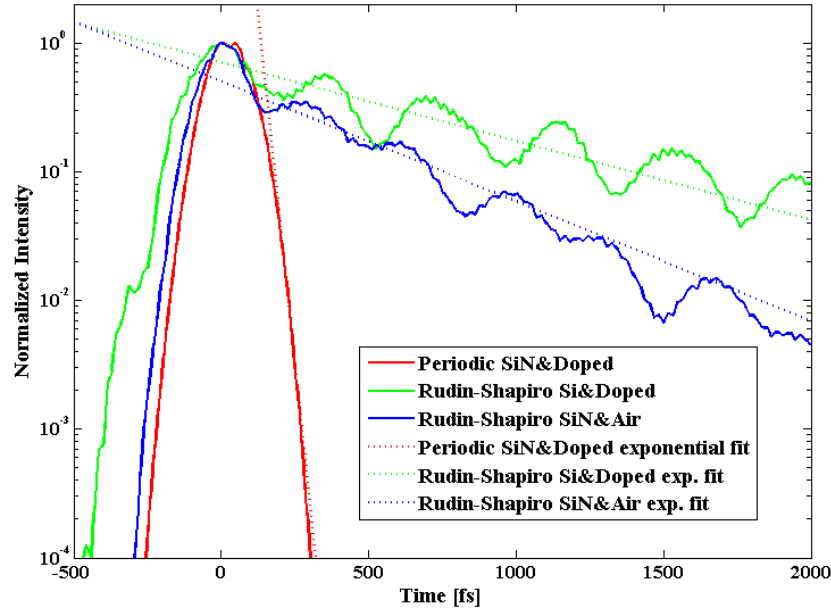


Figure 4·8: Intensity versus time for the three structures of interest. Each data set is fit by an exponential curve, yielding exponents of -0.0499, -0.00141, and -0.00214 for the Periodic, Rudin-Shapiro Si, and Rudin-Shapiro SiN structures, respectively.

fitting are summarized in Table 4·4. The results are also normalized with respect to the periodic structure diffusion constant. These results show clearly that the Rudin-Shapiro

Structure	Calculated constant	Normalized constant
Periodic SiN and Doped SiN	-0.0499	1
Rudin-Shapiro Si and Doped Quartz	-0.00141	0.0283
Rudin-Shapiro SiN and Air	-0.00214	0.0429

Table 4·4: Diffusion constants calculated from the exponential curve fit of the pulse decay data.

structures give rise to a smaller diffusion constant, and thus a reduced transport speed. This however, is tangential to the main goal of demonstrating subdiffusive behavior in

aperiodic systems. To explore the phenomenon of subdiffusion more directly, we explore the diffusion exponent yielded by these systems.

4.2.2 Diffusion Exponent Analysis

To probe the diffusion exponent of these systems we seek to measure the mean squared displacement of a light pulse as it propagates through each structure. We begin this measurement by sending an ultra-short pulse of light ($8.6fs$) at one edge of the waveguide. To track the pulse as it travels, one can not simply track the intensity of the field, due to the many facets the pulse will encounter, there will be reflections, localization effects, and interference effects. For these reasons one must track the energy density of the pulse through the system. Through tracking the energy density, we will be able to calculate the mean square displacement, or synonymously the diffusion length, of the pulse over time. We use the following equation to achieve this:

$$L_d^2(t) = \int dr u(r, t) |r - r_0|^2. \quad (4.3)$$

Here, L_d is the diffusion length, r_0 is the position of the source, and $u(r, t)$ is the energy density with respect to the total supplied energy at a given time t , given by:

$$u(r, t) = \frac{1}{2}(E \cdot D + B \cdot H) \quad (4.4)$$

In order to achieve this, we use an FDTD setup with two monitors: a two-dimensional electric field monitor surrounding the waveguide and a one-dimensional refractive index monitor to track the changes in the dielectric constant amongst the slabs of material. A depiction of this setup is shown in Figure 4.9. Because our system is uniform in y , we integrate the resulting 2D field intensity in the y direction, yielding a 1D horizontal line of electric field values that has been calculated for every time position in the simulation. This data is sufficient then to calculate the diffusion length of our system versus time.

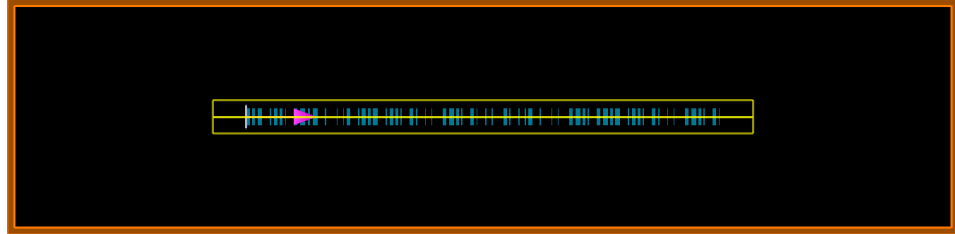


Figure 4.9: Sample FDTD diffusion length measurement setup. Note the 2D field monitor surrounding the structure and the 1D index monitor through the center of the structure.

For this analysis, we focus on only two structure types: the periodic SiN & doped SiN system and the Rudin-Shapiro SiN & doped SiN system. Here, we keep the structure materials the same so that any conclusions can be made in regards to the difference in disorder (structure) rather than material properties. The frequencies used for each structure at each length are displayed in Table 4.5. The spectra of these structures are again given in Figure 4.5.

		Wavelength		
		Length	λ_1	λ_2
			128	256
Periodic (SiN and Doped SiN)	128	1431nm	1592nm	1754nm
	256	1473nm	1599nm	1744nm
	512	1459nm	1604nm	1739nm
Rudin-Shapiro (SiN and Doped SiN)	128	1424nm	1528nm	1682nm
	256	1424nm	1494nm	1675nm
	512	1424nm	1498nm	1675nm

Table 4.5: Frequencies examined in the energy transport analysis

The results data has four distinctive regimes, as demonstrated in Figure 4.10. Note that the y-axis, representing the displacement, has been normalized to unity. This implies that each structure has been normalized to a length of 1, and the data now represents the percentage of structure length that has been traversed. Thus, the time at which the curve reaches a displacement of 1 represents the time at which the pulse

first reaches the end of the structure. After this point, the pulse reflects off of the PML simulation boundary and the energy density begins to travel in the reverse direction. Note that this is really just a formality as the lengths of each structure were identical ($L = 512$), so the following analysis holds without normalization as well. To calculate

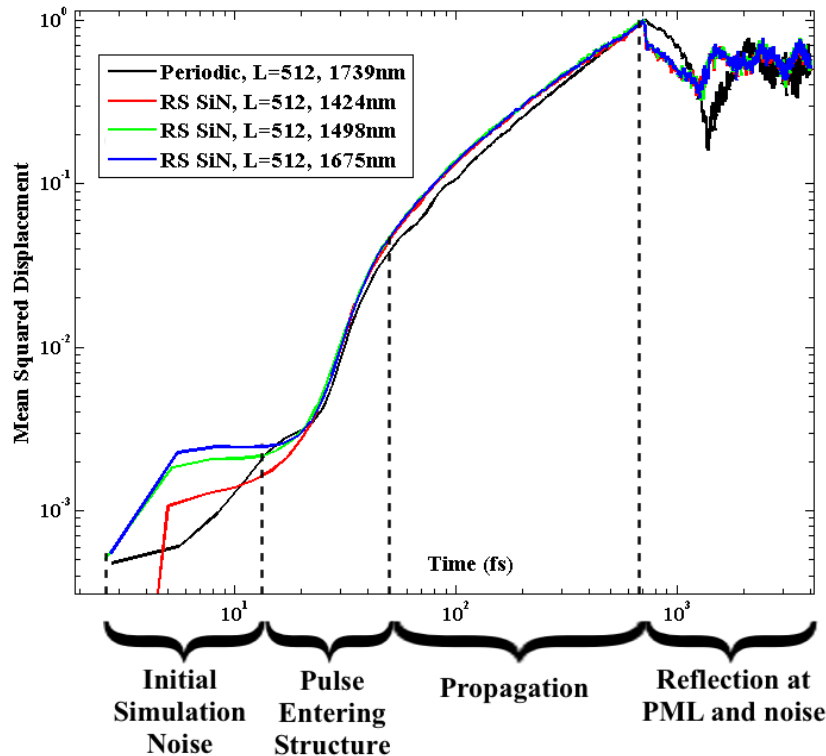


Figure 4.10: Regimes of the energy density displacement data.

the mean square displacement, we are interested in the transport regime of this data, and the rest is disregarded as extraneous information. Returning to the mean squared displacement equation, $\langle r^2(t) \rangle \sim Dt^\beta$, we are interested in the β exponent that determines the transport regime each pulse is operating in. To achieve this, a power law curve of the form $y = y_0 + Ax^B$ is fit to the data. The results of this, shown in both linear and log-log scale in Figure 4.11, are detailed in Table 4.6. For these simulations,

all structure lengths are held constant at $L = 512$ to standardize the results.

Structure	Wavelength	Fit equation	β
Periodic SiN and Doped SiN	1739nm	$\langle r^2(t) \rangle \sim -0.036 + 0.0014t^{1.003}$	1.003
	1424nm	$\langle r^2(t) \rangle \sim -0.084 + 0.0055t^{0.799}$	0.799
	1498nm	$\langle r^2(t) \rangle \sim -0.088 + 0.0055t^{0.805}$	0.805
	1675nm	$\langle r^2(t) \rangle \sim -0.097 + 0.0064t^{0.780}$	0.780

Table 4.6: Mean square displacement data power law fitting results. The length is held at $L = 512$ for all structures.

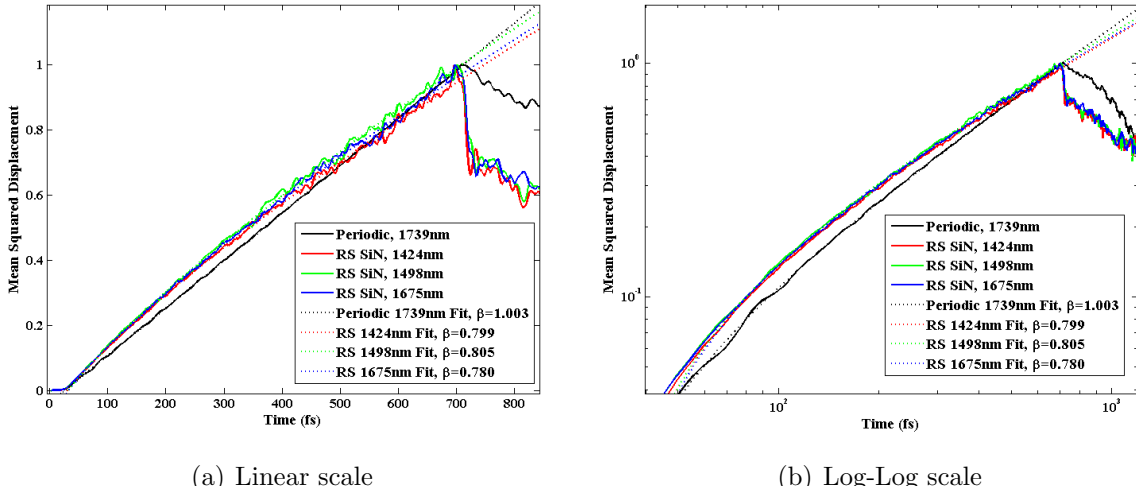


Figure 4.11: Mean Squared Displacement versus Time in both linear and log-log scale. The power law curve fits are overlaid with dotted lines.

This data thus shows clear subdiffusion of electromagnetic energy through the Rudin-Shapiro structures. Characterized by a $\beta < 1$ (in this case ≈ 0.80), the subdiffusive behavior that was shown in the one- and two-dimensional random walks is verified in an electromagnetic domain. If we plot just the power law fits and extrapolate the time axis to 5000 fs , the subdiffusive effect can be more easily appreciated (Figure 4.12).

This then represents the first verification of optical subdiffusion in deterministic media. To further explore this phenomenon, the effect of the scaling length on the diffusion exponent is explored. Now, rather than a fixed length of $L = 512$, the length is

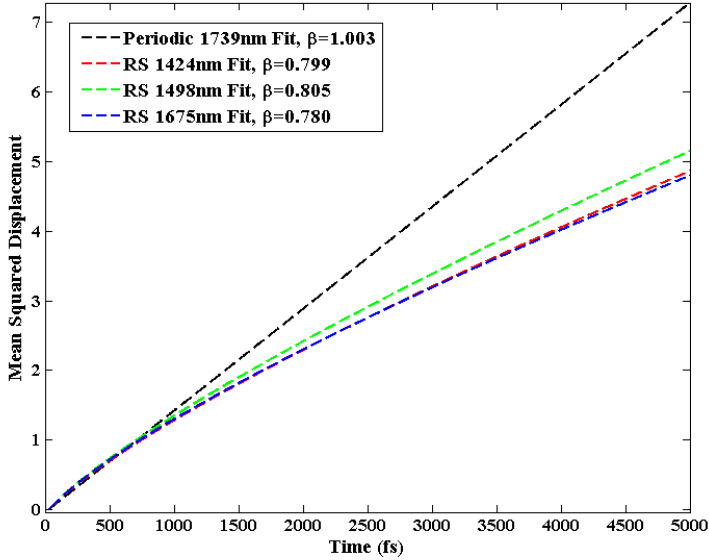


Figure 4.12: Mean Square Displacement versus Time power law fits.

varied between $L = 128$, $L = 256$, and $L = 512$ and the same energy density propagation analysis is conducted. The same structures and FDTD simulation setup are used and the wavelength explored at each structure length is held roughly constant ($\pm 10\text{nm}$). We vary these length scales over both the periodic and Rudin-Shapiro structures, which yields the data shown in Figure 4.13.

Figure 4.13 shows that both the Rudin-Shapiro and periodic structures lead to similar shifts in the mean squared displacement curves. As the structure grows, the curves shift downwards and the peak shifts to the right, implying that the pulse arrives at the end of the structure at a later time. This is intuitive, as we expect any traveling object to require more time to travel a longer distance. However, fitting power law curves to each of these data sets (Figure 4.14) reveals a more complex transport mechanism than first assumed through intuition. While the periodic structures remain ballistic at all length scales (i.e. $\beta = 1$), the Rudin-Shapiro structure demonstrates an increase in the

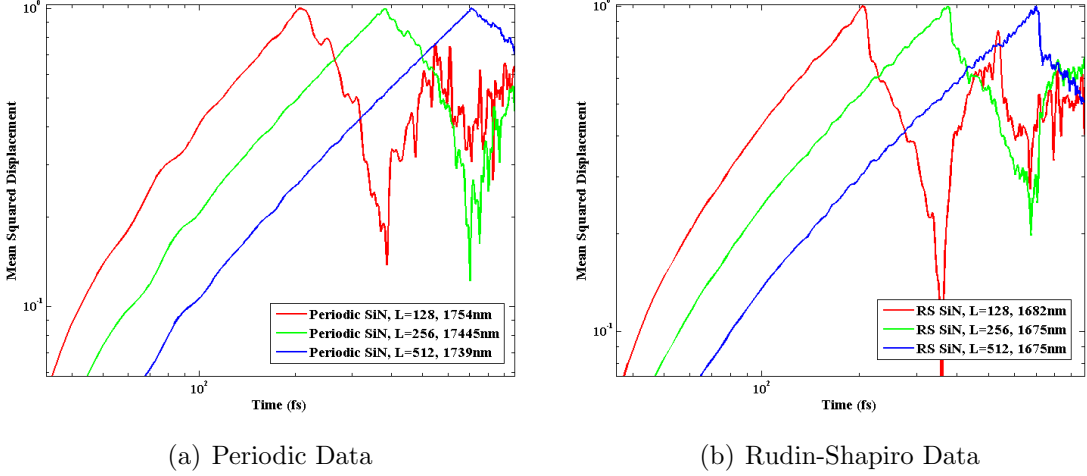


Figure 4.13: Mean Square Displacement vs. Time as a function of the structure length.

subdiffusivity of the structure as the length increases. The results of the power law fits

Structure	Length	Fit equation	β
Periodic (SiN and Doped SiN)	128	$\langle r^2(t) \rangle \sim -0.107 + 0.0038t^{1.066}$	1.066
	256	$\langle r^2(t) \rangle \sim -0.120 + 0.0071t^{1.002}$	1.002
	512	$\langle r^2(t) \rangle \sim -0.097 + 0.0064t^{1.003}$	1.003
Rudin-Shapiro (SiN and Doped SiN)	128	$\langle r^2(t) \rangle \sim -0.174 + 0.0091t^{0.912}$	0.912
	256	$\langle r^2(t) \rangle \sim -0.120 + 0.0071t^{0.852}$	0.852
	512	$\langle r^2(t) \rangle \sim -0.097 + 0.0064t^{0.780}$	0.780

Table 4.7: Mean square displacement as a function of structure length power law fitting results.

are summarized in Table 4.7. The mechanism for decreasing the diffusion exponent can be understood through scattering and localization arguments. The longer the aperiodic structure, the more 'traps' the pulse will encounter. Each trap serves to localize the pulse for a brief period of time, and importantly, the localization effects are not linear. Each localization and back reflection influences, and is in turn influenced, by previous reflections and localization events. This thus creates a cumulative effect over the length of the structure that grows as the length of the structure increases. This scaling prop-

erty thus suggests the ability to actively tune the subdiffusion exponent through the fabrication of deterministic aperiodic structures.

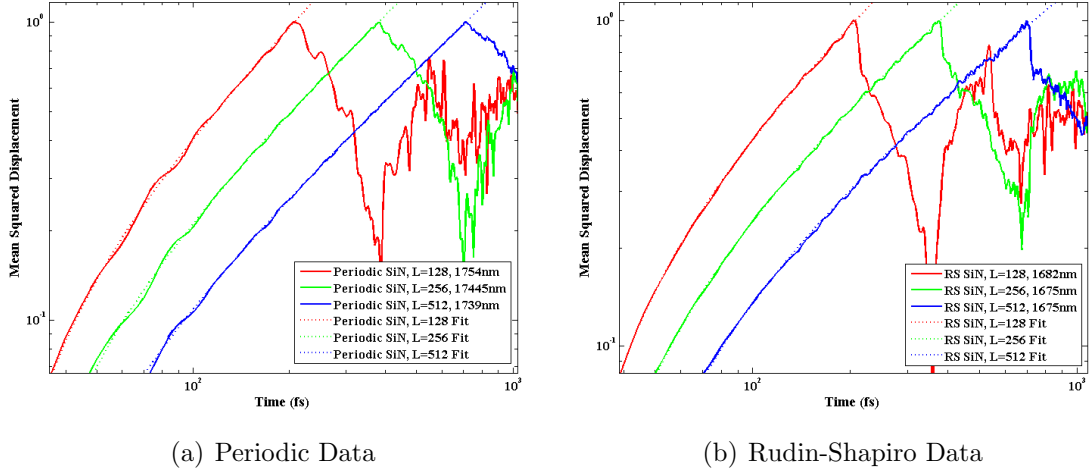


Figure 4.14: Mean Square Displacement vs. Time as a function of the structure length. Power law fits are overlaid.

4.2.3 Influence of scattering strength and localization length

The scattering strength and localization length have been shown to have a strong influence on the transport of aperiodic waveguide systems. To support propagation through consecutive dielectric slabs of varying index, the index contrast must support sufficient confinement. Once propagation has been established there is an optimized domain that gives rise to subdiffusion. If the scattering strength is too weak, no effect will be seen as the localization phenomena will be minimal. Conversely, if the scattering strength is too strong, light will be scattered out of the plane of the waveguide, thus leading to a loss of confinement. Similarly, the localization length, which is given by l_c , can be categorized into three domains determined by: (a) $l_c \ll \lambda$, (b) $l_c \approx \lambda$, and (c) $l_c \gg \lambda$. For subdiffusion, the regime of interest is when $l_c \gg \lambda$. In this scenario, we have weak scattering of the type that leads to diffusive transport of light.

The scattering length can be found using a scaling analysis in which the transmission of a given system is measured over many system lengths. When light propagates through a one-dimensional multi-layer dielectric system, the localization length is defined by:

$$l_c = \frac{-L}{\langle \ln(T) \rangle}, \quad (4.5)$$

where L is the length of the system and T is the transmission. The transmission is to be averaged over many systems samples which are of equal length and disorder. This is straight forward for a random system, but becomes slightly trickier to quantify for deterministic aperiodic sequences. Such analysis is typically demonstrated by plotting the reciprocal ensemble averaged transmission $1/T$ versus the system length L on a semilog scale, as depicted in Figure 4.15. The slope of the resulting curve represents the localization length of the given system (Daozhong et al., 1994) (Asatryan et al., 1996).

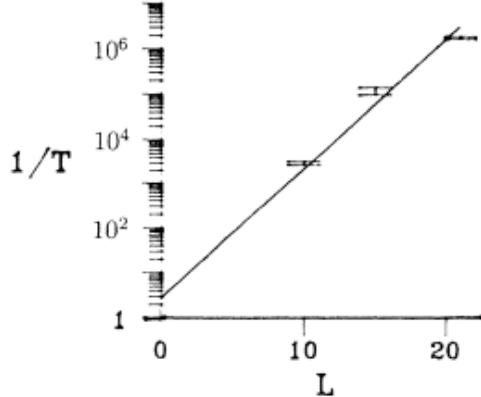


Figure 4.15: Reciprocal transmission versus the system length. The slope of this data yields the localization length, l_c (Daozhong et al., 1994).

The importance of the scattering regime of each structure is seen to be directly relevant to the transport properties of Rudin-Shapiro systems. As previously noted, there are two distinct domains encountered in the design of these systems: (a) the scattering

and localization effects are too strong and do not support propagation, and (b) the scattering is appropriate for subdiffusive transport. In the case of the Si and Air Rudin-Shapiro structure, the index contrast (3.5 and 1) is too great and the localization effect too strong to support transport. This leads to a confined mode that oscillates within the first two facets of the dielectric multilayer structure (Figure 4·16). Alternatively, the SiN and Doped SiN Rudin-Shapiro structure has an appropriate index contrast (2.1 and 2.3) and thus leads to sufficiently weak scattering such that transport is possible (Figure 4·17).

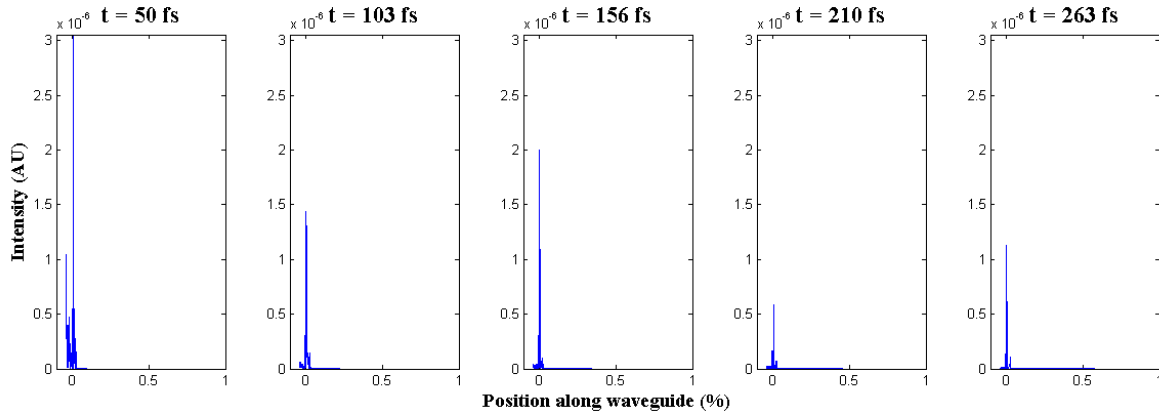


Figure 4·16: Pulse propagation in the Rudin-Shapiro Si and Air structure. The strong scattering leads to a localized mode that does no propagate with time.

Interestingly, the Rudin-Shapiro structure that does propagate energy exhibits a long tail of fluctuating energy fields in the wake of the wavefront. This is in contrast to the periodic propagating structure which does not demonstrate a long tail (Figure 4·18). This long tail is an established phenomenon that is most frequently witnessed in regards to acoustic waves and has previously been described for one-dimensional random media (Figure 4·19). Thus, the presence of the same phenomenon here demonstrates the power of aperiodic systems to mimic the properties of random systems deterministically. The process is identical for both aperiodic photonic systems and random acoustic systems.

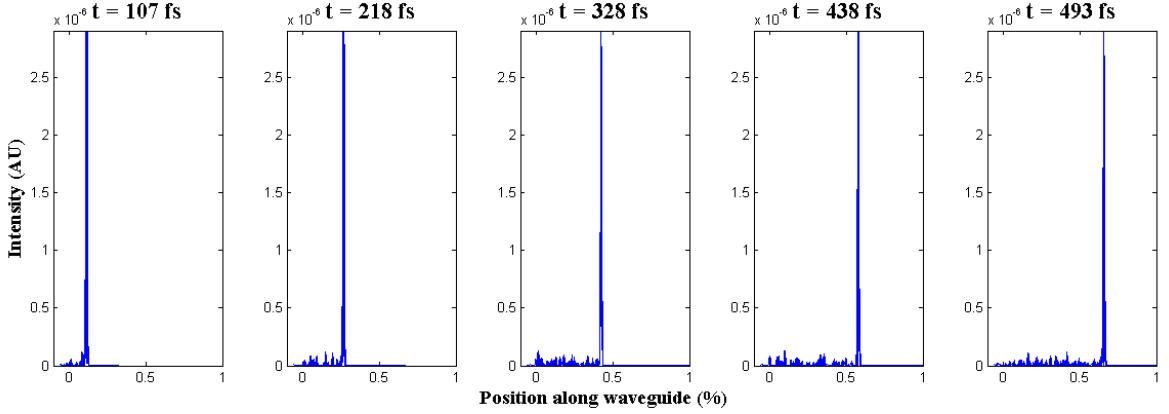


Figure 4.17: Pulse propagation in the Rudin-Shapiro SiN and Doped SiN structure. The index contrast and scattering strength are engineered such that propagation of the light pulse is allowed.

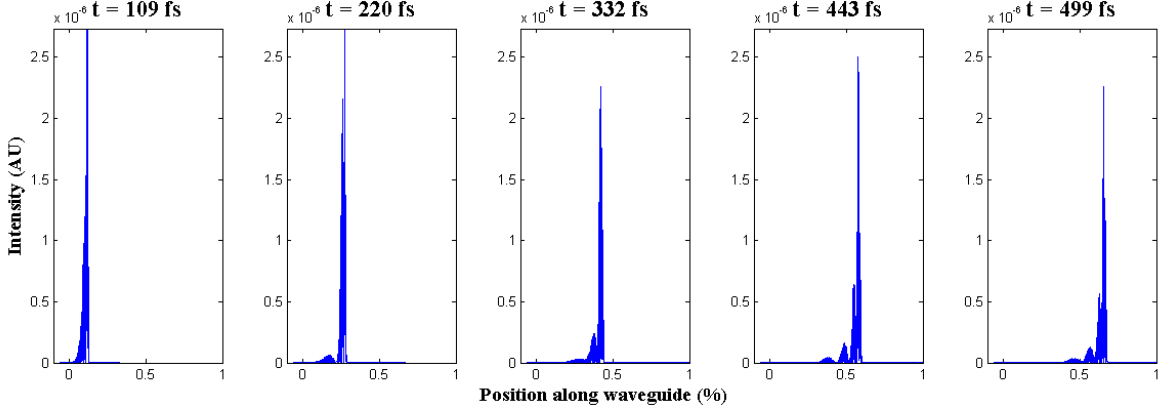


Figure 4.18: Pulse propagation in the Periodic SiN and Doped SiN structure.

A wave pulse is injected into one side of a disordered one-dimensional system and the transmitted energy is measured at the opposite facet of the system. The measured pulse is typically a smeared version of the incident pulse that is followed by a noisy, incoherent tail of energy fluctuations, or coda. Interestingly, the front of the transmitted pulse is coherent and is creating through a deterministic process given by the convolution of the incident pulse with a stochastic kernel that is dependent upon the disorder of the structure (Fouque et al., 2007). Figure 4.19 depicts the transmission of an acoustic wave through a random one-dimensional medium. The long tail of energy fluctuations

following the initial pulse are similar to those seen in the propagation of photons through aperiodic dielectric structures, as shown in Figure 4.17.

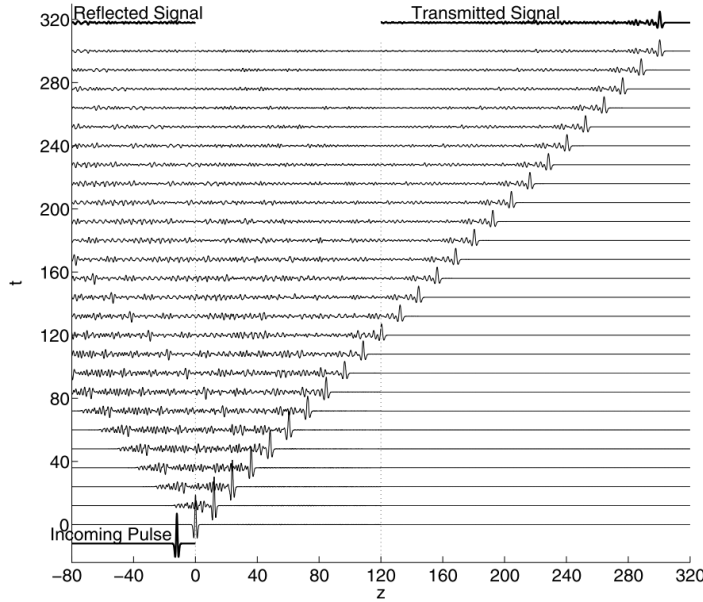


Figure 4.19: Acoustic pulse propagation through a random one-dimensional medium (Fouque et al., 2007).

4.3 Two-Dimensional Systems

Two dimensional aperiodic systems can also be evaluated using the same techniques as outlined for the one-dimensional systems. Due to the fact that the 1D systems are in fact pseudo-1D and are run in a 2D environment, no additional changes are required. The methods for calculating the transmission, energy density transport, and pulse decay are identical.

The physical structure of the system, however, of course is different. Rather than slabs of material with uniformity along the vertical direction, either spheres or columns populate the environment according to some aperiodic sequence. A sample FDTD setup for such a scenario is shown if Figure 4.20.

Such simulations and experiments have been carried out by Inose et al. for random

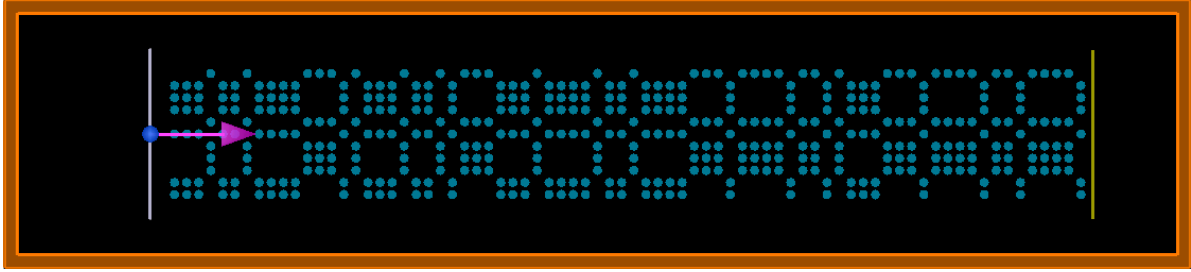


Figure 4.20: Sample CAD layout of a two-dimensional Rudin-Shapiro structure.

systems. While the effort in their work is targeted towards identifying Anderson localization effects, rather than slowed diffusion, the same transport measurements are made. Disordered dielectric cylindrical columns are used rather than slabs of dielectric material, but similar FDTD calculations are made to find the diffusion length, and energy density transport (Inose et al., 2010).

Chapter 5

Device Design and Engineering

Using the data collected in the previous chapter's simulations, preliminary experiments on physical structures have begun. The simulation data has helped to narrow the focus to a select number of structures that have demonstrated the strong potential for anomalous diffusion phenomena.

5.1 Fabrication

Devices are fabricated using electron-beam lithography. This technique enables us to write at the 100nm scale that is required. The structures have been fabricated at Lawrence-Berkeley National Laboratory due to their world-class clean room and writing capabilities. Their technology allows us to write at this scale with a precision that would be unachievable in many university clean rooms. Sections are written as 3D rectangular slabs and we have initially written our devices at lengths of 128 terms (ABAAB...etc). Each slab section has a width of $2.5\mu m$ and a height of $2\mu m$. Solid waveguide sections are also written before and after the aperiodic sections to allow for easier experimental light coupling. The waveguides are then cleaved at the edge of the substrate such that the solid waveguide section meets the edge of the chip. This allows for light to be coupled more efficiently with less scattering at the surface of the device. Figure 5.1 shows scanning electron micrographs of the results aperiodic waveguides.

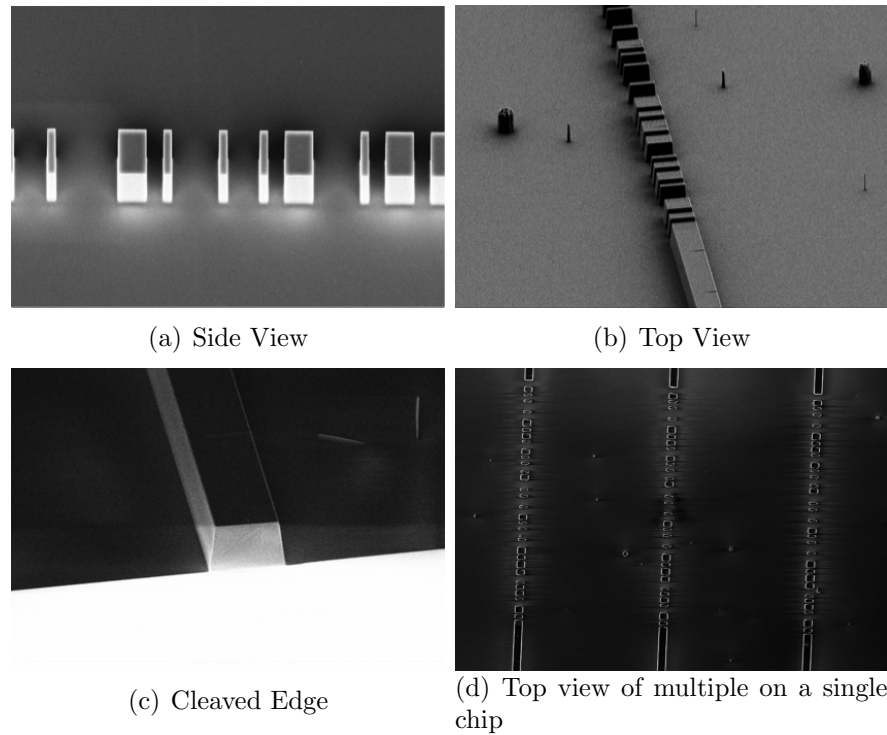


Figure 5·1: SEM Micrographs of aperiodic waveguides. (Courtesy of Nate Lawrence)

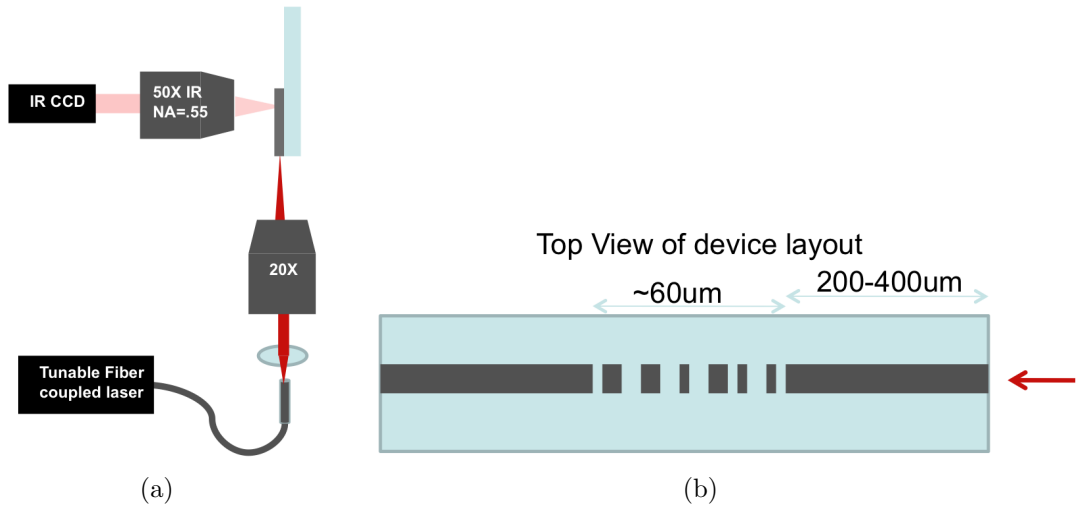
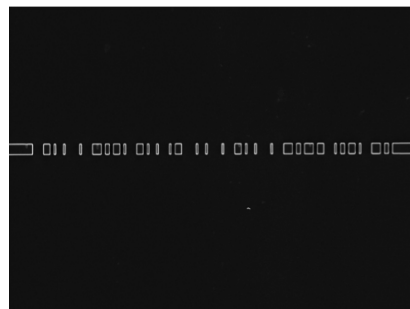


Figure 5.2: Experimental setup schematics (Courtesy of Nate Lawrence)

5.2 Experimental Methods

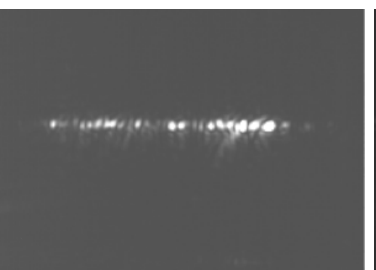
For the experimental setup we guide a tunable fiber-coupled laser into one facet of the aperiodic waveguide. The laser is tunable from 1520nm to 1610nm. Using an infrared CCD camera we view the scattering from the top of the devices. This will give us a measure of the losses from the structure and will allow us to estimate certain transport phenomena. A diagrammatic schematic of the setup can be seen in Figure 5.2. A tunable laser is used so that the waveguide can be excited at multiple wavelengths. The images captured using the IR CCD camera demonstrate the varying wavelengths influence on the transport of light through the system (Figure 5.3). The first thing to note is that the light is indeed traveling through this waveguide despite the jumps in refractive index along the direction of propagation. This suggests that our individual sections were properly fabricated such that light is coupled between them, rather than simply leaked at the facets. The intensity of light tails clearly varies as the wavelength is adjusted, implying that different frequencies are being more efficiently transported through the system. These results are of course very preliminary and serve more as a



(a) Unilluminated



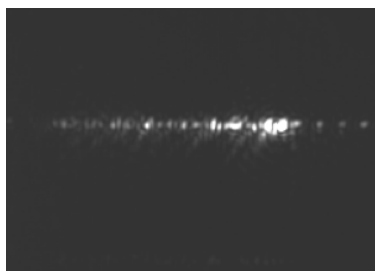
(b) 1520nm



(c) 1530nm



(d) 1540nm



(e) 1550nm



(f) 1560nm



(g) 1580nm

Figure 5.3: IR CCD images of out-of-plane light scattering from aperiodic waveguides (Courtesy of Nate Lawrence)

guide for how future experiments will be run rather than a basis for our first collection of anomalous subdiffusion data. Future efforts will be led most heavily by Nate Lawrence who has provided the bulk of the experimental work for this project.

Chapter 6

Conclusion

The goal of this thesis was to explore the influence of aperiodic disorder on the transport properties of nanostructures arrays and, more specifically, to identify the structures and parameters that lead to anomalous subdiffusion of light. While superdiffusion of light has been recently demonstrated (Barthelemy et al., 2008), the realm of subdiffusion has remained largely unexplored despite the exciting opportunities it offers for thin-film photovoltaics and optical sensing technologies.

The realm of photonic subdiffusion is explored through the use of both random walk simulations (Section 3.1) and electromagnetic Finite-Difference Time-Domain simulations (Section 4.1). The former provides a first-order approximation of the transport properties of aperiodic structures while the latter offers a more rigorous exploration of the wave-based phenomena of light.

The random walk simulations identified the Rudin-Shapiro structure as one which supports subdiffusion as well as Sinai logarithmic subdiffusion. The simulations also verified the conclusions made in the literature regarding the anomalous diffusion properties of random one-dimensional and two-dimensional systems. The electromagnetic numerical models substantiated the claim that the Rudin-Shapiro structure demonstrates subdiffusive properties. Furthermore, the scaling of the aperiodic Rudin-Shapiro structure was shown to facilitate the active tuning of the diffusion exponent, where longer structures lead to a decrease in the diffusion exponent, β . The propagation features of these subdiffusive transports have been shown to mimic those found in random

media and offer an opportunity to deterministically engineer disordered systems that display similar properties to random systems.

Importantly, this work outlines the structures to be tested during future experimental work and also identifies the process for determining whether any arbitrary structure supports subdiffusive transport. This numerical model makes it possible to consider a much wider range of structures than would be possible if each one had to be fabricated and characterized on an optical bench. The results shown here also act as a baseline for future experiments against which the collected data can be measured.

While the main goal of the thesis was to explore how aperiodic order and structure influenced the transport of photons, the work touched upon the influence of materials and, more importantly, material mismatch on transport behavior. Thus, the simulation environments and analysis are perfectly applicable for studying systems of various material composition rather than various disorder.

Appendix A

Source Code

Listing A.1: gen_Fib1D.m - Used to generate a one-dimensional Fibonacci sequence

```
1 function [output] = gen_Fib1D(length)
2
3
4     w = .5*(sqrt(5)+1);
5         array_fib = zeros(1,length);
6         for i=1:(length)
7             array_fib (i) = 1+floor(i/w)-floor((i+1)/w);
8         end
9         output = array_fib;
10
11 end
```

Listing A.1: gen_Fib1D.m - Used to generate a one-dimensional Fibonacci sequence

Listing A.2: gen_Fib2D.m - Used to generate a two-dimensional Fibonacci sequence

```
1 % Creates a 2D Fibonacci sequence which has a generation number which is
2 % equal to 'n'. By using Alternation Theory, that is in the X-Direction the
3 % propagation is normal, that is A goes to AB, and B goes to A. But then it
4 % starts alternating (Depending on number mudulation).
5
6 function [outvalue] = gen_Fib2D(sizes)
7
8     A=0;
9     B=1;
10
11    C=[A,B];
12    A=B;
```

```

13    B=C;
14
15    n=2;
16
17    while(length(B)<sizes)
18        C=[A,B];
19        A=B;
20        B=C;
21        n=n+1; % this serves as a reference counter only
22    end
23
24    A=C;
25    output = [];
26    N=length(A);
27    A1 = 1-A;
28
29    for i=1:N
30        if(A(i)==1)
31            output=[output,A'];
32        else
33            output=[output,A1'];
34        end
35    end
36    outvalue=output(1:sizes,1: sizes );
37 end

```

Listing A.2: gen_Fib2D.m - Used to generate a two-dimensional Fibonacci sequence

Listing A.3: gen_TM1D.m - Used to generate a one-dimensional Thue-Morse sequence

```

1 function [output] = gen_TM1D(sizes)
2
3     A = 1;
4     B = 0;
5
6     x = [A,B];
7
8     while (size(x,2) < sizes)
9         temp = zeros(1, 2*size(x,2));
10        for i = 1:size(x,2)
11            j = 2*i-1;

```

```

12      if x(i) == A
13          temp(j:j+1)= [A,B];
14      else
15          temp(j:j+1) = [B,A];
16      end
17  end
18  x = temp;
19  size(x,2);
20 end
21 output = x(1,1:sizes);
22 end

```

Listing A.3: gen_TM1D.m - Used to generate a one-dimensional Thue-Morse sequence

Listing A.4: gen_TM2D.m - Used to generate a two-dimensional Thue-Morse sequence

```

1 function [output] = gen_TM2D(size)
2
3     a=1;
4
5     while length(a)<size
6         b=1-a;
7         c=[a;b];
8         d=1-c;
9         a=[c';d'];
10        a=a';
11    end
12
13    output = a(1:size, 1:size);
14
15 end

```

Listing A.4: gen_TM2D.m - Used to generate a two-dimensional Thue-Morse sequence

Listing A.5: gen_RS1D.m - Used to generate a one-dimensional Rudin-Shapiro sequence

```

1 function [output] = gen_RS1D(sizes)
2
3     A = 1;

```

```

4   B = 0;
5   x = [A,B];
6
7   while (size(x,2) < sizes)
8       temp = zeros(1, 2*size(x,2));
9       for i = 1:2:size(x,2)
10          j = 2*i-1;
11          if x(i:i+1) == [A,A]
12              temp(j:j+3)= [A,A,A,B];
13          elseif x(i:i+1) == [A,B]
14              temp(j:j+3) = [A,A,B,A];
15          elseif x(i:i+1) == [B,A]
16              temp(j:j+3) = [B,B,A,B];
17          elseif x(i:i+1) == [B,B]
18              temp(j:j+3) = [B,B,B,A];
19      end
20
21      end
22      x = temp;
23      size(x,2);
24  end
25  output = x(1,1:sizes);
26 end

```

Listing A.5: gen_RS1D.m - Used to generate a one-dimensional Rudin-Shapiro sequence

Listing A.6: gen_RS2D.m - Used to generate a two-dimensional Rudin-Shapiro sequence

```

1 function [output] = gen_RS2D(Size)
2
3     TI = 1;
4     while 2^(TI+1) < Size
5         TI=TI+1;
6     end
7
8     output=[1,0;0,1];
9     N=size(output);
10
11    for j = 1:TI
12        buffer=[];
13        for i = 1:N(1,1)

```

```

14         b=RS(output(i,:));
15         buffer=[buffer;b];
16     end
17
18     buffer=buffer';
19     output=buffer;
20     N=size(output);
21     buffer=[];
22
23     for i=1:N(1,1)
24         b=RS(output(i,:));
25         buffer=[buffer;b];
26     end
27     output=buffer';
28 end
29
30
31
32
33
34
35
36 function [c]= RS(buffer)
37
38 % This function is used to create the RS sequence of an array of numbers buffer.
39 % There are some restrictions in the code, it assumed that
40 % the array is made of only 1s and 0s, also it assumes that the length of
41 % the array is a power of 2.
42
43 N=size(buffer);
44
45 n=0;
46
47 while (2^n<N(1,2))
48     n=n+1;
49 end
50
51 a=buffer;
52
53 for count2=1:n
54     c=[];
55     for count3=1:2:2^count2

```

```

56     if (a(count3)==1 && a(count3+1)==1)
57         b =[1,1,1,0];
58     elseif (a(count3)==1 && a(count3+1)==0)
59         b =[1,1,0,1];
60     elseif (a(count3)==0 && a(count3+1)==1)
61         b =[0,0,1,0];
62     else
63         b =[0,0,0,1];
64     end
65     c=[c,b];
66 end
67 end
68 end

```

Listing A.6: gen_RS2D.m - Used to generate a two-dimensional Rudin-Shapiro sequence

Listing A.7: gen_perc.m - Used to generate a two-dimensional percolation array of chosen percolation level p

```

1 function [ cluster ] = gen_perc(size, p_c)
2
3 %create square grid
4 %fill every point with a random number
5 %threshold random numbers to 0,1
6 %return cluster
7
8 cluster = rand(size);
9
10 for i = 1:size
11     for j = 1:size
12         if cluster(i,j) < (1-p_c)
13             cluster(i,j) = 0;
14         else
15             cluster(i,j) = 1;
16         end
17     end
18 end
19 end

```

Listing A.7: gen_perc.m - Used to generate a two-dimensional percolation array of chosen percolation level p

Listing A.8: gen-periodic.m - Used to generate a two-dimensional periodic sequence

```

1 function [output] = gen-periodic(size)
2
3     output = zeros(size);
4
5     for i=[1:size]
6         for j=[1:size]
7             output(i,j) = mod(i+j,2);
8         end
9     end
10 end

```

Listing A.8: gen-periodic.m - Used to generate a two-dimensional periodic sequence

Listing A.9: RW2D_pos.m - Used to generate the two-dimensional position-based random walk on all arrays of interest

```

1 function [history dev] = RW2D_pos (start_pos, a, data, radius, steps)
2
3     myloc = start_pos;
4     jumpcounter = 0;
5     history = zeros(steps,2);
6
7     for j = 1:steps
8         history(j,:) = myloc;
9         stepsize = a+randn;
10        theta = rand*2*pi; % choose random angle to jump at (in radians)
11        [dx dy] = pol2cart(theta,stepsize); %calculate change in x and y
12        newloc = myloc + [dx dy]; %find new location
13
14
15        if lineseg_circ_intersect_arr (myloc,newloc,data,radius) == 0
16            %If you don't collide with a particle , jump!
17            myloc = newloc;
18            jumpcounter = jumpcounter+1;
19        end
20
21    end
22    dev = abs(myloc(1)-start_pos(1))^2+abs(myloc(2)-start_pos(2))^2;
23

```

```

24 %%%%%%
25 %Optional Code for Plotting the Random walk
26 %    figure
27 %    for i = 1:length(data)
28 %        rectangle ('position',[data(i,1)-radius data(i,2)-radius 2*radius 2*radius],'
29 %        'curvature',[1,1], 'EdgeColor','k','FaceColor','k');
30 %    end
31 %    hold on
32 %    plot(history (:,1),history (:,2),'-','MarkerFaceColor', 'blue')
33 %    title (['Step Size = ',num2str(a)])
34 %    scatter(history (:,1),history (:,2),3, 'MarkerFaceColor', 'blue')
35 %%%%%%
36 end

```

Listing A.9: RW2D_pos.m - Used to generate the two-dimensional position-based random walk on all arrays of interest

Listing A.10: RW2D_8.m - Used to generate the two-dimensional grid-based random walk on all arrays of interest

```

1 %%%2D Random Walk
2 function [dev_fib, dev_RS, dev_TM, dev_random, dev_square, dev_periodic] = RW2D_8(
3     steps, size, a, location_start, lattice_fib, lattice_RS, lattice_TM, lattice_periodic,
4     lattice_square, lattice_random)
5
6
7     %%Directions
8     left = [-a,0];
9     upleft = [-a,a];
10    up = [0,a];
11    upright = [a,a];
12    right = [a,0];
13    downright =[a,-a];
14    down =[0,-a];
15    downleft= [-a,-a];
16    %%%
17
18    %Array variable to start to location history of the walker
19    history_fib = zeros(steps,2);
20    history_RS = zeros(steps,2);
21    history_TM = zeros(steps,2);
22    history_square = zeros(steps,2);
23    history_random = zeros(steps,2);

```

```

22 history_periodic = zeros(steps,2);
23
24 % Variables for the current location of the walker
25 location_fib = location_start;
26 location_RS = location_start;
27 location_TM = location_start;
28 location_square = location_start;
29 location_random = location_start;
30 location_periodic = location_start;
31
32
33 %Generate and execute sequence of random steps
34 %Steps can be up, down, left, or right and of length 'steplength'
35 %%%%%%
36 sequence = rand(1,steps);
37
38
39 for i = 1:steps
40     history_fib(i,:) = location_fib;
41     history_RS(i,:) = location_RS;
42     history_TM(i,:) = location_TM;
43     history_square(i,:) = location_square;
44     history_random(i,:) = location_random;
45     history_periodic(i,:) = location_periodic;
46     i;
47
48 %      disp('here')
49 if sequence(i) < 0.146447
50     % Left
51     location_fib = takeStep(lattice_fib, location_fib, left);
52     location_RS = takeStep(lattice_RS, location_RS, left);
53     location_TM = takeStep(lattice_TM, location_TM, left);
54     location_square = takeStep(lattice_square, location_square, left);
55     location_random = takeStep(lattice_random, location_random, left);
56     location_periodic = takeStep(lattice_periodic, location_periodic, left);
57 elseif sequence(i) > 0.146447 && sequence(i) < 0.25
58     % UpLeft
59     location_fib = takeStep(lattice_fib, location_fib, upleft);
60     location_RS = takeStep(lattice_RS, location_RS, upleft);
61     location_TM = takeStep(lattice_TM, location_TM, upleft);
62     location_square = takeStep(lattice_square, location_square, upleft);
63     location_random = takeStep(lattice_random, location_random, upleft);

```

```

64 location_periodic = takeStep(lattice_periodic , location_periodic , upleft );
65
66 elseif sequence(i) >0.25 && sequence(i) < 0.396447
67 % Up
68 location_fib = takeStep( lattice_fib , location_fib , up);
69 location_RS = takeStep(lattice_RS,location_RS,up);
70 location_TM = takeStep(lattice_TM,location_TM,up);
71 location_square = takeStep(lattice_square , location_square , up);
72 location_random = takeStep(lattice_random,location_random,up);
73 location_periodic = takeStep(lattice_periodic , location_periodic , up);
74 elseif sequence(i) >0.396447 && sequence(i) < 0.5
75 % Upright
76 location_fib = takeStep( lattice_fib , location_fib , upright);
77 location_RS = takeStep(lattice_RS,location_RS,upright);
78 location_TM = takeStep(lattice_TM,location_TM,upright);
79 location_square = takeStep(lattice_square , location_square , upright);
80 location_random = takeStep(lattice_random,location_random,upright);
81 location_periodic = takeStep(lattice_periodic , location_periodic , upright);
82 elseif sequence(i) >0.5 && sequence(i) < 0.646447
83 % Right
84 location_fib = takeStep( lattice_fib , location_fib , right );
85 location_RS = takeStep(lattice_RS,location_RS,right );
86 location_TM = takeStep(lattice_TM,location_TM,right );
87 location_square = takeStep(lattice_square , location_square , right );
88 location_random = takeStep(lattice_random,location_random,right );
89 location_periodic = takeStep(lattice_periodic , location_periodic , right );
90 elseif sequence(i) >0.646447 && sequence(i) < 0.75
91 % downright
92 location_fib = takeStep( lattice_fib , location_fib , downright);
93 location_RS = takeStep(lattice_RS,location_RS,downright);
94 location_TM = takeStep(lattice_TM,location_TM,downright);
95 location_square = takeStep(lattice_square , location_square , downright);
96 location_random = takeStep(lattice_random,location_random,downright);
97 location_periodic = takeStep(lattice_periodic , location_periodic , downright)
98 ;
99 elseif sequence(i) >0.75 && sequence(i) < 0.896447
100 % down
101 location_fib = takeStep( lattice_fib , location_fib , down);
102 location_RS = takeStep(lattice_RS,location_RS,down);
103 location_TM = takeStep(lattice_TM,location_TM,down);
104 location_square = takeStep(lattice_square , location_square , down);
105 location_random = takeStep(lattice_random,location_random,down);

```

```

105     location_periodic = takeStep(lattice_periodic , location_periodic ,down);
106
107 else
108     % down left
109     location_fib = takeStep( lattice_fib , location_fib ,downleft);
110     location_RS = takeStep(lattice_RS,location_RS,downleft);
111     location_TM = takeStep(lattice_TM,location_TM,downleft);
112     location_square = takeStep(lattice_square ,location_square ,downleft);
113     location_random = takeStep(lattice_random,location_random,downleft);
114     location_periodic = takeStep( lattice_periodic , location_periodic ,downleft);
115
116 end
117
118
119
120 % Calculate Mean Square Average Deviation from start
121 dev_fib = ( location_fib (1)–location_start (1))^2 + (location_fib (2)–location_start
122 (2))^2;
123 dev_RS = (location_RS(1)–location_start(1))^2 + (location_RS(2)–location_start(2))
124 ^2;
125 dev_TM = (location_TM(1)–location_start(1))^2 + (location_TM(2)–location_start
126 (2))^2;
127 dev_square = (location_square(1)–location_start (1))^2 + (location_square(2)–
128 location_start (2))^2;
129 dev_random = (location_random(1)–location_start(1))^2 + (location_random(2)–
130 location_start(2))^2;
131
132 %%%%%%
133 % figure
134 % contourf( lattice_fib ,1),colormap(flipud(gray(2)))
135 % hold on
136 % scatter( history_fib (:,1) , history_fib (:,2) , 'MarkerFaceColor' , 'blue');
137 % title ('Fibonacci')
138 % xlim([0 size])
139 % ylim([0 size])
140 %

```

```

141 %%%%%%
142 % figure
143 % contourf(lattice_RS,1), colormap(flipud(gray(2)))
144 % hold on
145 % scatter(history_RS(:,1),history_RS(:,2), 'MarkerFaceColor', 'blue');
146 % title ('RS')
147 % xlim([0 size])
148 % ylim([0 size])
149 %
150 %%%%%%
151 % figure
152 % contourf(lattice_TM,1), colormap(flipud(gray(2)))
153 % hold on
154 % scatter(history_TM(:,1),history_TM(:,2), 'MarkerFaceColor', 'blue');
155 % title ('TM')
156 % xlim([0 size])
157 % ylim([0 size])
158 %
159 %
160 %%%%%%
161 % figure
162 % contourf(lattice_square,1), colormap(flipud(gray(2)))
163 % hold on
164 % scatter(history_square(:,1),history_square(:,2), 'MarkerFaceColor', 'blue');
165 % title ('square')
166 % xlim([0 size])
167 % ylim([0 size])
168 %
169 %
170 %%%%%%
171 % figure
172 % contourf(lattice_periodic,1), colormap(flipud(gray(2)))
173 % hold on
174 % scatter(history_periodic(:,1),history_periodic(:,2), 'MarkerFaceColor', 'blue');
175 % title ('periodic')
176 % xlim([0 size])
177 % ylim([0 size])
178 %
179 %%%%%%
180 % figure
181 % contourf(lattice_random,1), colormap(flipud(gray(2)))
182 % hold on

```

```
183 % scatter(history_random(:,1),history_random(:,2), 'MarkerFaceColor', 'blue');  
184 % title ('random')  
185 % xlim([0 size])  
186 % ylim([0 size])  
187 %%%%%%  
188  
189 end
```

Listing A.10: RW2D_8.m - Used to generate the two-dimensional grid-based random walk on all arrays of interest

References

- Asatryan, A. A., Nicorovici, N. A., Robinson, P. A., de Sterke, C. M., and McPhedran, R. C. (1996). Electromagnetic localization in one-dimensional stacks with random loss and gain. *Physical Review B*, 54(6):3916–3925.
- Barthelemy, P. (2009). *Anomalous Transport of Light*. PhD thesis, LENS (European Laboratory of Nonlinear Spectroscopy).
- Barthelemy, P., Bertolotti, J., and Wiersma, D. S. (2008). A levy flight for light. *Nature*, 453(7194):495–498.
- Ben-Avraham, D. and Havlin, S. (2000). *Diffusion and reactions in Fractals and Disordered Systems*. Cambridge University Press.
- Bertolotti, J. (2007). *Light Transport Beyond Diffusion*. PhD thesis, LENS (European Laboratory of Nonlinear Spectroscopy).
- Boriskina, S. V., Gopinath, A., and Negro, L. D. (2008). Optical gap formation and localization properties of optical modes in deterministic aperiodic photonic structures. *Optics Express*, 16(23):18813–18826.
- Bunde, A. and Havlin, S. (1991). *Fractals and Disordered Systems*. Springer-Verlag.
- Cheng, S.-F. and Jin, G.-J. (2002). Trace map and eigenstates of a thue-morse chain in a general model. *Physical Review B*, 65(13):134206.
- Dal Negro, L., Feng, N.-N., and Gopinath, A. (2008). Electromagnetic coupling and plasmon localization in deterministic aperiodic arrays. *Journal of Optics A: Pure and Applied Optics*, 10(6):064013.
- Dal Negro, L., Oton, C. J., Gaburro, Z., Pavesi, L., Johnson, P., Lagendijk, A., Righini, R., Colocci, M., and Wiersma, D. S. (2003). Light transport through the band-edge states of fibonacci quasicrystals. *Physical Review Letters*, 90(5):055501.
- Dal Negro, L., Stolfi, M., Yi, Y., Michel, J., Duan, X., Kimerling, L. C., LeBlanc, J., and Haavisto, J. (2004). Photon band gap properties and omnidirectional reflectance in Si/SiO₂ thuemorse quasicrystals. *Applied Physics Letters*, 84(25):5186.

- Dallapiccola, R., Gopinath, A., Stellacci, F., and Negro, L. D. (2008). Quasi-periodic distribution of plasmon modes in two-dimensional fibonacci arrays of metal nanoparticles. *Optics Express*, 16(8):5544–5555.
- Daozhong, Z., Wei, H., Youlong, Z., Zhaolin, L., Bingying, C., and Guozhen, Y. (1994). Experimental verification of light localization for disordered multilayers in the visible-infrared spectrum. *Physical Review B*, 50(14):9810–9814.
- Dulea, M., Johansson, M., and Riklund, R. (1992). Localization of electrons and electromagnetic waves in a deterministic aperiodic system. *Physical Review B*, 45(1):105–114.
- Fouque, J.-P., Garnier, J., Papanicolaou, G., and Solna, K. (2007). *Wave Propagation and Time Reversal in Randomly Layered Media (Stochastic Modelling and Applied Probability)*. Springer.
- Gaponenko, S. V. (2010). *Introduction to Nanophotonics*. Cambridge University Press, New York, N.Y.
- Garcia, N., Genack, A. Z., and Lisyansky, A. A. (1992). Measurement of the transport mean free path of diffusing photons. *Physical Review B*, 46(22):14475–14479.
- Gellermann, W., Kohmoto, M., Sutherland, B., and Taylor, P. C. (1994). Localization of light waves in fibonacci dielectric multilayers. *Physical Review Letters*, 72(5):633–636.
- Gopinath, A., Boriskina, S. V., Feng, N.-N., Reinhard, B. M., and Dal Negro, L. (2008). Photonic-plasmonic scattering resonances in deterministic aperiodic structures. *Nano Letters*, 8(8):2423–2431.
- Gouyet, J. (1996). *Physics and Fractal Structures*. Springer-Verlag.
- Inose, Y., Sakai, M., Ema, K., Kikuchi, A., Kishino, K., and Ohtsuki, T. (2010). Light localization characteristics in a random configuration of dielectric cylindrical columns. *Physical Review B*, 82(20):205328.
- Janot, C. (1997). *Quasicrystals: a primer*. Clarendon Press, Oxford.
- Jespersen, S., Metzler, R., and Fogedby, H. C. (1999). Lévy flights in external force fields: Langevin and fractional fokker-planck equations and their solutions. *Physical Review E*, 59(3):2736–2745.
- Lagendijk, A. and Dainty, J. (1999). *Current Trends in Optics*. Academic Press, London.

- Maciá, E. (2006). The role of aperiodic order in science and technology. *Reports on Progress in Physics*, 69(2):397.
- Metzler, R. and Klafter, J. (2000). The random walk's guide to anomalous diffusion: a fractional dynamics approach. *Physics Reports*, 339(1):1 – 77.
- Schroeder, M. R. (1985). *Number theory in science and communication*. Springer-Verlag.
- Schroeder, M. R. (1991). *Fractals, Chaos, Power Laws*. Freeman, New York.
- Sheng, P. (1995). *Introduction to Wave Scattering, Localization, and Mesoscopic Phenomena*. Academic Press, San Diego, C.A.
- Stanley, H. E. and Havlin, S. (1987). Generalisation of the sinai anomalous diffusion law. *Journal of Physics A: Mathematical and General*, 20(9):L615–L618.
- Taflove, A. (1980). Application of the finite-difference time-domain method to sinusoidal steady-state electromagnetic-penetration problems. *IEEE Transactions On Electromagnetic Compatibility*, EMC-22(3):191–202.
- Thouless, D. J. (1974). Electrons in disordered systems and the theory of localization. *Physics Reports*, 13(3):93 – 142.
- Trevino, J., Cao, H., and Dal Negro, L. (2011). Circularly symmetric light scattering from nanoplasmonic spirals. *Nano Letters*.

CURRICULUM VITAE

Travis Rich

EDUCATION

Master of Science, Electrical Engineering

Boston University, 2011

Bachelor of Science, Electrical Engineering

Boston University, 2010

EXPERIENCE

Boston University Nanomaterials and Nanostructure Optics Lab - *Research Assistant*

Advisor: Luca Dal Negro | Boston, MA, 2010-2011

Focus: *Photonic subdiffusion, aperiodic nanophotonics, electromagnetic simulations*

Smart Lighting Engineering Research Center - *Research Assistant*

Advisor: Thomas Little | Boston, MA, 2009-2011

Focus: *Dual-use optical communications, networking via solid-state lighting*

Smart Travel - *Hardware Engineer*

Advisor: Thomas Little | Boston, MA, 2009-2011

Focus: *Vehicular communications and networking, optical communications*

MIT RLE - Optics and Quantum Electronics Group - *Research Assistant*

Advisor: Franz Kaertner | Cambridge, MA, 2009-2010

Focus: *Femtosecond laser frequency combs, four-level laser cavity loss measurements*

Innosynthesis, Inc. - *Principal Engineer*

Advisor: Bunmi Adekore | Boston, MA, 2010-2011

Focus: *Solid-state medical diagnostic hardware design, C++, optical diagnostics*

AWARDS

BU College of Engineering Dean's Fellowship - 2010

MobiSys Conference Best Poster Award - 2010

NSF Graduate Research Fellowship Honorable Mention - 2010

Earle and Mildred Bailey Memorial Award - 2010

Summer Term Alumni Research Scholars Program - 2009

ACTIVITIES

Tau Beta Pi Engineering Honor Society - *MA Eta President* | 2009-2010

Smart Lighting High School Outreach Program | 2009-2011